FFI-rapport 2015/01554

Improving ship detection by using polarimetric decompositions

Tonje Nanette Arnesen Hannevik, Knut Eldhuset
and Richard B. Olsen

FFI Forsvarets forskningsinstitutt

Improving ship detection by using polarimetric decompositions

Tonje Nanette Arnesen Hannevik, Knut Eldhuset and Richard B. Olsen

Norwegian Defence Research Establishment (FFI)

12 October 2015

FFI-rapport 2015/01554

1318

P: ISBN 978-82-464-2584-9
E: ISBN 978-82-464-2585-6

Emneord

Polarimetri

Skipsdeteksjon

Is

Dekomposisjon

Syntetisk aperture-radar (SAR)

Satellittbilder

Godkjent av

Richard B. Olsen	Project manager
Johnny Bardal	Director

English summary

Norway’s large ocean areas require efficient methods to monitor vessels. Radar satellites in orbit today offer dual- or quad-polarised data, which ease the task of detecting vessels in a SAR (Synthetic Aperture Radar) image.

The Norwegian Defence Research Establishment (FFI) has developed an automatic ship detection tool, Aegir, which uses all polarisation channels to detect vessels. The ship detector also combines the available polarisation channels to increase the ship to sea contrast to be able to detect more vessels.

Since 2011 it is possible to use fully polarimetric images with large area coverage (50 km swath width, while 25 km before). This is of potential interest for operative maritime surveillance.

26 RADARSAT-2 dual-polarisation and 24 quad-polarisation images have been analyzed both manually and automatically. Using Aegir, it is shown that cross-polarisation and $(HH\text{-}VV)\times HV$ are best for ship detection.

Using manual analysis, some decomposition methods have been tested: Pauli, Circular, Krogager and Yamaguchi methods. The polarisation decomposition methods can be used to increase the ship to sea contrast and they can also be used to help discriminate between ice and vessels. It is shown that the Yamaguchi decomposition method gives promising results for differentiating between vessels and ice.

The different methods used in the analysis, and the theory behind the methods, for both dual-polarised and quad-polarised images are described in the report.

Sammendrag

Norge har store havområder som krever effektive overvåkingsmetoder for å ha mulighet til å ha oversikt over skipstrafikken. Radarsatelitter i dag tilbyr dual- eller full-polarimetriske data, noe som forbedrer skipsdeteksjon i et Syntetisk Aperture Radar-bilde (SAR).

Forsvarets Forskningsinstitutt (FFI) har utviklet et skipsdeteksjonsverktøy, Ægir, som bruker alle polariseringskanaler for å detektere skip. Skipsdetektoren kombinerer de tilgjengelige polariseringskanalene for å øke skip-til-sjø-kontrasten for å ha mulighet for å detektere flere skip.

Siden 2011 er det blitt mulig å bruke fullpolarimetriske bilder med stor arealdekning (50 km båndbredde mot tidligere 25 km). Dette er potensielt av interesse for operativ havovervåking.

26 RADARSAT-2 dual-polarimetri- og 24 full-polarimetri-bilder har blitt analysert både manuelt og automatisk. Ved å bruke Ægir, er det vist at krysspolarisering og $(HH\text{-}VV)\times HV$ er best for skipsdeteksjon når full-polarimetri er tilgjengelig.

Ved å bruke manuell analyse, har flere dekomposisjonsmetoder blitt testet ut: Pauli, sirkulær, Krogager og Yamaguchi. Dekomposisjonsmetodene kan brukes til å øke skip-til-sjø-kontrasten og de kan også brukes til å se forskjell på skip og is i SAR-bilder. Yamaguchi dekomposisjon har vist lovende resultater for differensiering mellom skip og is.

De forskjellige metodene som er brukt i analysen, og teorien bak metodene for både dual- og full-polarimetri-bilder er beskrevet i rapporten.

Contents

1 Introduction

Requirements for effective monitoring of the Norwegian ocean areas in the High North are increasing. RADARSAT-2 delivers several SAR (Synthetic Aperture Radar) images to the Norwegian authorities every week. After the launch and commissioning of Sentinel-1A in 2014, the volume of available SAR imagery has increased. Earlier advice for ship detection has been to use large incidence angles and HH-polarisation to detect ships. Research has shown that cross-polarised data can be used for ship detection at high incidence angles as well as low incidence angles [1],[2]. Research has also indicated that it is easier to estimate more accurate ship lengths in cross-polarised data compared to co-polarised data [3].

This report will look at optimizing the use of the different polarisations available, both for automatic ship detection and for manual analysis of vessels. Some basic polarisation theory and how polarisation influences ship detection are described in section 1. The theory behind polarimetric decompositions is described in section 2. Some of these polarimetric decompositions have been used to do ship and ice detection in SAR images, and the results are shown in section 3. Section 4 gives the conclusions and suggestions for further work.

1.1 Polarisation

Radar makes use of electromagnetic transverse waves, and thus, they can be polarised. Linear polarisation refers to how the radar beam's orientation (the electric field's orientation) relative to the Earth's surface is. Horizontal polarisation (*H*) from a satellite is when the electrical field of the transmitted radar wave from the satellite is approximately normal to the plane of incidence, while the electric field is parallel to the plane of incidence in vertical polarisation (*V*).

Radar images from satellites can offer *HH*, *VV*, *HV* and/or *VH* images. The *HH*- and *VV*-channels are referred to as co-polarised channels, while the *HV*- and *VH*-channels are referred to as cross-polarised channels. *VV*-polarisation means that the radar both transmits and receives vertical polarised radiation, while HH-polarisation means that the radar both transmits and receives horizontal polarised radiation. Cross-polarisation may either be *HV*-polarised, where the transmitted radiation is horizontal and the received radiation is vertical, or *VH*-polarised, where the transmitted radiation is vertical and the received radiation is horizontal. Figure 1.1 shows how the electric field is oriented for *H*- and *V*-polarisation (top) and for cross-polarisation (bottom).

While early civil SAR satellites such as ERS-1 and Radarsat-1 only provided single polarisation data (*VV* and *HH* respectively), newer satellites such as Radarsat-2, TerraSAR-X, Cosmo-Skymed and Sentinel-1A have selectable polarisation modes. While Radarsat-2 has the capability to provide fully polarimetric data (*HH*, *VV*, *HV* and *VH*) operationally, TerraSAR-X is only operated experimentally in polarimetric mode, the other satellites are limited to two simultaneous polarisations (dual-pol modes).

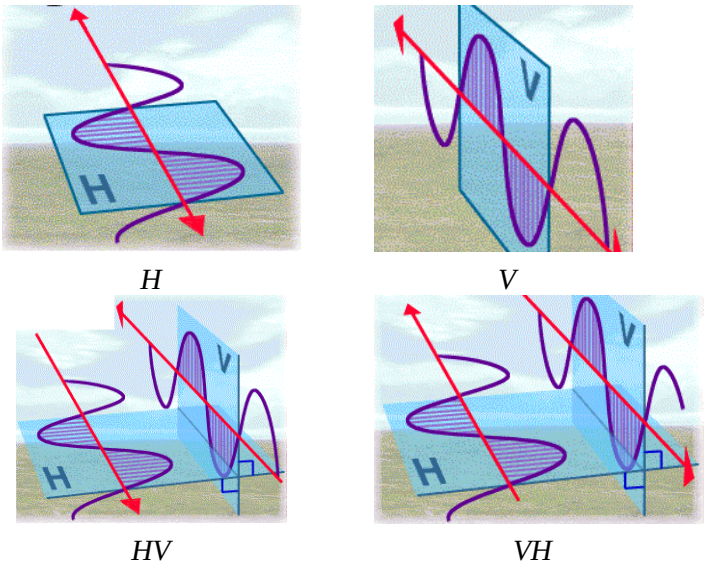

Figure 1.1 Top: Transmitted and received HH- and VV-polarisation. Bottom: Cross-polarisation, HV and VH. Source: ESA

With suitable phasing of vertically and horizontally linear-polarised signals, it is possible to synthesize circular-polarised data on transmission. Reception of the scattered signal in *H*- and *V*- linearly polarised channels results in a sub-set of polarimetric data, referred to as compact polarimetry [4]. This is currently implemented on the Indian radar satellite RISAT and the Japanese ALOS-2, and will be available on future satellites such as the satellites in the Canadian Radarsat Constellation Mission.

1.2 Polarisation and ship detection

Polarisation is an important factor when working with ship detection. Different materials and surfaces have different scattering properties in the several polarisations and polarisation combinations available today. The structure of the ship, the ship's orientation compared to the radar, motion and sea state all play an important role in how a vessel reflects the radar signals back to the satellite.

Depending on how complex the ship's superstructure is, the number of reflections from the surface of the ship can be both even (double) and odd (single and triple) and in addition reflections can occur from corners, edges and cables on the ship.

Multi-polarised SAR data give substantially more information than the more traditional single-polarised SAR data. Using more polarisation channels makes it easier to detect vessels and to discriminate between vessels and ice. Co-polarised data are suitable for detecting vessels at large incidence angles, when ship to sea contrast is maximized due to lower backscatter from the ocean background. Cross-polarised data have much weaker ocean backscatter, and is less dependent on imaging geometry and wind conditions. Thus, ship detection can be done at smaller incidence angles than in co-polarisation.

1.3 Dual-polarisation

Dual-polarised data are in the combinations *HH/VV*, *HH/HV* or *VV/VH*. For dual-polarised radar data, two images are obtained over the same area. The data can either be:

- *HH/VV* where one image is obtained by transmitting and receiving horizontal radiation and the other image is obtained by transmitting and receiving vertical radiation.
- *HH/HV* where one image is obtained by transmitting and receiving horizontal radiation and the other image is obtained by transmitting horizontal and receiving vertical radiation.
- *VV/VH* where one image is obtained by transmitting and receiving vertical radiation and the other image is obtained by transmitting vertical radiation and receiving horizontal radiation.

The information in these data sets is not as complete as in fully polarimetric data sets, so it is not possible to do a full decomposition into the different scattering types over the imaged area. On the upside, dual-polarised data are better for operational use, since the data are available in wider swaths, i.e. the temporal coverage is better.

When carrying out ship detection, it is possible to:

1. detect ships in each channel separately
2. combine the two channels by multiplying the two channels to get a combined polarisation image, and subsequently perform ship detection.

Figure 1.2 shows ScanSAR polarisation combinations for *VV*-polarisation, *VH*-polarisation and the combined case (multiplying the two channels and dividing by a constant to scale the image).

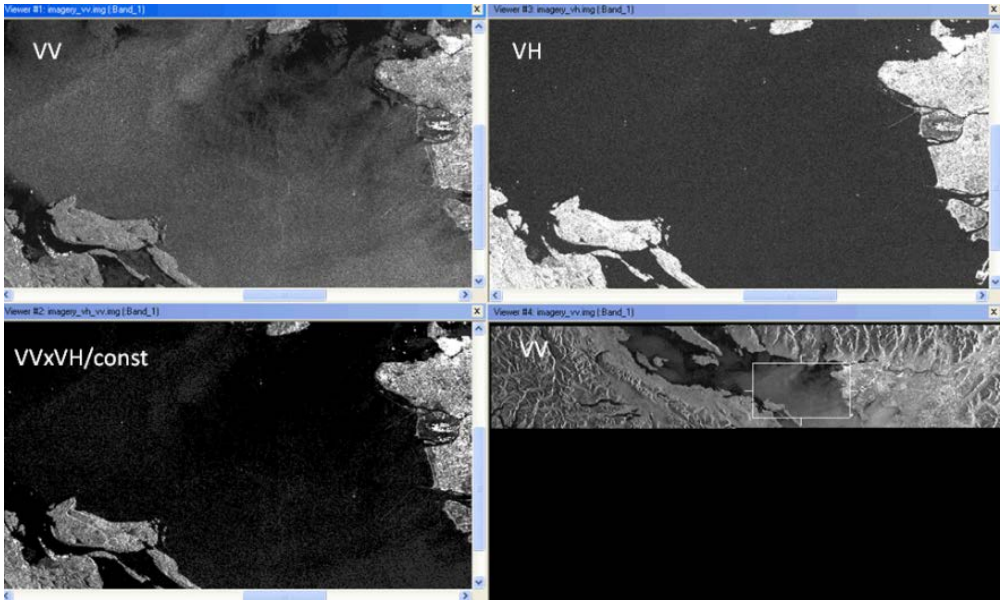

Figure 1.2 ScanSAR polarisation combinations in VV, VH and by combining the VV- and VH-channel.

The contrast between land and sea and how clearly the vessels are visible differ between the different sub images. The contrast and the vessels are most clear in the combined case. VV-polarisation gives most information about the sea.

1.4 Quad-polarisation

Quad-polarisation mode gives four images over the same area. The SAR images are delivered in *HH*, *VV*, *HV* and *VH*, and it is possible to use all four polarisation channels to image a ship and its surroundings. Each polarisation channel has different characteristics, and can be used to get better information about the physical properties of hard targets and the ocean background. Quad-polarisation also gives the possibility to combine the information from the different polarisation channels in a polarimetric analysis. This analysis gives information about structure and shape of different scattering surfaces. Thus, it is possible to get more complete information when fully polarimetric data is available. The scattering matrix, S, from a vessel can be decomposed in many different ways when fully polarimetric data is available.

Research in polarimetry has resulted in a number of ways to combine the different polarisation channels, and various interpretations of the scattering mechanisms associated with the individual and combined polarisation options.

2 Polarimetric decompositions

When quad-polarised data are available, the scattering matrix for a target can be constructed [5]:

$$S = \begin{bmatrix} S_{HH} & S_{HV} \\ S_{VH} & S_{VV} \end{bmatrix} = m \begin{bmatrix} \cos 2\theta & \sin 2\theta \\ \sin 2\theta & -\cos 2\theta \end{bmatrix} \tag{2.1}$$

where m is the true strength of a scatterer, and θ is the scatterer's orientation angle relative to the z-axis. Therefore polarimetric radar will provide useful information about the target. Data from a polarimetric radar system can also be used to distinguish between different types of scatterers, for example the contributions from even- and odd-bounce scattering. These can be estimated using different polarimetric decompositions.

Polarimetric decompositions are usually divided into two groups, model-based decompositions (see chapter 2.1) and coherent decompositions (see chapter 2.2).

2.1 Model-based decompositions

There are many model-based decompositions, for example Freeman-Durden three-component decomposition, Freeman two-component decomposition and the Yamaguchi four-component decomposition. The Freeman-Durden three-component decomposition is useful over forested areas, because it is possible to discriminate between flooded and non-flooded areas in the forest and between forested and non-forested areas [6]. The mechanisms are canopy scatter (volume), Bragg scatter (direct/surface) and even- or double-bounce scatter. The Freeman two-component

decomposition is more sensitive to forest canopy and also to the ratio of the canopy to ground reflections. Here a canopy scatter and a ground scatter (double-bounce scatter or a Bragg scatter) are the selected mechanisms. The Yamaguchi four-component decomposition with rotation makes it possible to discriminate between oriented urban blocks (double bounce scattering) and vegetation (volume scattering) [6], because the method minimizes the cross-polarized *HV* component and oriented urban blocks are emphasised. Without the rotation, the volume scattering from the houses and streets are emphasised.

This chapter only describes the Yamaguchi four-component decomposition due to its promising possibilities for ship and ice detection.

2.1.1 Yamaguchi four-component decomposition

To decompose polarimetric SAR (Synthetic Aperture Radar) images Yamaguchi has proposed a four-component scattering model in [7] and [8]. This scattering model can carry out the four-component decomposition directly or make use of a rotation of the coherency matrix before doing the four-component decomposition. To retrieve the rotation angle, the cross-polarised component is minimized. The rotation angle is then used to rotate the coherency matrix. Then the four-component scattering power decomposition method is applied to the four fully polarimetric SAR images. Only the coherency matrix elements are used in this decomposition algorithm. The method is simple and effective, and it makes it possible to discriminate between different scattering objects that were previously difficult to discriminate, for example oriented urban blocks (double bounce scattering) versus vegetation (volume scattering).

Originally the polarimetric SAR data of the imaging pixel were divided into volume scattering, surface scattering, double bounce scattering and helix scattering components when using the three- or four-component decomposition method. Using these individual components it is possible to make full colour images with red, green and blue (RGB). Red is used for double bounce, green is used for volume scattering and blue is used for surface scattering. The brightness of each colour corresponds to the magnitude of the individual scattering components.

Without using the Yamaguchi decomposition method, man-made structures, such as building blocks, can exhibit volume scattering if the main scattering centre is at an oblique direction with respect to the radar illumination [7]. Thus, urban areas can be misinterpreted as vegetation. To be able to classify these oblique oriented building blocks as man-made structures, the Yamaguchi four-component decomposition method can be used. The idea was first proposed by Huynen [9].

In [7] they say that this idea shows that “the desying operation (elimination of the tilt angle) is one of the major processes that fully polarimetric synthetic aperture radar (SAR) image processing allows one to do”. The terminology “deorientation” is used in [10], and the idea is further developed. The concept is adopted and applied to the four-component scattering power decomposition in [11]. The rotation of the coherency matrix, the rotation angle and the decomposition scheme using the rotated coherency matrix are described in [7].

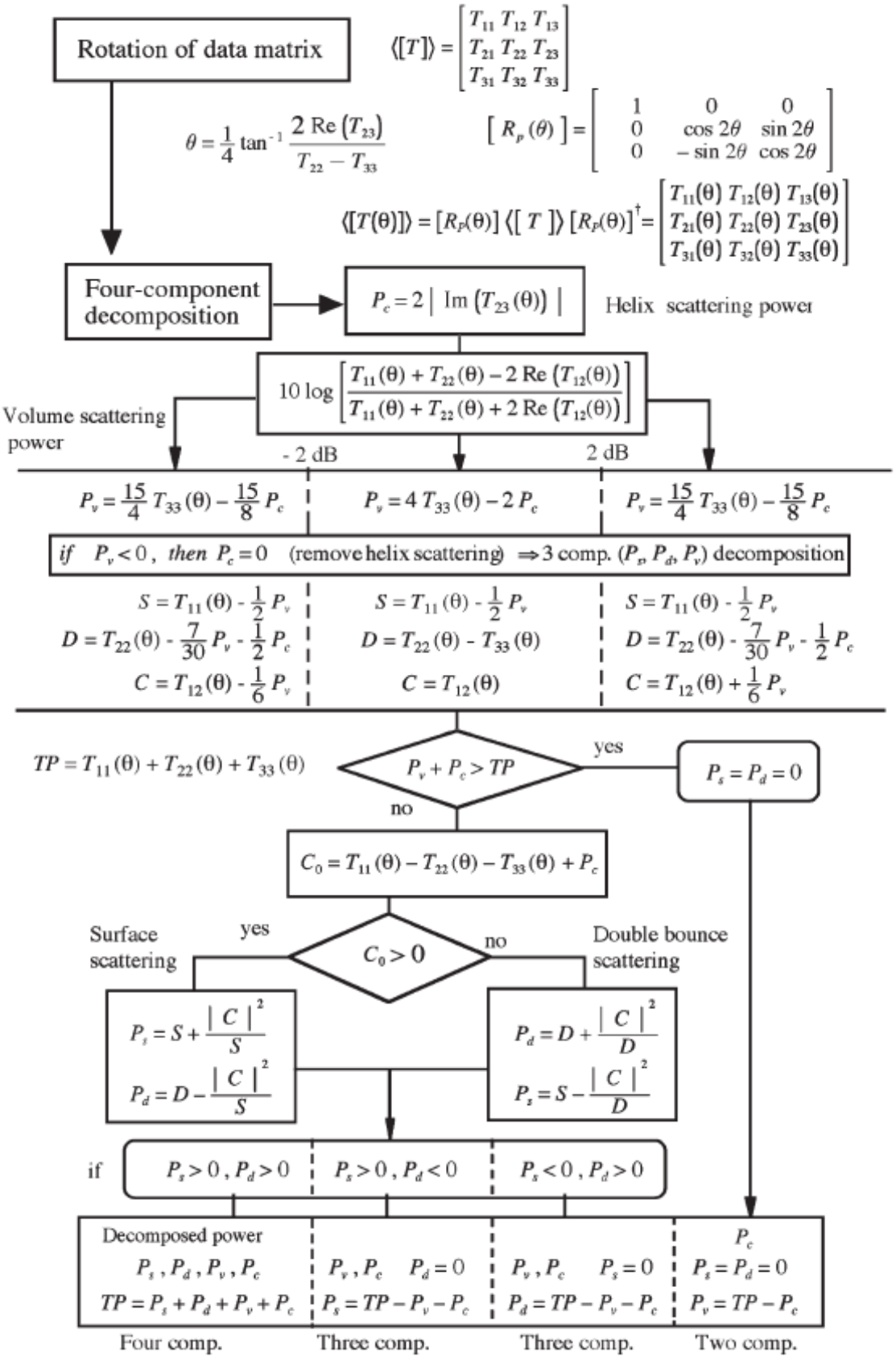

Figure 2.1 Yamaguchi "four-component scattering power decomposition algorithm" with and without rotation of the coherency matrix. Source: [7]

It might be interesting to see if this decomposition method and algorithm can be used for ship detection, ice detection, as well as ship and ice discrimination at sea.

Figure 2.1 shows the algorithm used in the Yamaguchi four-component decomposition method. It is possible to represent the results of the decomposition method with rotation and without rotation of the coherency matrix.

Without rotation of the data matrix:

First the procedure without rotation is described. This presentation is built upon Figure 2.1. The expected value of the coherency matrix is the starting point:

$$\langle [T] \rangle = \begin{bmatrix} T_{11} & T_{12} & T_{13} \\ T_{21} & T_{22} & T_{23} \\ T_{31} & T_{32} & T_{33} \end{bmatrix} \tag{2.2}$$

$$\langle [T] \rangle = \begin{bmatrix} \frac{1}{2}\langle |S_{HH}+S_{VV}|^2 \rangle & \frac{1}{2}\langle (S_{HH}+S_{VV})(S_{HH}-S_{VV})^* \rangle & \langle (S_{HH}+S_{VV})(S_{HV})^* \rangle \\ \frac{1}{2}\langle (S_{HH}-S_{VV})(S_{HH}+S_{VV})^* \rangle & \frac{1}{2}\langle |(S_{HH}-S_{VV})|^2 \rangle & \langle (S_{HH}-S_{VV})(S_{HV})^* \rangle \\ \langle (S_{HV})(S_{HH}+S_{VV})^* \rangle & \langle (S_{HV})(S_{HH}-S_{VV})^* \rangle & 2\langle |S_{HV}|^2 \rangle \end{bmatrix} \tag{2.3}$$

Equation (2.3) is found on page 68 in [6]. Here $\langle\ \rangle$ means the expected value and * means complex conjugated. The expected value of for example S_{HH} is calculated like this:

$$\langle S_{HH}(m,n) \rangle = \sum_{j=-1}^{1}\sum_{i=-1}^{1} (S_{HH}(m+i, n+j)/9) \tag{2.4}$$

Equation (2.4) is valid for all *m*'s and *n*'s, except the *m*'s and *n*'s at the edges (first and last row and first and last column). A square of 3 pixels × 3 pixels is used. To find for example S_{HH} (2,2), the following is calculated:

$$\begin{bmatrix} S_{HH}(1,1) & S_{HH}(1,2) & S_{HH}(1,3) \\ S_{HH}(2,1) & S_{HH}(2,2) & S_{HH}(2,3) \\ S_{HH}(3,1) & S_{HH}(3,2) & S_{HH}(3,3) \end{bmatrix} \tag{2.5}$$

The expected value of $S_{HH}(2,2)$ is calculated by equation (2.5), and then the new expected value of that pixel is found. This is done for each pixel in the matrix. The edges of the matrix are not valid, so these are left out and set to zero.

The helix scattering power component is given by:

$$P_c = 2|\mathrm{Im}\, T_{23}| \tag{2.6}$$

To find the volume scattering component one must find the value of the test variable:

$$10\log\left[\frac{T_{11}+T_{22}-2\,\mathrm{Re}\,T_{12}}{T_{11}+T_{22}+2\,\mathrm{Re}\,T_{12}}\right] \tag{2.7}$$

If this test value is smaller than -2 dB or larger than 2 dB, then P_V is found by:

$$P_v = \frac{15}{4}T_{33} - \frac{15}{8}P_c \tag{2.8}$$

If the test value is between -2 dB and 2 dB, then P_v is found by:

$$P_v = 4T_{33} - 2P_c \tag{2.9}$$

If $P_v < 0$, then $P_c = 0$, which means the helix component can be removed. Then there are three components left: surface scattering power component (P_s), double bounce scattering power component (P_d) and volume scattering power component (P_v). The variables *S*, *D* and *C* that will be used to find P_s, P_d and P_v must also be found. If the test value above is smaller than -2 dB, these variables are found by:

$$S = T_{11} - \frac{1}{2}P_v \qquad D = T_{22} - \frac{7}{30}P_v - \frac{1}{2}P_c \qquad C = T_{12} - \frac{1}{6}P_v \tag{2.10}$$

If the test value is between -2 dB and 2 dB, these variables are found by:

$$S = T_{11} - \frac{1}{2}P_v \qquad D = T_{22} - T_{33} \qquad C = T_{12} \tag{2.11}$$

If the test value is larger than 2 dB, these variables are found by:

$$S = T_{11} - \frac{1}{2}P_v \qquad D = T_{22} - \frac{7}{30}P_v - \frac{1}{2}P_c \qquad C = T_{12} + \frac{1}{6}P_v \tag{2.12}$$

Then one must calculate the total power, *TP*:

$$TP = T_{11} + T_{22} + T_{33} \tag{2.13}$$

If $P_v + P_c > TP$, then $P_s = P_d = 0$, and one ends up with a <u>two-component scattering</u> method where:

P_c is given by equation (2.6) and:

$$P_s = P_d = 0$$
$$P_v = TP - P_c \tag{2.14}$$

If $P_v + P_c < TP$, then the branch condition, C_0 is given by:

$$C_0 = T_{11} - T_{22} - T_{33} + P_c \tag{2.15}$$

The branch condition is used to decide if the surface scattering or double bounce scattering is dominant.

If $C_0 > 0$, then surface scattering is dominant:

$$P_s = S + \frac{|C|^2}{S} \tag{2.16}$$
$$P_d = D - \frac{|C|^2}{S} \tag{2.17}$$

If $C_0 < 0$, then double bounce scattering is dominant:

$$P_d = D + \frac{|C|^2}{D} \tag{2.18}$$
$$P_s = S - \frac{|C|^2}{D} \tag{2.19}$$

If $P_s > 0$ and $P_d > 0$, the four-component scattering components are given by:

$$TP = P_s + P_d + P_v + P_c \tag{2.20}$$

The individual components are given equations (2.6) (P_c), (2.8) or (2.9) (P_v), (2.16) or (2.19) (P_s) and (2.17) or (2.18) (P_d).

If $P_s > 0$ and $P_d < 0$, the three-component scattering components are given by:

$$P_d = 0$$
$$P_s = TP - P_v - P_c \tag{2.21}$$

P_c is given by equation (2.6) and P_v is given by equation (2.8) or (2.9).

Another three-component scattering is given by:

$P_s = 0$

$P_d = TP - P_v - P_c$ (2.22)

With rotation of the data matrix:

Here the procedure with rotation is described. The presentation is built upon Figure 2.1. The expected value of the coherency matrix is the starting point, see equation (2.2). The rotated data matrix is given by:

$$\langle [T(\theta)] \rangle = [R_p(\theta)] \langle [T] \rangle [R_p(\theta)]^{\dagger} = \begin{bmatrix} T_{11}(\theta) & T_{12}(\theta) & T_{13}(\theta) \\ T_{21}(\theta) & T_{22}(\theta) & T_{23}(\theta) \\ T_{31}(\theta) & T_{32}(\theta) & T_{33}(\theta) \end{bmatrix} \quad (2.23)$$

Where θ and $[Rp(\theta)]$ are given by:

$$\theta = \frac{1}{4}\tan^{-1}\frac{2\,\mathrm{Re}(T_{23})}{T_{22} - T_{33}} \quad (2.24)$$

$$[R_p(\theta)] = \begin{bmatrix} 1 & 0 & 0 \\ 0 & \cos 2\theta & \sin 2\theta \\ 0 & -\sin 2\theta & \cos 2\theta \end{bmatrix} \quad (2.25)$$

$<[T(\theta)]>$ is given by equation (2.3) and (2.23) - (2.25). Then the elements of the data matrix are given by:

$$T_{11}(\theta) = T_{11} = \frac{1}{2}\langle (S_{HH} + S_{VV}) \rangle \quad (2.26)$$

$$T_{12}(\theta) = T_{12}\cos 2\theta + T_{13}\sin 2\theta = \frac{1}{2}\langle (S_{HH} + S_{VV})(S_{HH} - S_{VV})^* \rangle \cos 2\theta + \langle (S_{HH} + S_{VV})(S_{HV})^* \rangle \sin 2\theta \quad (2.27)$$

$$T_{13}(\theta) = -T_{12}\sin 2\theta + T_{13}\cos 2\theta = -\frac{1}{2}\langle (S_{HH} + S_{VV})(S_{HH} - S_{VV})^* \rangle \sin 2\theta + \langle (S_{HH} + S_{VV})(S_{HV})^* \rangle \cos 2\theta \quad (2.28)$$

$$T_{21}(\theta) = T_{12}^*(\theta) \quad (2.29)$$

$$T_{22}(\theta) = T_{22}\cos^2 2\theta + T_{33}\sin^2 2\theta + \mathrm{Re}(T_{23})\sin 4\theta = \frac{1}{2}\langle |(S_{VV} - S_{HH})|^2 \rangle \cos^2 2\theta + 2\langle (S_{HV})^2 \rangle \sin^2 2\theta + \mathrm{Re}(\langle (S_{HH} - S_{VV})(S_{HV})^* \rangle)\sin 4\theta \quad (2.30)$$

$$T_{23}(\theta) = j\mathrm{Im}(T_{23}) = j\mathrm{Im}(\langle (S_{HH} - S_{VV})(S_{HV})^* \rangle) \quad (2.31)$$

$$T_{31}(\theta) = T_{13}^*(\theta) \quad (2.32)$$

$$T_{32}(\theta) = - jIm(T_{23}) = - jIm(\left\langle (S_{HH} - S_{VV})(S_{HV})^{*} \right\rangle) \tag{2.33}$$

$$T_{33}(\theta) = T_{33}\cos^2 2\theta + T_{22}\sin^2 2\theta - Re(T_{23})\sin 4\theta = 2\left\langle (S_{HV})^2 \right\rangle \cos^2 2\theta + \frac{1}{2}\left\langle |(S_{VV} - S_{HH})|^2 \right\rangle \sin^2 2\theta + Re(\left\langle (S_{HH} - S_{VV})(S_{HV})^{*} \right\rangle)\sin 4\theta \tag{2.34}$$

where * means complex conjugated.

The helix scattering power component is given by:

$$P_c = 2\left|\mathrm{Im}\, T_{23}(\theta)\right| \tag{2.35}$$

To find the volume scattering component one must find the value of:

$$10\log\left[\frac{T_{11}(\theta) + T_{22}(\theta) - 2\,\mathrm{Re}\, T_{12}(\theta)}{T_{11}(\theta) + T_{22}(\theta) + 2\,\mathrm{Re}\, T_{12}(\theta)}\right] \tag{2.36}$$

If this test value is smaller than -2 dB or larger than 2 dB, then P_V is found by:

$$P_v = \frac{15}{4}T_{33}(\theta) - \frac{15}{8}P_c \tag{2.37}$$

If the test value is between -2 dB and 2 dB, then P_v is found by:

$$P_v = 4T_{33}(\theta) - 2P_c \tag{2.38}$$

If $P_v < 0$, then $P_c = 0$, which means the helix component can be removed. Then there are three components left: surface scattering power component (P_s), double bounce scattering power component (P_d) and volume scattering power component (P_v). The variables *S*, *D* and *C* that will be used to find P_s, P_d and P_v must also be found. If the test value (equation (2.36)) is smaller than -2 dB, these variables are found by:

$$S = T_{11}(\theta) - \frac{1}{2}P_v \qquad D = T_{22}(\theta) - \frac{7}{30}P_v - \frac{1}{2}P_c \qquad C = T_{12}(\theta) - \frac{1}{6}P_v \tag{2.39}$$

If the test value is between -2 dB and 2 dB, these variables are found by:

$$S = T_{11}(\theta) - \frac{1}{2}P_v \qquad D = T_{22}(\theta) - T_{33}(\theta) \qquad C = T_{12}(\theta) \tag{2.40}$$

If the test value is larger than 2 dB, these variables are found by:

$$S = T_{11}(\theta) - \frac{1}{2}P_v \qquad D = T_{22}(\theta) - \frac{7}{30}P_v - \frac{1}{2}P_c \qquad C = T_{12}(\theta) + \frac{1}{6}P_v \tag{2.41}$$

Then one must calculate the total power, *TP*:

$$TP = T_{11}(\theta) + T_{22}(\theta) + T_{33}(\theta) \tag{2.42}$$

If $P_v + P_c > TP$, then $P_s = P_d = 0$, and one ends up with a two-component scattering method where:
P_c is given by equation (2.6), $P_s = P_d = 0$ and P_v is given by:

$$P_v = TP - P_c \tag{2.43}$$

If $P_v + P_c < TP$, then the branch condition, C_0 is given by:

$$C_0 = T_{11}(\theta) - T_{22}(\theta) - T_{33}(\theta) + P_c \tag{2.44}$$

The branch condition is used to decide if the surface scattering or double bounce scattering is dominant.

If $C_0 > 0$, then the surface scattering is dominant, and P_s and P_d are given by (2.16) and (2.17).
If $C_0 < 0$, then the double bounce scattering is dominant and P_d and P_s are given by (2.18) and (2.19).

If $P_s > 0$ and $P_d > 0$, the four-component scattering components are given by equation (2.20). The individual components are given by equations (2.6) (P_c), (2.8) or (2.9) (P_v), (2.16) or (2.19) (P_s) and (2.17) or (2.18) (P_d).

If $P_s > 0$ and $P_d < 0$, the three-component scattering components are found by the following procedure. P_c is given by equation (2.6) and P_v is given by equation (2.8) or (2.9), $P_d = 0$ and P_s is given by:

$$P_s = TP - P_v - P_c \tag{2.45}$$

Another three-component scattering is given by:

$$P_s = 0$$
$$P_d = TP - P_v - P_c \tag{2.46}$$

Some examples of the Yamaguchi decomposition method were made over Flevoland in the Netherlands in 2010 (see Figure 2.2 - Figure 2.5). Figure 2.2 shows the Yamaguchi decomposition for helix, volume, double bounce and surface (displayed with ERDAS). Figure 2.3 shows the Yamaguchi decomposition for helix, volume, double bounce and surface (displayed

with ERDAS) over San Fransisco, USA. Figure 2.4 shows a comparison between Yamaguchi and Pauli decomposition. Figure 2.5 shows Yamaguchi decomposition standard and rotated. The red colour means double scattering (buildings, man-made objects etc.). The green colour means volume scattering (higher vegetation etc.). The blue colour means direct scattering (open mountain areas, swamp areas, water etc.).

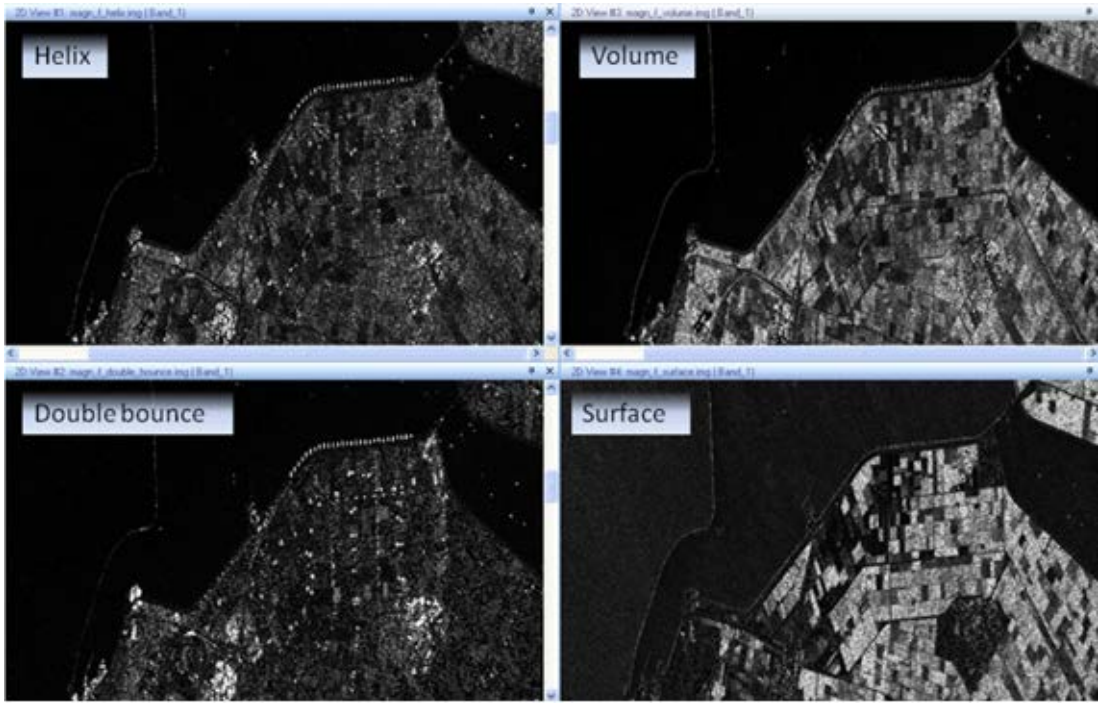

Figure 2.2 Yamaguchi decomposition over Flevoland in the Netherlands.

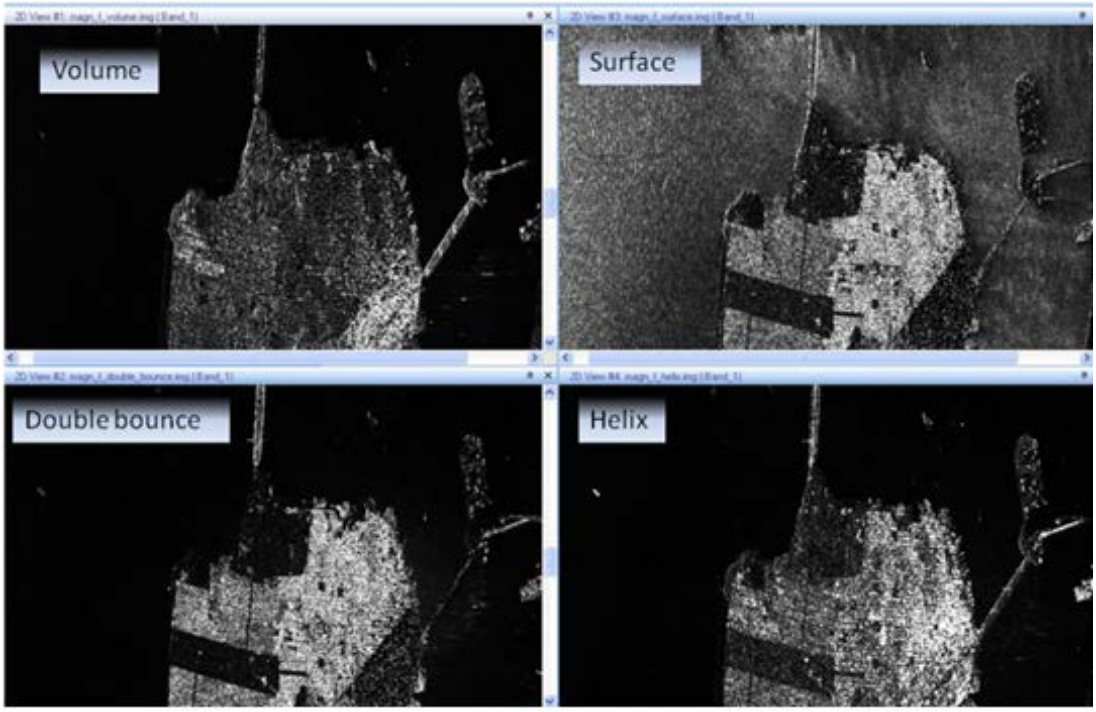

Figure 2.3 Yamaguchi decomposition over San Fransisco, USA.

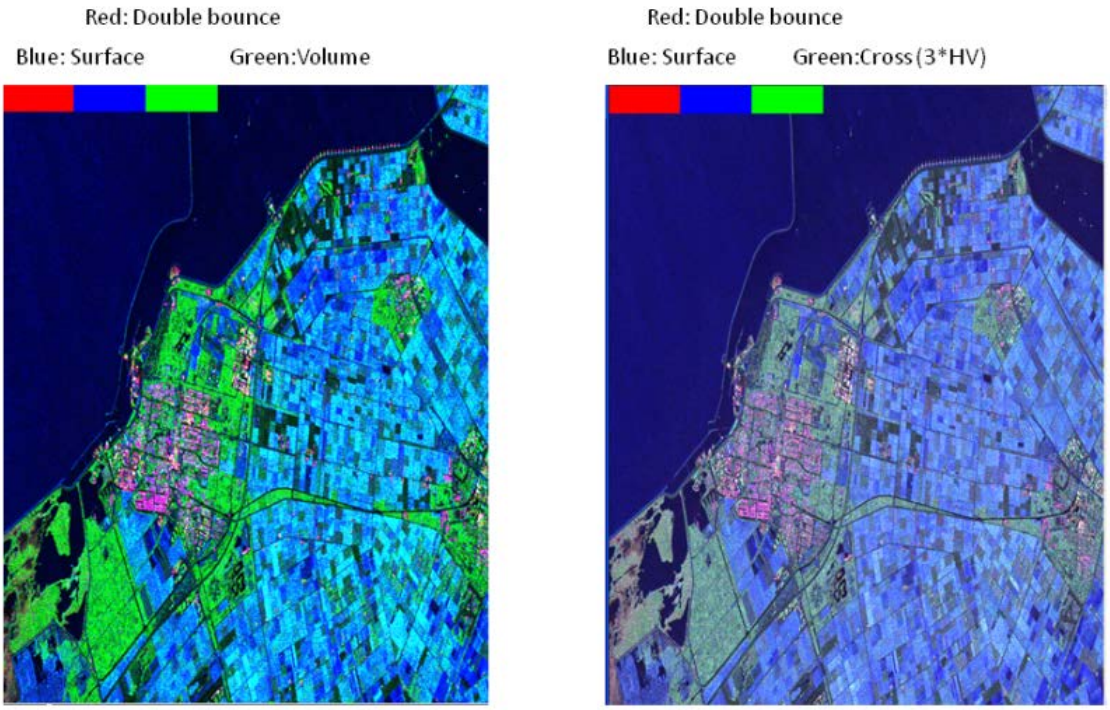

Figure 2.4 Yamaguchi (left) vs Pauli (right) decomposition. Red: Double bounce, Blue: Surface, Green: Volume (left) 3×HV (right) over Flevoland, Netherlands.

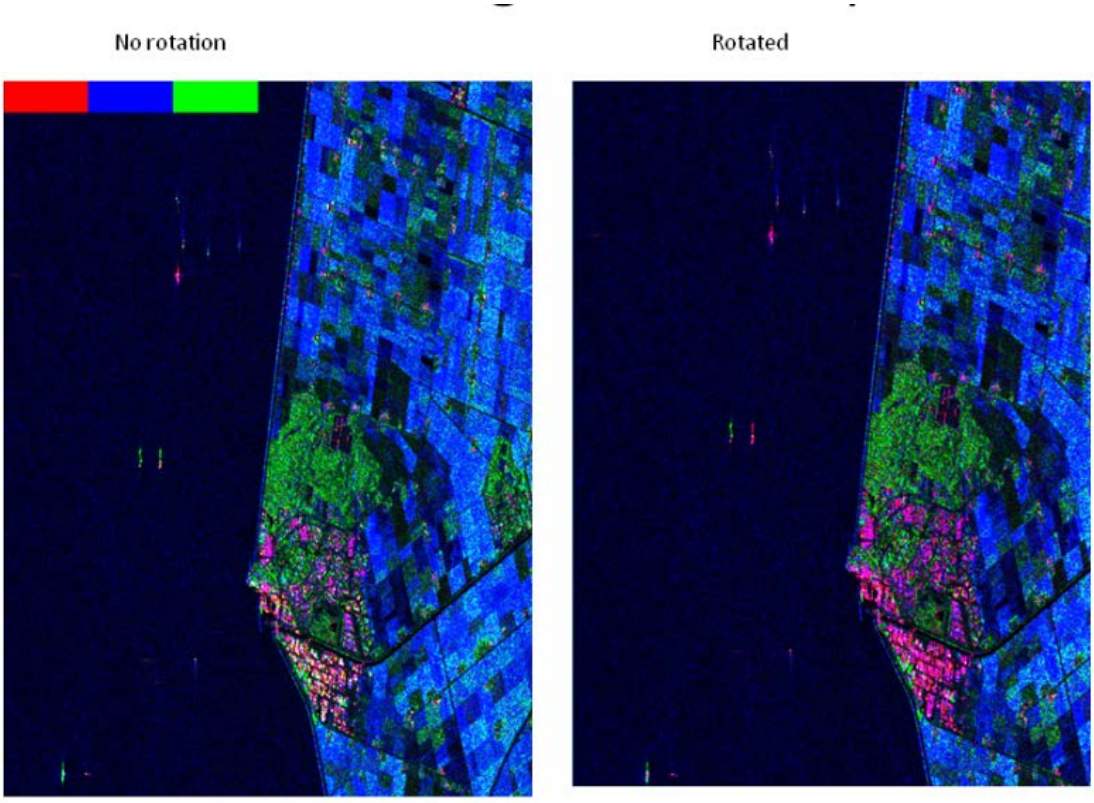

Figure 2.5 Yamaguchi decomposition standard (left) and rotated (right) over Flevoland, Netherlands.

2.2 Coherent decompositions

Coherent decomposition methods aim at expressing the measured scattering matrix, *S*, by combining basis matrices based on canonical scattering mechanisms [6]:

$$S = \sum_{k=1}^{N} \alpha_k S_k \tag{2.47}$$

Each scattering matrix (*S*) represents a single target. One problem with coherent decomposition methods is that they don't take into account speckle noise, which is usual in Single Look Complex (SLC) data. To reduce the problem of complex random multipliers, some kind of speckle filter has to be applied. The data have to be averaged in some way. The coherent decomposition methods are useful if only one dominant target component is expected. There are many ways to decompose a scattering matrix, *S*, and it is impossible to apply only one unique decomposition method. This is the second problem of coherent decomposition methods.

This chapter presents coherent decomposition methods: the Pauli decomposition method (chapter 2.2.1), a fusion of individual polarimetric channels (chapter 2.2.1), the Circular basis decomposition method (chapter 2.2.2) and the Krogager decomposition method (chapter 2.2.3).

2.2.1 Pauli decomposition

The Pauli decomposition method is well known, and it gives components of surface scattering (*HH+VV*), volume scattering (HV or VH) and double bounce (*HH-VV*). An example is shown in Figure 2.6 where six vessels in the Norne field, west of the coast of central Norway, are shown. They appear as brighter targets (bright green) against the ocean background. The oil production vessel, Norne FPSO (260 m long), is shown third from the top. The three different scattering components are displayed in different colours, and two scaling factors have been used here, *sc1 = 0.7* and *sc2 = 2*. The surface scattering is odd bounce (surface, sphere or corner reflector), displayed in blue and scaled with scaling factor *sc1*: *(HH+VV) ^ 0.7*. The double bounce is even bounce (dihedral or double bounce), displayed in red and scaled with scaling factor *sc1*: *(HH-VV) ^ 0.7*. The volume scattering is even bounce (i.e. dihedral tilted 45 degrees), displayed in green and scaled with both scaling factors: *($\sqrt{2}$ × (HV+VH)) ^ 0.7* [12].

Figure 2.7 shows an example of ships and ship wakes in a segment of a RADARSAT-2 image from the Strait of Gibraltar, with the individual scattering mechanisms shown separately. The figure shows how double bounce reflections *HH-VV* from the ocean surface are almost non-existent, whereas the surface scattering *HH+VV* and the *VV*-polarisation scattering from the ocean is quite strong. The figure also shows an example of HH-polarisation displayed in red, *HV*-polarisation displayed in green and *VV*-polarisation displayed in blue where it is possible to see both ship wakes and ships clearly.

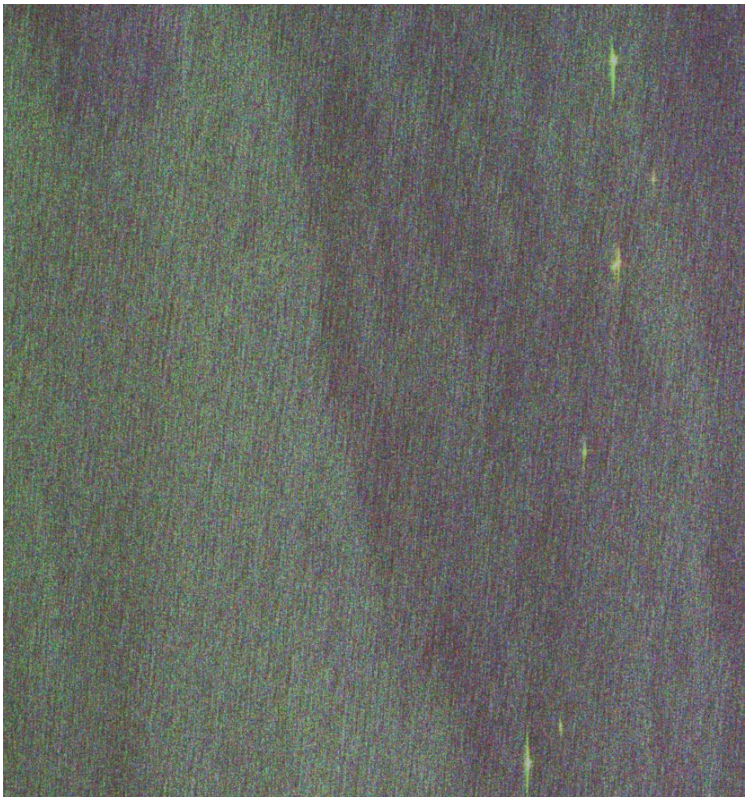

Figure 2.6 Pauli decomposition of six vessels in the Norne field and the ocean in the background. The vessels are clearly visible. The Norne FPSO oil production vessel is third from the top.

It is possible to fuse a combination of the different polarisations to enhance the ship to sea contrast [13]:

$$(HH - VV) \times HV \tag{2.48}$$

This represents a fusion of information from double bounce and cross-polarisation, which should maximise the observed signal reflected from ships, while suppressing the ocean clutter. Figure 2.8 shows the same segment as in Figure 2.7, but here for double bounce, the combined case, *HH*-polarisation and *HV*-polarisation (volume scattering). The ship to sea contrast is best for the combined case *(HH-VV)×HV*. Figure 2.9 shows a segment of a RADARSAT-2 Fine quad-polarisation image over Flevoland, the Netherlands. One ship is clearly more visible in the double bounce image compared to the volume scattering image. Figure 2.10 shows some vessels outside Vanouver, Canada in RADARSAT-2 polarimetric data (ERDAS is used). The vessels have strong reflection both in double bounce and surface scattering.

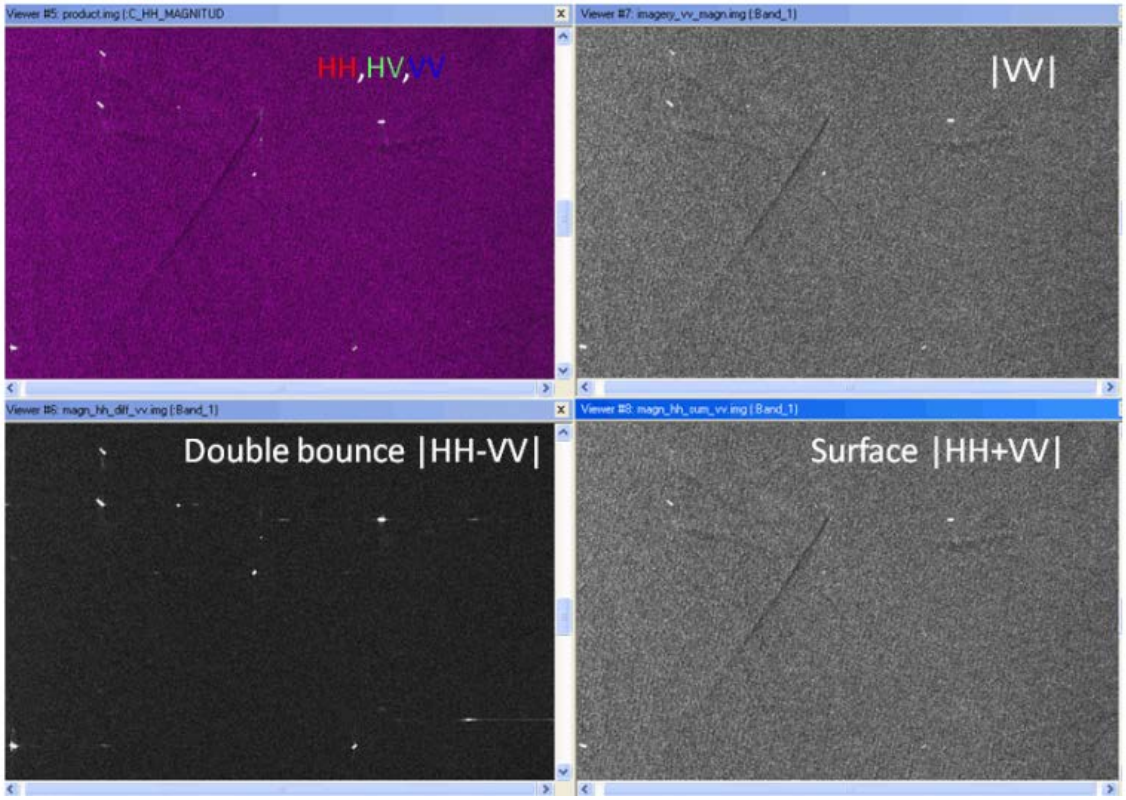

Figure 2.7 RADARSAT-2 polarimetric data from the Straits of Gibraltar showing vessels and ship wakes.

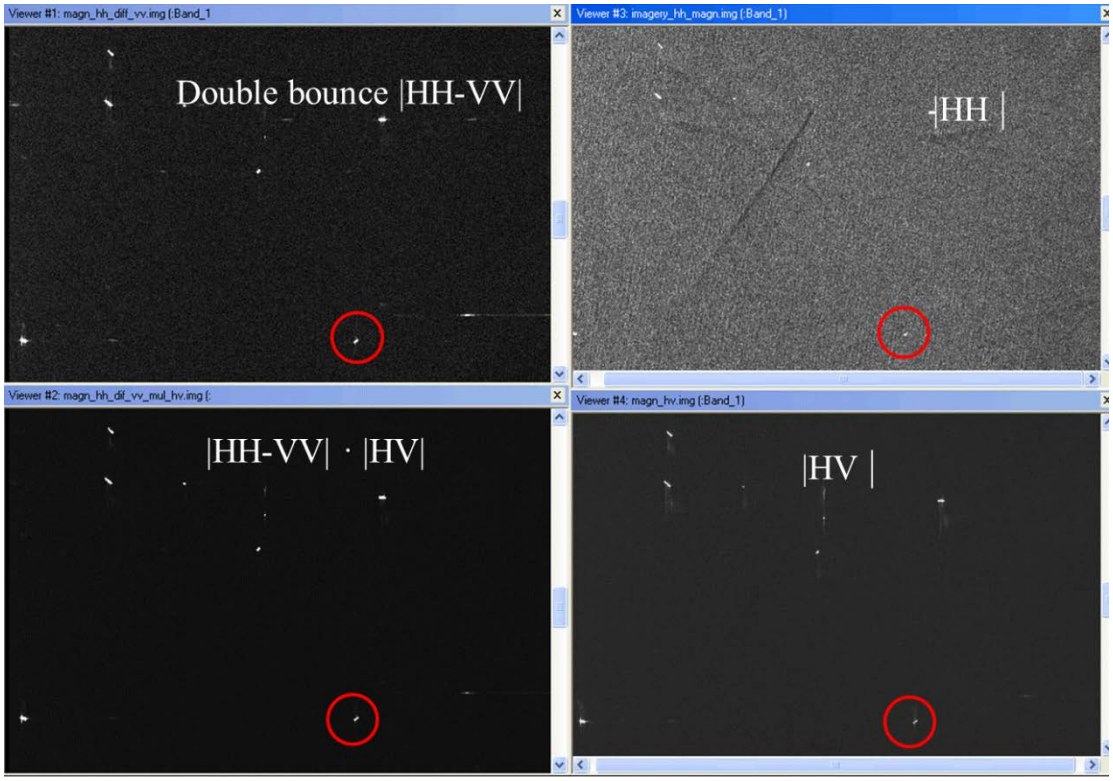

Figure 2.8 RADARSAT-2 polarimetric data from the Straits of Gibraltar showing vessels and ship wakes.

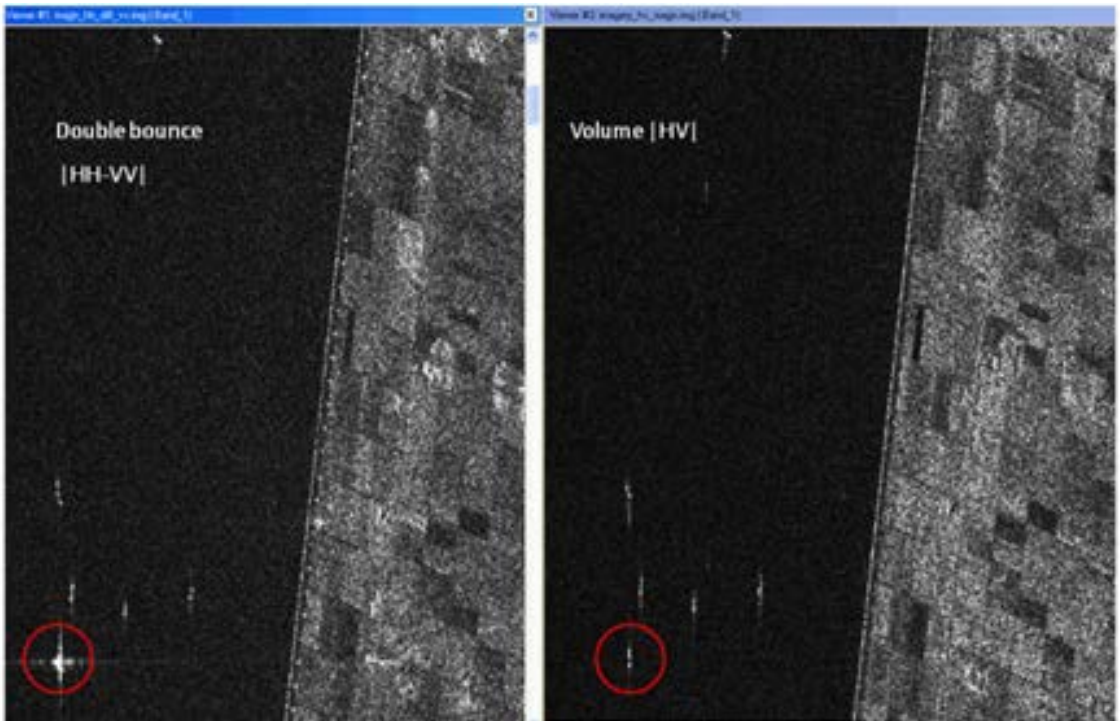

Figure 2.9 Pauli decomposition in a RADARSAT-2 Fine quad-polarisation image over Flevoland in the Netherlands. One ship is clearly best visible in the double bounce image.

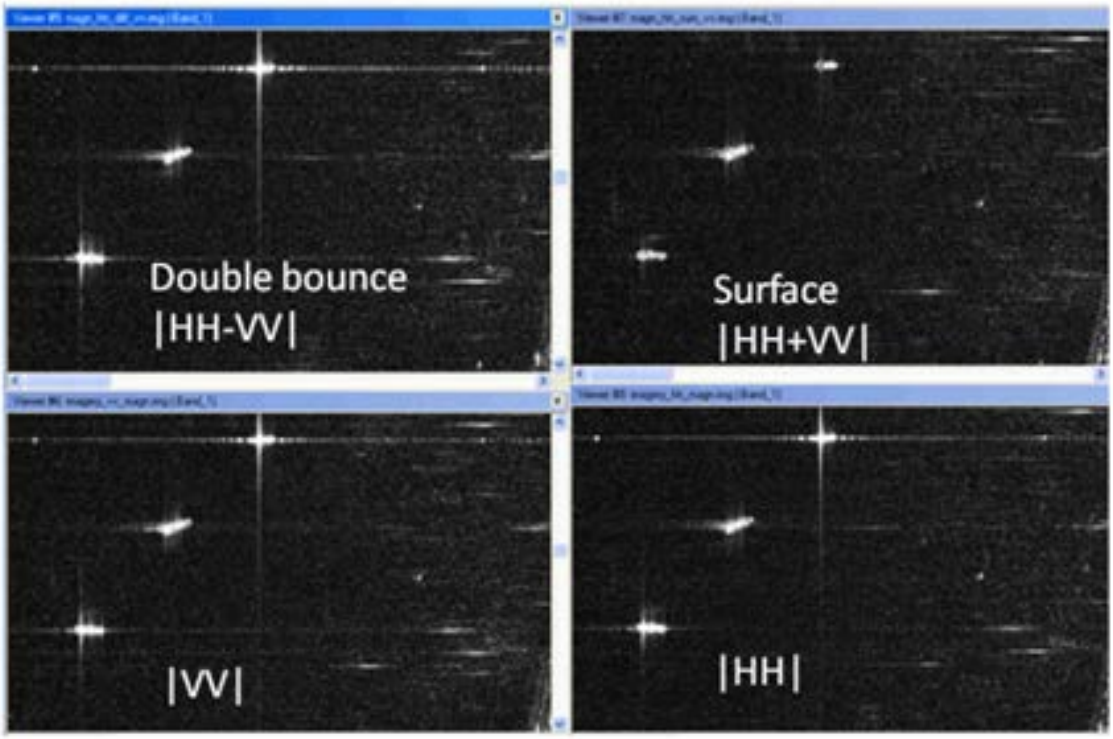

Figure 2.10 RADARSAT-2 polarimetric imagery, Vancouver, Canada. Ships have both strong double bounce and surface scattering.

2.2.2 Circular basis decomposition

Another decomposition method that can be used when fully-polarimetric data are available is the Circular basis decomposition as shown in equation (2.49) [13]. Multiplying out equation (2.49) gives equations (2.50)-(2.53). The S_{RL} (Right-Left) and S_{LR} (Left-Right) elements contain the double bounce (*HH-VV*) and the sum of the volume scattering components (*HV+VH*). The S_{RR} and S_{LL} elements contain surface scattering (*HH+VV*). It is expected that the ocean surface scattering is suppressed in the double bounce case. In the surface scattering channels, we expect to see more surface waves, oceanographic phenomena and ship wakes.

$$\begin{bmatrix} S_{RR} & S_{RL} \\ S_{LR} & S_{LL} \end{bmatrix} = \frac{1}{2}\begin{bmatrix} 1 & -i \\ -i & 1 \end{bmatrix}\begin{bmatrix} S_{HH} & S_{HV} \\ S_{VH} & S_{VV} \end{bmatrix}\begin{bmatrix} 1 & i \\ i & 1 \end{bmatrix} \tag{2.49}$$

$$|S_{RR}| = \frac{1}{2}(S_{HH} + S_{VV} + i(S_{HV} - S_{VH})) \tag{2.50}$$

$$|S_{RL}| = \frac{1}{2}(S_{HV} + S_{VH} + i(S_{HH} - S_{VV})) \tag{2.51}$$

$$|S_{LR}| = \frac{1}{2}(S_{HV} + S_{VH} + i(S_{VV} - S_{HH})) \tag{2.52}$$

$$|S_{LL}| = \frac{1}{2}(S_{HH} + S_{VV} + i(S_{VH} - S_{HV})) \tag{2.53}$$

Figure 2.11 shows RADARSAT-2 polarimetric data from the Strait of Gibraltar. The radar image segments are shown using Circular basis decomposition made in ERDAS. The *RR* and *LL* components shows a clear ship wake and vessels, while the *RL* and *LR* components suppress the sea and the vessels become more visible.

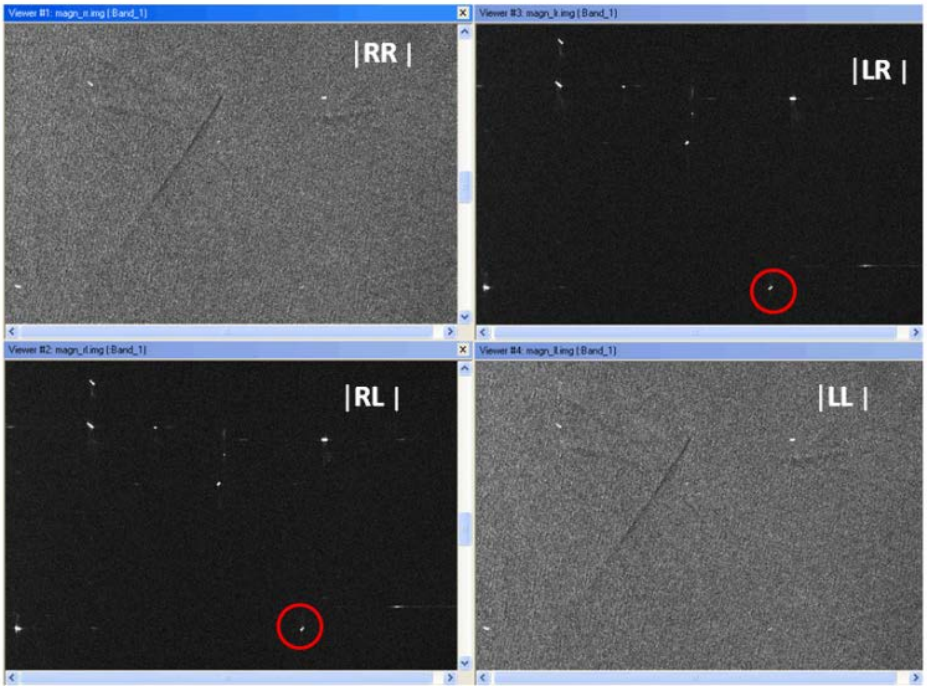

Figure 2.11 RADARSAT-2 polarimetric data from the Straits of Gibraltar.

2.2.3 Krogager decomposition

Krogager decomposition method involves decomposing the symmetric scattering matrix, *S*, into three coherent components [6]. The three components are a sphere *(k_s)*, diplane *(k_d)* and helix (k_h) targets under a change of rotation, θ. The three components of the Krogager decomposition method and their relationship to the Circular basis method (see chapter 2.2.2) is given by [5]:

$$k_{sphere} = |KS_{RL}| \tag{2.54}$$

$$k^{+}_{diplane} = |KS_{LL}| \quad ; \quad k^{-}_{diplane} = |KS_{RR}| \tag{2.55}$$

$$k^{+}_{helix} = |KS_{RR}| - |KS_{LL}| \quad ; \quad k^{-}_{helix} = |KS_{LL}| - |KS_{RR}| \tag{2.56}$$

If $|KS_{RR}|$-$|KS_{LL}|$ is positive, $k^{+}_{diplane}$ and k^{+}_{helix} will be used. If $|KS_{RR}|$-$|KS_{LL}|$ is negative, $k^{-}_{diplane}$ and k^{-}_{helix} will be used [5]. Transformation from linear to circular elements are done by these formulas:

$$KS_{RR} = iS_{HV} + \frac{1}{2}(S_{HH} - S_{VV}) \tag{2.57}$$

$$KS_{LL} = iS_{HV} - \frac{1}{2}(S_{HH} - S_{VV}) \tag{2.58}$$

$$KS_{RL} = \frac{i}{2}(S_{HH} + S_{VV}) \tag{2.59}$$

Figure 2.12 shows RADARSAT-2 polarimetric data from the Straits of Gibraltar. ERDAS is used to make the segments showing the Krogager decomposition method. The image segment to the upper left shows *HH* in red, *3×HV* in green and *VV* in blue.

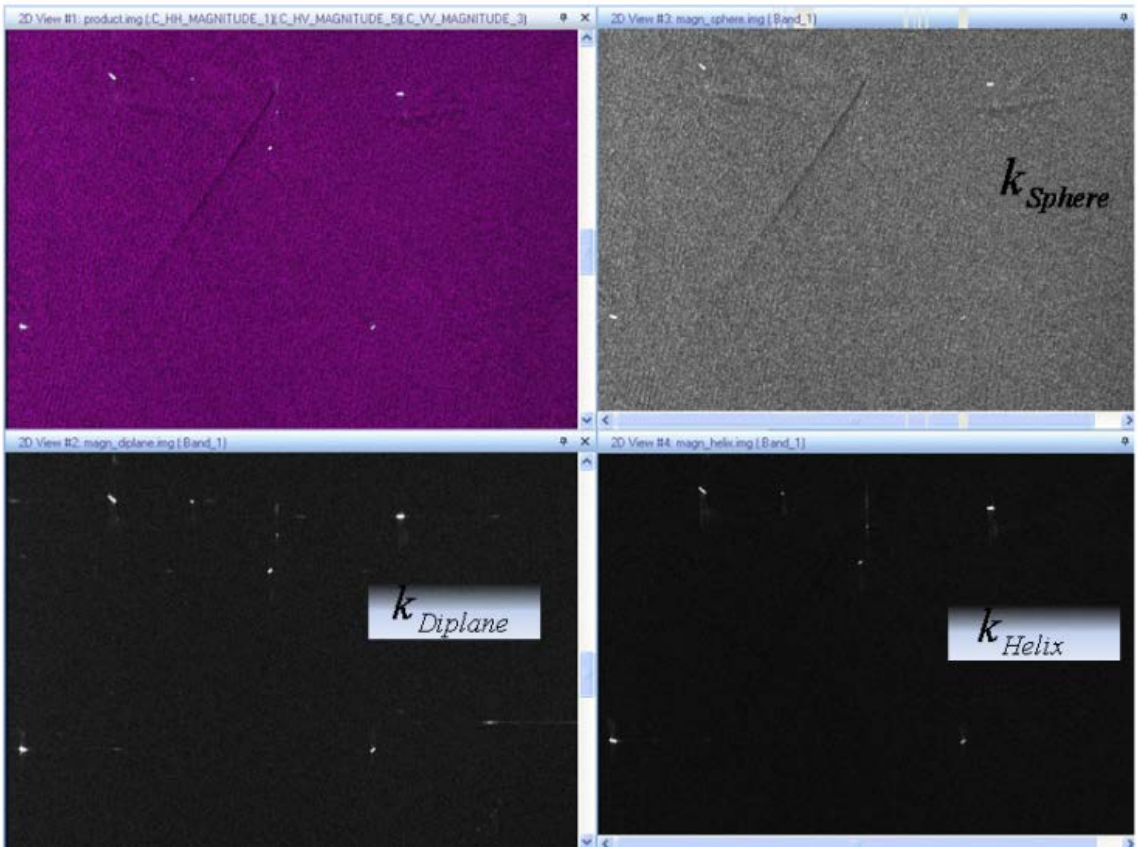

Figure 2.12 RADARSAT-2 polarimetric data from the Straits of Gibraltar shown using Krogager decomposition method.

2.3 Representing polarimetric data

Table 2.1 shows four different ways of representing polarimetric data [12]. The *HV*-channel is multiplied with a factor 3 in linear representation so it can be visible in the colour combination. *HV+VH* is amplified compared to co-polarisation to make it visible. The Circular and Krogager decomposition methods have no weighting. Examples of these presentations will be shown in this report.

	Red	Green	Blue
Linear	*3×HV*	*HH*	*VV*
Pauli	*(HH-VV) ^ 0.7*	*($\sqrt{2}$ ×(HV+VH)) ^ 0.7*	*(HH+VV) ^ 0.7*
Circular	*RL*	*RR*	*LL*
Krogager	k_{sphere}	$k_{diplane}$	k_{helix}

Table 2.1 Four different ways to represent polarimetric data.

3 Polarimetric decompositions and results

This chapter presents test results from using RADARSAT-2 images over the Norne field, west of the coast of central Norway. The Norne Field is a large oil and gas field on the Norwegian continental shelf. The oil from the field is loaded onto a tanker and transported to the market. The oil production and cargo ship Norne FPSO is used constantly on the field and is moored to a template on the ocean floor (see Figure 3.1). Norne FPSO can rotate freely around a mooring mid-ship, so the bow is always facing the dominant on-coming waves. Norne FPSO is 260.2 m long, 41.0 m wide and 25.0 m high. Often, other vessels and oil platforms are in the area around Norne, and can be analysed also.

Figure 3.1 Illustration and image of the oil production vessel Norne FPSO. Source: Statoil

Information about the oil platform and other ships in the Norne Field has been obtained from Statoil [14] to be sure which oil platforms and vessels that are in the imaged area. In addition AIS data have been obtained from aisonline.com [15]. The ships' position, identification and length can be obtained from the AIS data.

The maximum amplitude of a vessel compared with the background sea clutter has been investigated for ships with known structure and length together with how these conditions depend on the imaging geometry.

Figure 3.2 shows the distribution of vessels sizes of 2673 vessels during 6 months in the Norwegian Sea and Barents Sea north of 71°N. The figure shows that there were no vessels above 350 m inside the area during half a year.

Three different vessel sizes have been used in the study presented in the report: large, medium and small. Norne FPSO is defined as a large vessel. Eddy Fauna (108 m), Island Wellserver (116 m) and Vlas Nichkov (152 m) are defined as medium sized vessels (see Figure 3.3). Ocean Prince (65 m), Ocean King (75 m) and Far Star (84 m) are defined as small sized vessels (see Figure 3.4).

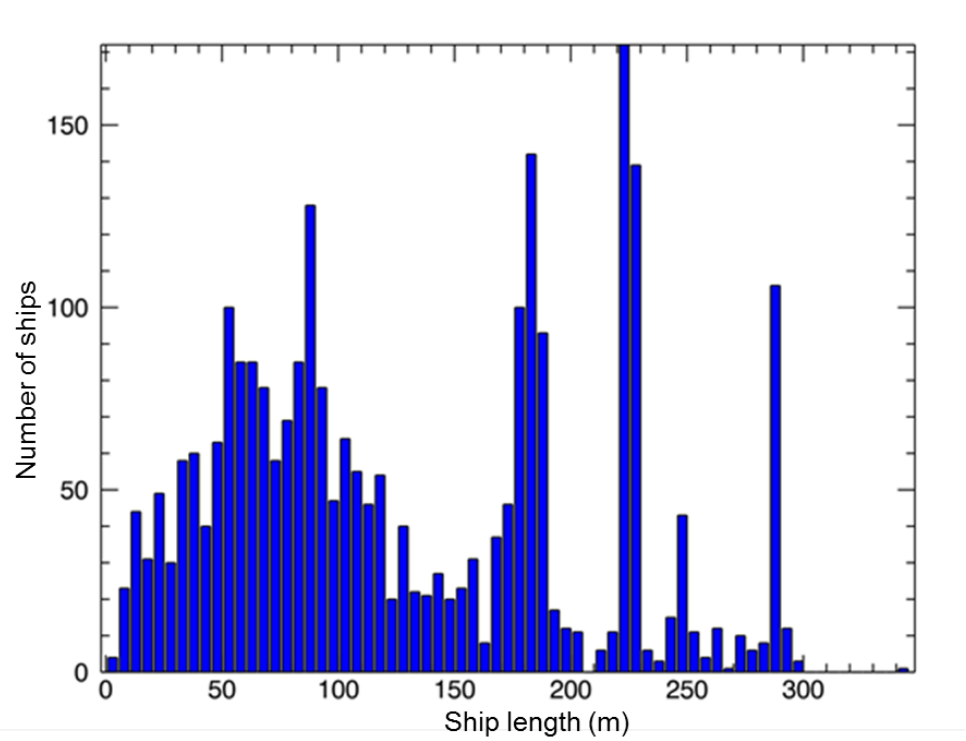

Figure 3.2 Distribution of vessel sizes in the Northern areas north of 71°N (Reference: AISSat-1 data, FFI).

Figure 3.3 Eddy Fauna (top left), Island Wellserver (top right) and Vlas Nichkov (bottom). Source: marinetraffic.com

Figure 3.4 Ocean Prince (top left), Ocean King (top right) and Far Star (bottom). Source: marinetraffic.com

3.1 Manual analysis

26 RADARSAT-2 ScanSAR dual-polarisation and 24 RADARSAT-2 quad-polarisation images have been analyzed. The different polarisations and polarisation combinations have been compared for automatic and manual ship detection for three different vessel sizes as well as for ice detection versus vessel detection. Some results are shown in this report.

3.1.1 Dual-polarisation

Figure 3.5 shows signatures of the oil production vessel Norne FPSO outside the west coast of Norway on June 30th 2010. The vessel is shown in 3D presentation in *HH*-, *HV*-polarisation and in the combined case *HH*×*HV*. The contrast is best when combining the two polarisation channels. The contrast between the maximum value of the vessel divided by the mean sea background is 47 for HH-polarisation, 34 for HV-polarisation and 975 for the combined case. The incidence angle for Norne FPSO is 35.3°.

Figure 3.6 shows signatures of vessels and the sea background of the Norne field outside the west coast of Norway on March 31st 2010. The vessels are shown in 3D presentation in *VV*-, *VH*-polarisation and in the combined case *VV*×*VH*. The contrast is best when combining the two polarisation channels, but VH-polarisation also gives good contrast. The contrast between the maximum value of Norne FPSO divided by the mean sea background is 9 for *VV*-polarisation, 35 for *VH*-polarisation and 40 for the combined case.

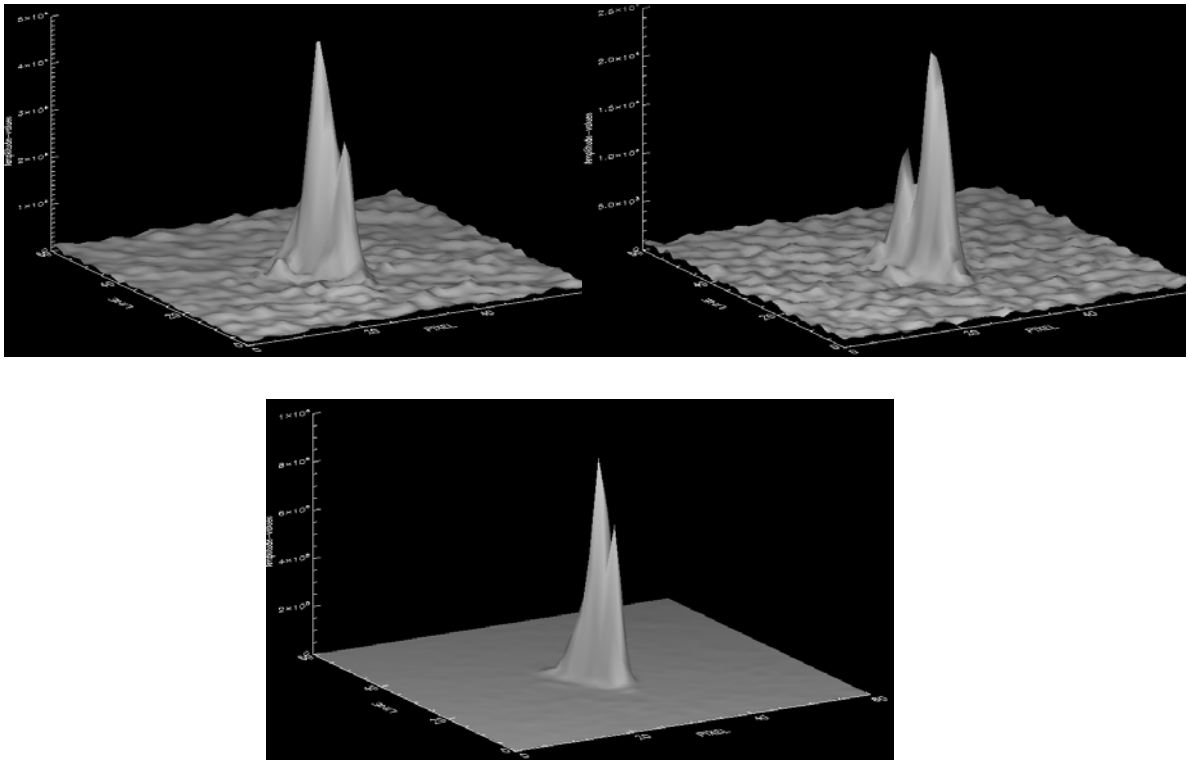

Figure 3.5 Signature of Norne FPSO in VV-channel (top left), VH-channel (top right) and the combined case (bottom).

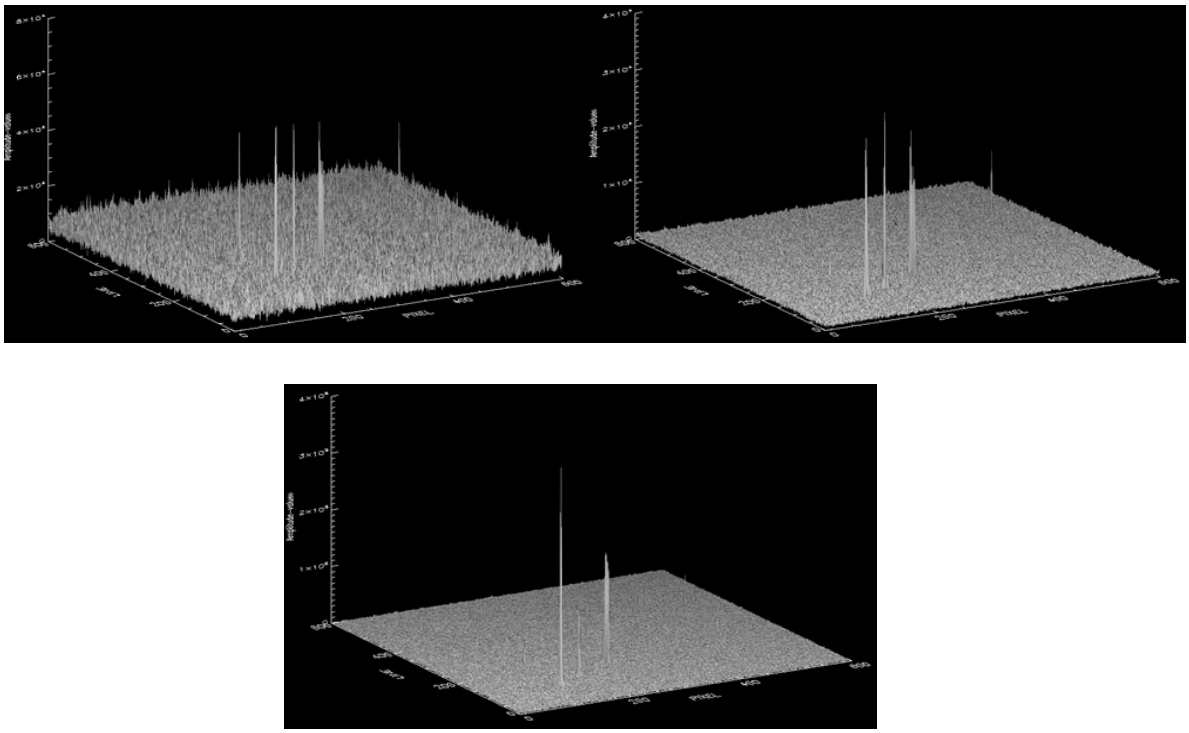

Figure 3.6 3D reflections of vessels and the sea background in a 600 pixels × 600 pixels segment. The VV-channel is shown at the top left, the VH-channel at the top right and the combined case at the bottom.

Table 3.1 shows maximum amplitude of Norne FPSO divided by mean sea for 26 RADARSAT-2 dual-polarised images.

					R = Maximum amplitude / mean sea			
Date	***Time***	***Mode***	***A/D***	***Inc. angle***	***HH***	***VV***	***HV/VH***	***Sqrt (co× cross)***
14/4-10	16:39:35	SCN	A	23,5		3	7	16
25/6-10	16:39:37	SCN	A	23,5	5		27	107
26/6-10	06:18:08	SCN	D	23,7	13		11	133
15/4-10	06:18:07	SCN	D	23,7		2	6	5
7/4-10	16:43:44	SCN	A	26,4		7	32	253
12/7-10	16:43:01	SCN	A	26,4	7		22	152
23/12-09	06:14:02	SCN	D	26,6	9		22	199
22/4-10	06:13:58	SCN	D	26,7		36	30	801
31/3-10	16:47:54	SCN	A	29,3		8	32	249
5/7-10	16:47:10	SCN	A	29,3	15		27	335
24/4-10	16:47:56	SCN	A	29,3		15	27	352
10/7-10	06:09:47	SCN	D	29,4	19		35	642
30/12-09	06:09:52	SCN	D	29,5	8		27	202
28/6-10	16:51:21	SCN	A	32,2	33		23	630
24/3-10	16:52:04	SCN	A	32,2		53	22	912
17/4-10	16:52:05	SCN	A	32,2		25	14	287
18/12-09	16:51:10	SCN	A	32.3	16		18	232
12/4-10	06:05:37	SCN	D	32,4		7	27	112
23/6-10	06:05:38	SCN	D	32,4	59		39	2828
20/12-09	06:01:09	SCW	D	33,7	8		10	105
10/4-10	16:56:14	SCN	A	35,2		23	45	544
21/6-10	16:55:31	SCN	A	35,2	8		19	148
30/6-10	06:09:52	SCN	D	35,3	47		34	975
19/4-10	06:01:27	SCN	D	35,3		13	30	376
3/4-10	17:00:24	SCN	A	38.1		21	26	507
14/12-09	17:08:56	SCW	A	41,5	41		23	884

Table 3.1 Maximum amplitude divided by mean sea for 26 RADARSAT-2 dual-pol images.

In most cases there are evident improvements of the ship to sea contrast when combining the polarisation channels for ship detection for low incidence angles. The improvements of the ship to sea contrasts when combining the polarisation channels for ship detection for medium and high incidence angles are very clear. Figure 3.7 shows maximum amplitude divided by mean sea for *HH*-, *VV*- and for *HV*- or *VH*-polarisation. *HH*- polarisation gives better contrast than *VV*-polarisation for all incidence angles. Cross-polarisation mostly gives better results for low and medium incidence angles. For higher incidence angles the cross-polarisation contrasts are somewhere in the middle of the co-polarisation contrasts. Figure 3.8 shows maximum amplitude divided by mean sea for *HH*- or *VV*-polarisation and for *HV*- or *VH*-polarisation. It seems that the cross-polarisation contrasts are more independent of the incidence angle, except for incidence angles below 25°. Then the contrasts for both co- and cross-polarisation are low. For all incidence angles *HH*- and *VV*-polarisation have more contrasts that are low than cross-polarisation has. Cross-polarisation seems to give more stable results and it seems that it is easier to detect vessels independently of the incidence angle. For higher incidence angles, all contrasts are above 10 for cross-polarisation.

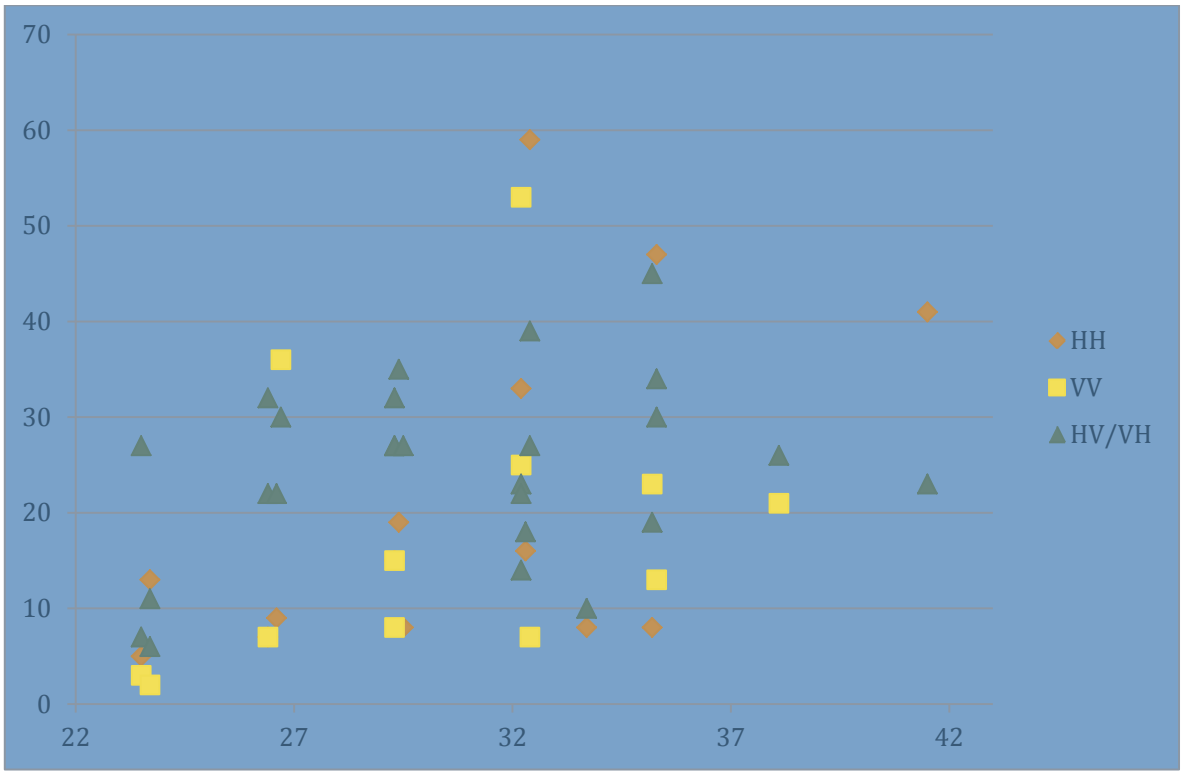

Figure 3.7 Maximum amplitude divided by mean sea for HH-, VV- and for HV- or VH-polarisation for Norne FPSO in RADARSAT-2 ScanSAR dual-polarised images.

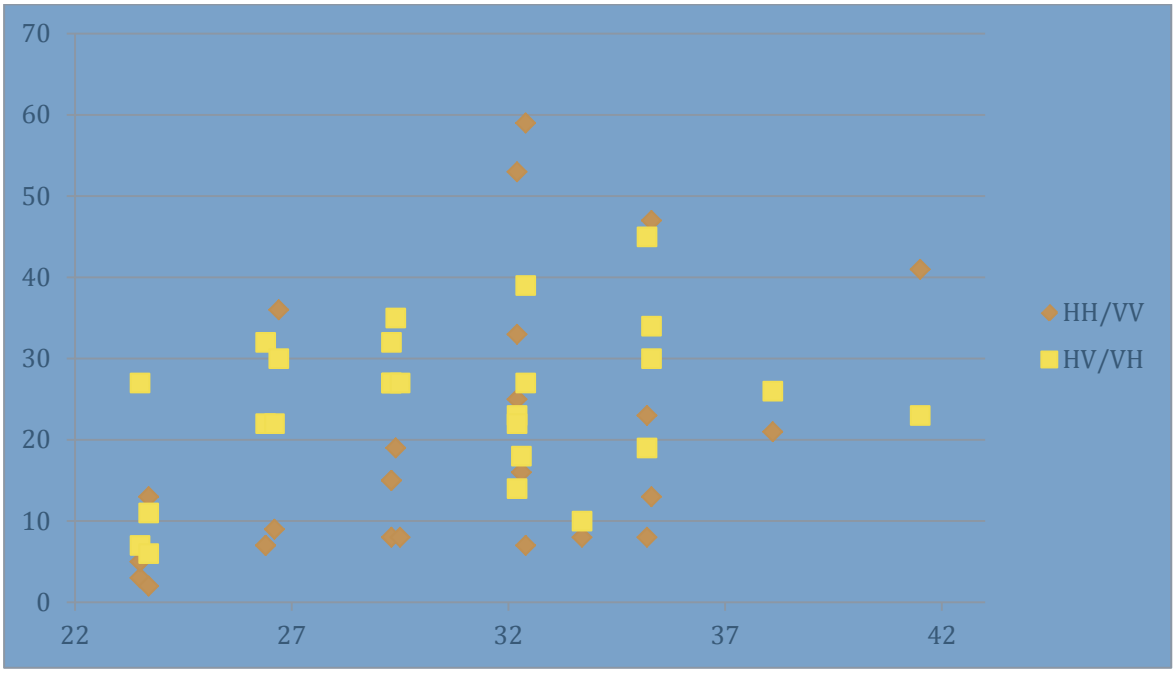

Figure 3.8 Maximum amplitude divided by mean sea for HH-/VV- and for HV- or VH-polarisation for Norne FPSO in RADARSAT-2 ScanSAR dual-polarised images.

3.1.2 Quad-polarisation and ship detection

Figure 3.9 shows examples of different polarimetric decompositions, including land, sea and sea ice. The figure shows a segment from the Oslofjord on February 7th 2010. Ice is visible in the fjord in a different colour than the ocean background. The example shows how buildings, ships and natural features scatter differently in different polarisation channels. The Pauli decomposition, Krogager decomposition and Yamaguchi decomposition methods are shown. Especially the Yamaguchi decomposition shows that the forest exhibits mostly volume scattering (green) and agricultural fields are dominated by surface scattering (blue) while most of the double bounce scattering (red) comes from buildings and manmade objects.

Figure 3.10 shows segments of a RADARSAT-2 quad-polarisation image from December 1st 2009 at low incidence angle, approximately 30 degrees. It is shown that the vessels are more visible in cross-polarisation and when combining the polarisation channels for quad-polarised data. The vessels shown are at the bottom Norne FPSO (260 m), Skandi Mongstad (97 m) to the left, Ocean Prince (65 m) to the right and oil platform Stena Don (96 m) at the top.

Figure 3.11 shows segments of a RADARSAT-2 quad-polarisation image from November 29th 2009. The figure shows the differences between scattering from vessels and the ocean background in double bounce (*HH-VV*), surface scattering (*HH+VV*), cross-polarisation (*HV*) and double bounce × cross-pol (*(HH-VV)×HV*). Norne FPSO is at incidence angle 27.3°.

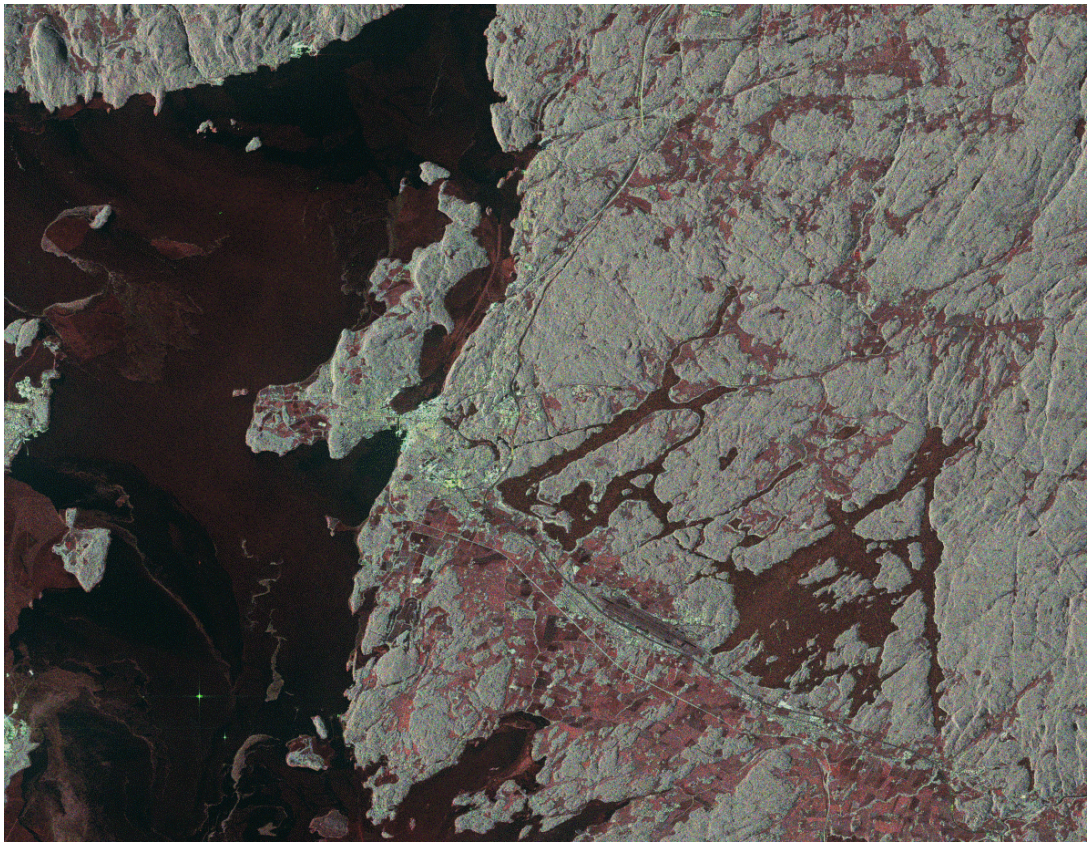

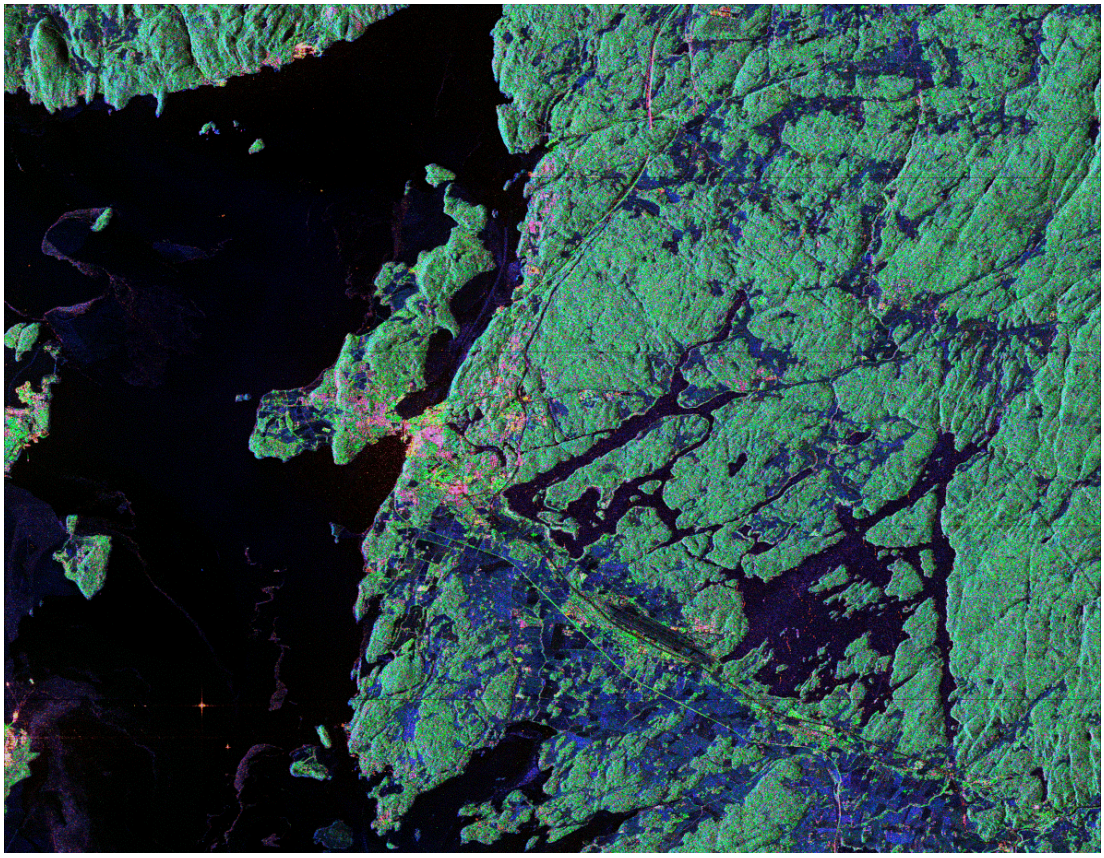

Figure 3.9 Segments from the Oslofjord when combining radar images in different polarisation combinations using RADARSAT-2 Standard quad-polarisation mode on February 7th 2010. The four different polarisation channels have been combined using the Pauli decomposition method (top previous page), the Krogager decomposition method (bottom previous page) and the Yamaguchi decomposition method (this page).

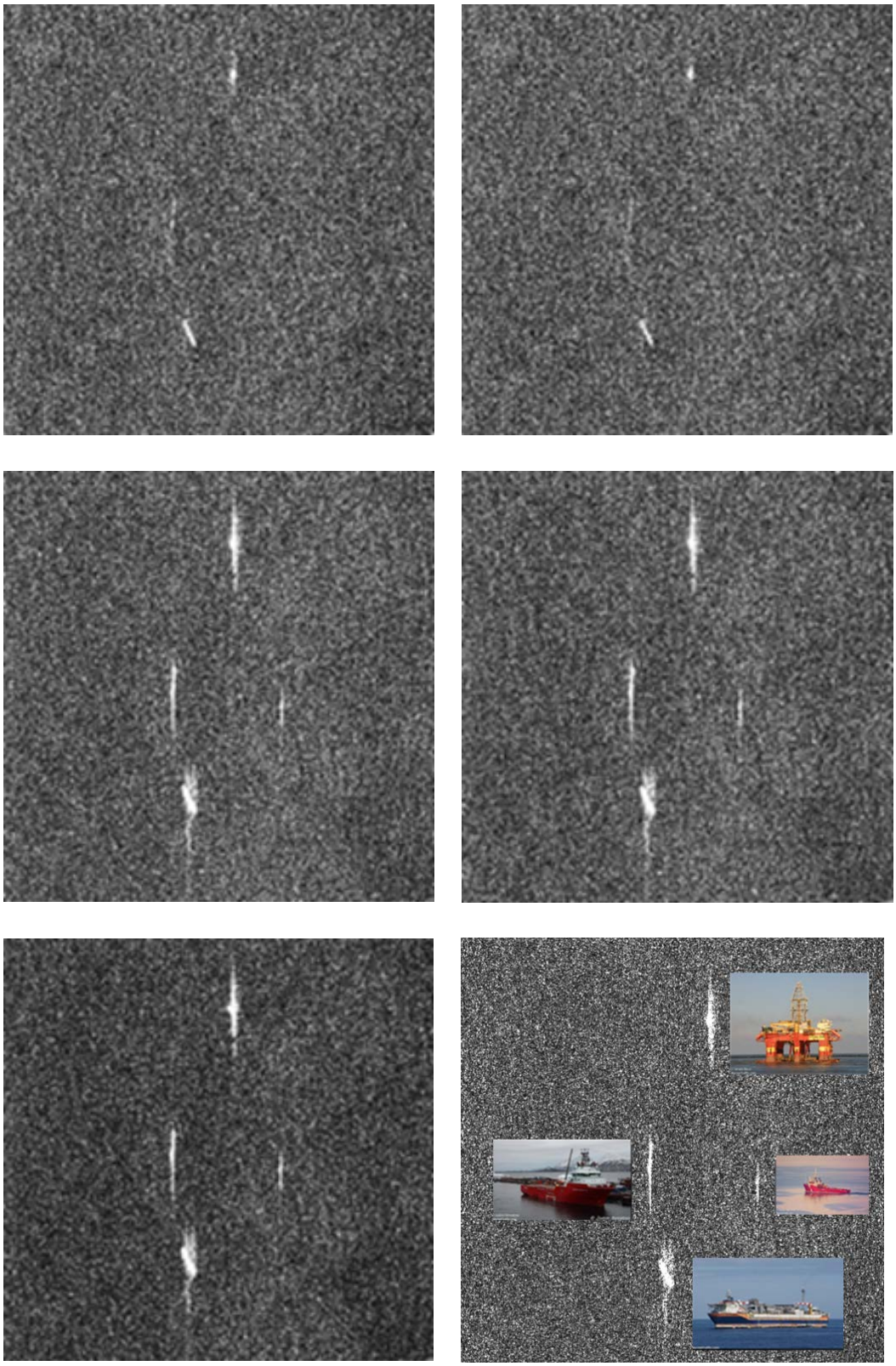

Figure 3.10 Segments of RADARSAT-2 quad-polarisation data from December 1st 2009 in different polarisations: HH (top left), VV (top right), HV (middle left), VH (middle right) and (HH-VV)×HV (bottom left). The different vessels are shown at the bottom right.

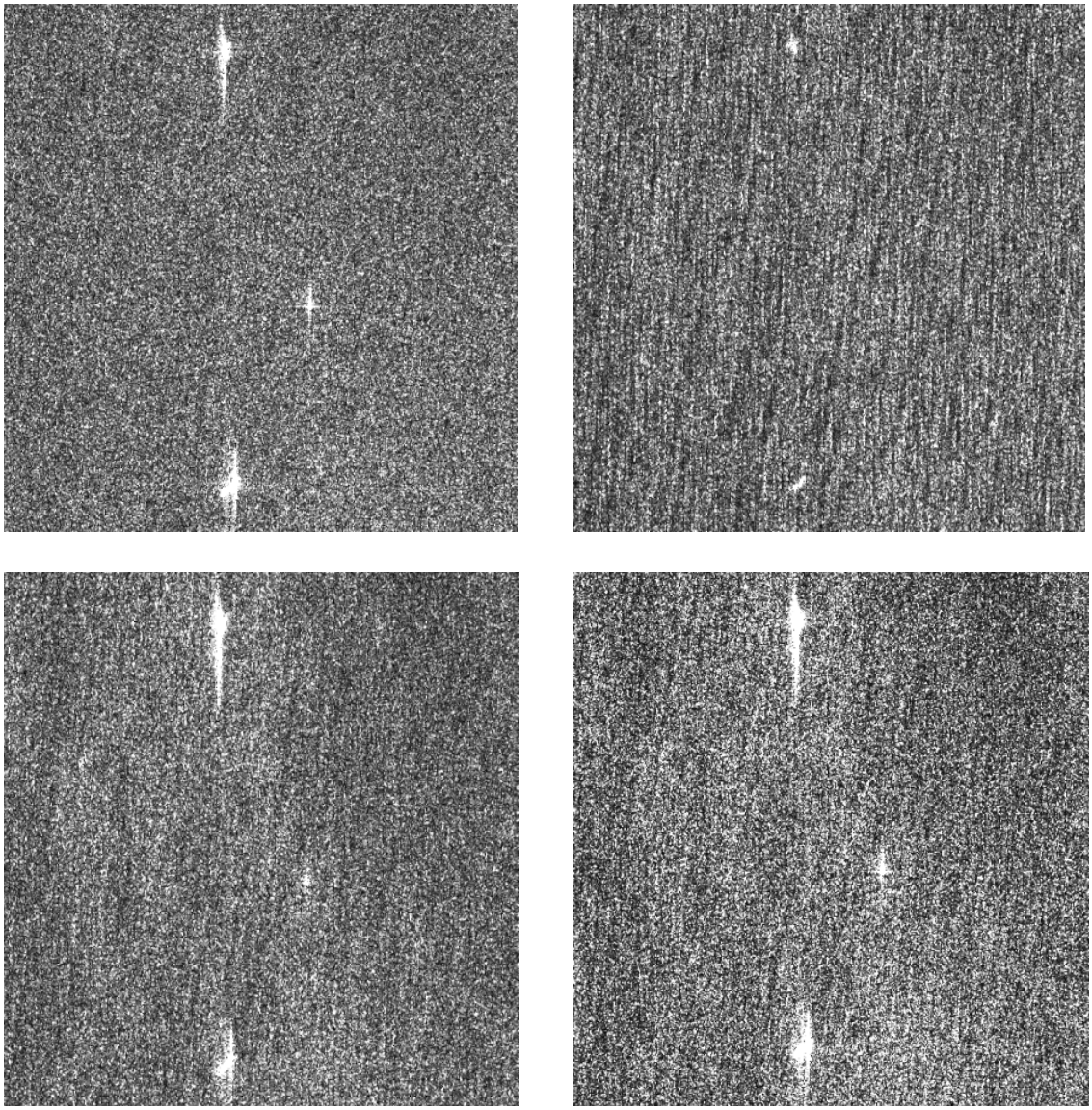

Figure 3.11 Segments of RADARSAT-2 quad-polarisation data from November 29th 2009 in different polarisation combinations: HH-VV (top left), HH+VV (top right), HV (bottom left) and (HH-VV) × HV (bottom right).

Figure 3.12 - Figure 3.15 shows a segment of 600 pixels × 600 pixels of a RADARSAT-2 Standard quad-polarisation image on December 10th 2009. The figures show how the 3D-reflections differ in the different polarisation channels and polarisation combinations. Figure 3.12 shows: *HH, VV, HH-VV* (double bounce) and *(HH-VV)×HV* (double bounce times volume scattering). Norne FPSO is at the top, Ocean Prince in the middle to the left and Skandi Mongstad (vessel) and Stenda Don (oil platform) are at the bottom (lying close together). It looks like Skandi Mongstad and Stena Don are one object since they are so close together. Figure 3.13 shows signatures after using the Circular basis decomposition method, *RR* and *RL*, Figure 3.14 shows signatures after using the Krogager decomposition method, while Figure 3.15 shows signatures after using the Yamaguchi decomposition method with rotation. Surface waves are visible in Yamaguchi surface rotated. Norne FPSO is at 40.9°.

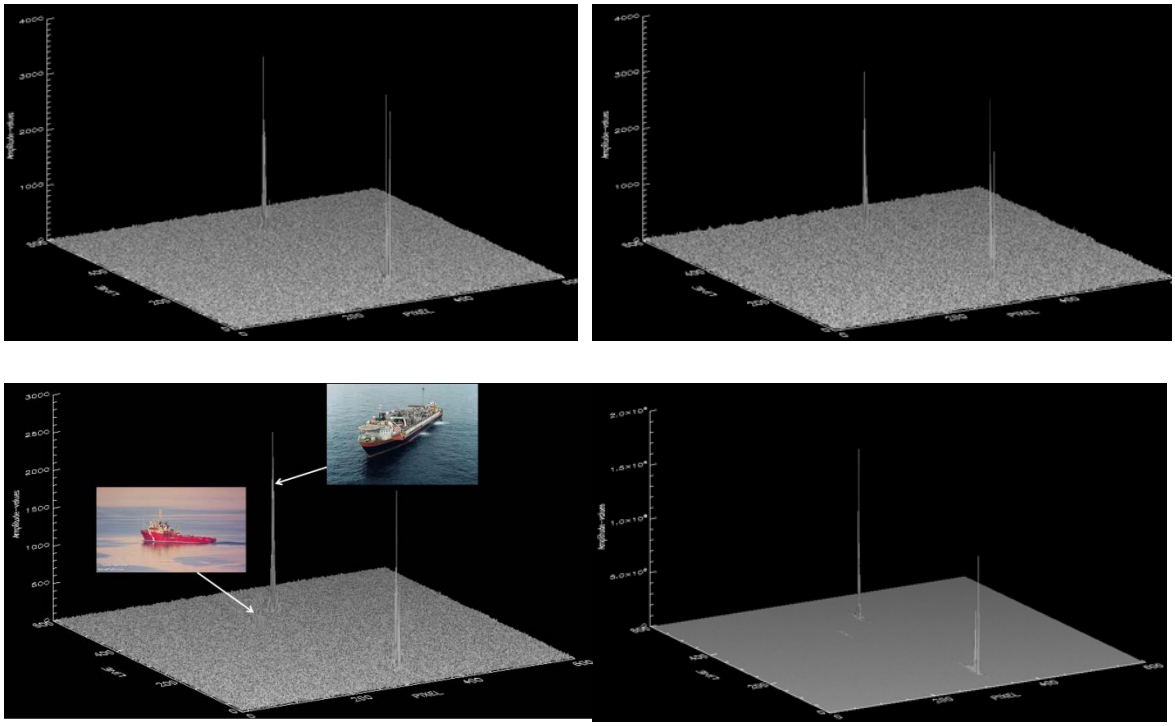

Figure 3.12 Segments of RADARSAT-2 quad-polarisation data on December 10th 2009 in different polarisations and polarisation combinations: HH (top left), VV (top right), HH-VV (bottom left), (HH-VV)×HV (bottom right). Norne FPSO and Ocean prince are shown with the arrows.

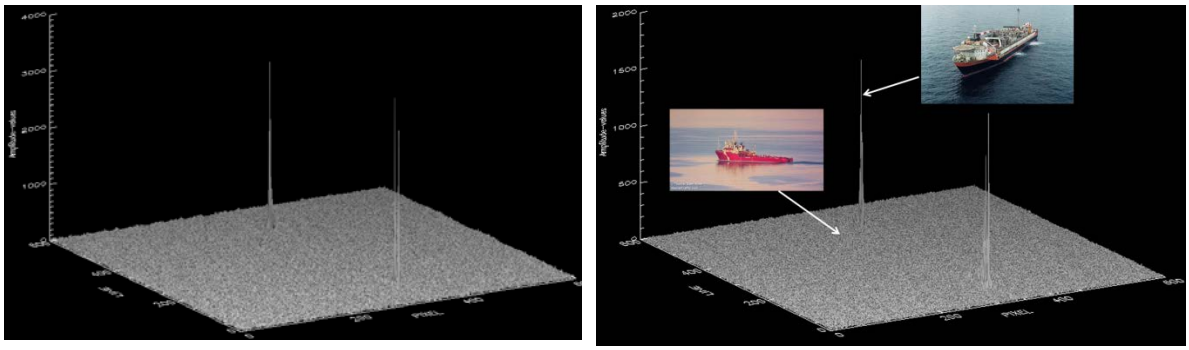

Figure 3.13 Segments of RADARSAT-2 quad-polarisation data on December 10th 2009 in Circular basis decomposition, RR (left) and RL (right). Norne FPSO and Ocean prince are shown with the arrows.

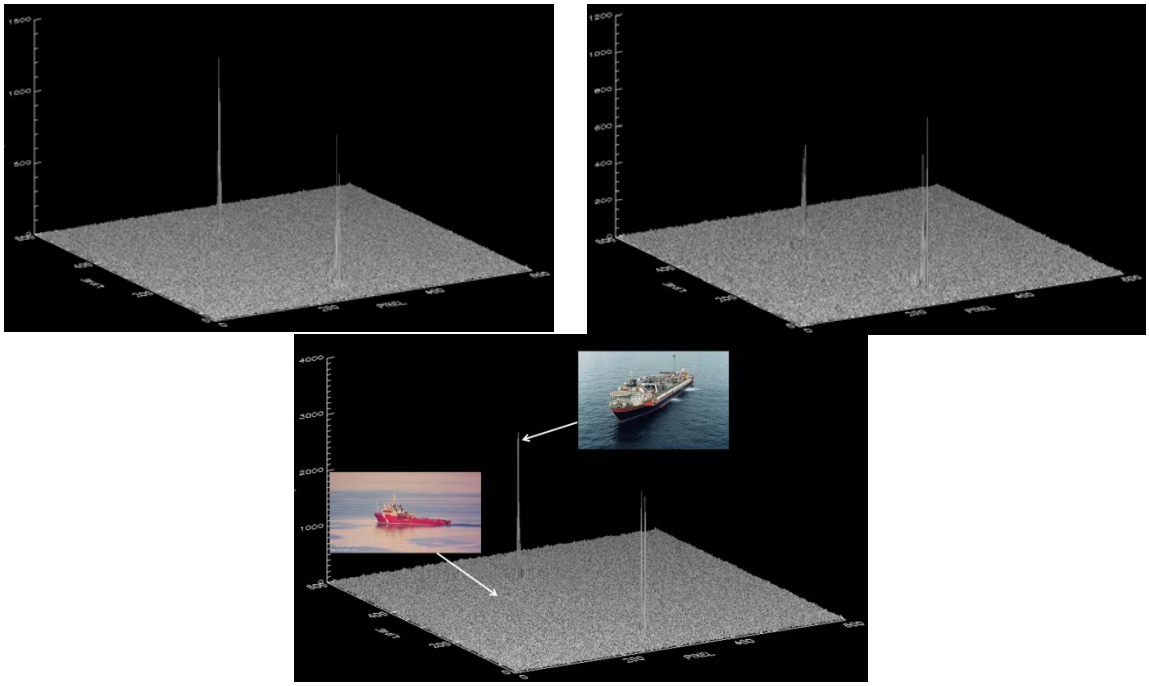

Figure 3.14 Segments of RADARSAT-2 quad-polarisation data on December 10th 2009 in Krogager decompositions: kDiplane (top left), kHelix (top right) and kSphere (bottom). Norne FPSO and Ocean prince are shown with the arrows.

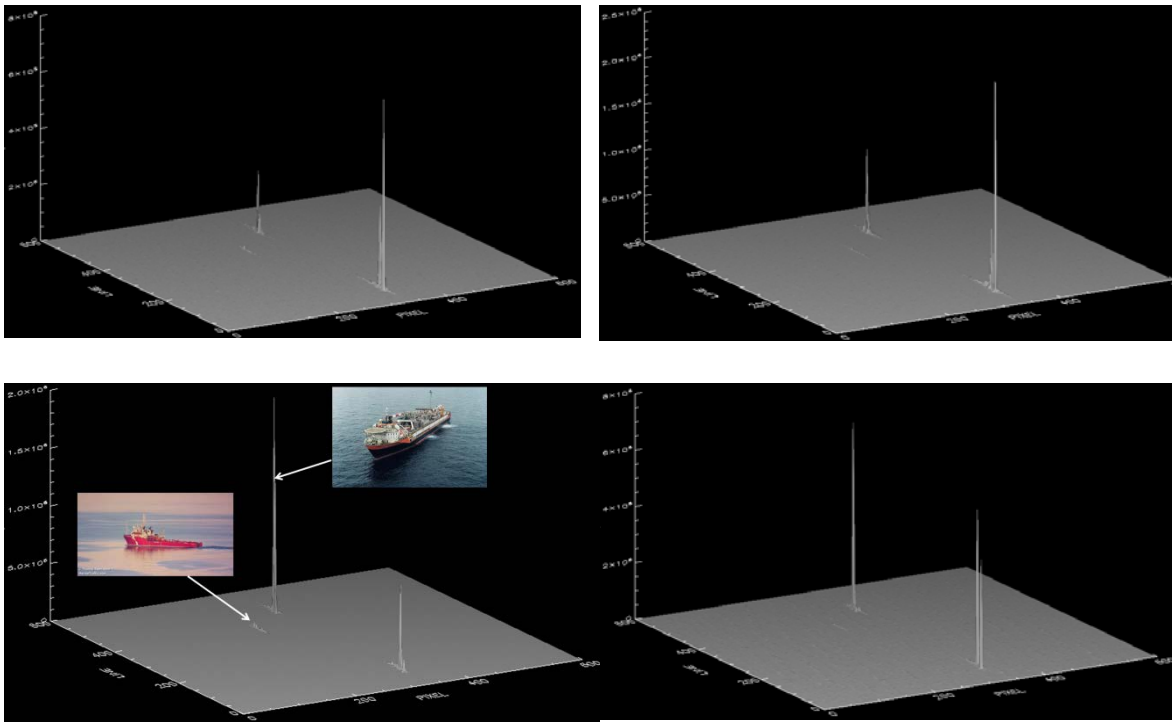

Figure 3.15 Segments of RADARSAT-2 quad-polarisation data on December 10th 2009 using Yamaguchi decomposition method: Yamaguchi helix rotated (top left), volume rotated (top right), double rotated (bottom left) and surface rotated (bottom right). Norne FPSO and Ocean prince are shown with the arrows.

Table 3.2 and Table 3.3 shows contrast measures of Norne FPSO and Ocean Prince for different polarisation channels and different polarisation combinations. The numbers indicate what we have seen in Figure 3.12 - Figure 3.15.

	Max. amplitude / mean sea	
Method	**Norne FPSO**	**Ocean Prince**
HH	193	18
VV	112	8
HV	123	22
VH	135	23
HH-VV	155	22
RR	150	8
RL	169	17
kSphere	150	8
kHelix	112	32
Sqrt((HH-VV)×HV)	149	20
Sqrt(Yamaguchi helix)	79	13
Sqrt(Yamaguchi volume)	81	11
Sqrt(Yamaguchi surface)	80	5
Sqrt(Yamaguchi double)	230	31
Sqrt(Yamaguchi double rot.)	234	29

Table 3.2 Maximum amplitude divided by mean sea for Norne FPSO on December 10th 2009.

	Max. intensity / mean sea intensity	
Method	**Norne FPSO**	**Ocean Prince**
HH^2	28982	253
VV^2	9833	56
HV^2	11843	382
(HH-VV)×HV	18707	349
Yamaguchi helix	5044	141
Yamaguchi volume	5950	120
Yamaguchi surface	6012	21
Yamaguchi double	35521	748
Yamaguchi double rot.	39374	671

Table 3.3 Maximum intensity divided by mean sea intensity for Norne FPSO on December 10th 2009.

Figure 3.16 - Figure 3.19 show signatures of ships and ocean clutter in sub images of 600 pixels × 600 pixels on March 23rd 2010 for different polarisations and polarisation combinations. The incidence angle of the vessels is 43°. The oil platform Deepsea Bergen (93 m) is shown at the top left, Ocean Prince (65 m) in the middle and Norne FPSO (260 m) at the bottom right. The ship to sea contrast is enhanced in the *HV*-channel, the *LR* and *RL* images, in the double bounce case (*HH-VV*) and when combining the double bounce and volume scattering. Figure 3.19 shows the same vessels presented in Yamaguchi surface rotated, Yamaguchi helix rotated, Yamaguchi volume rotated and Yamaguchi double rotated.

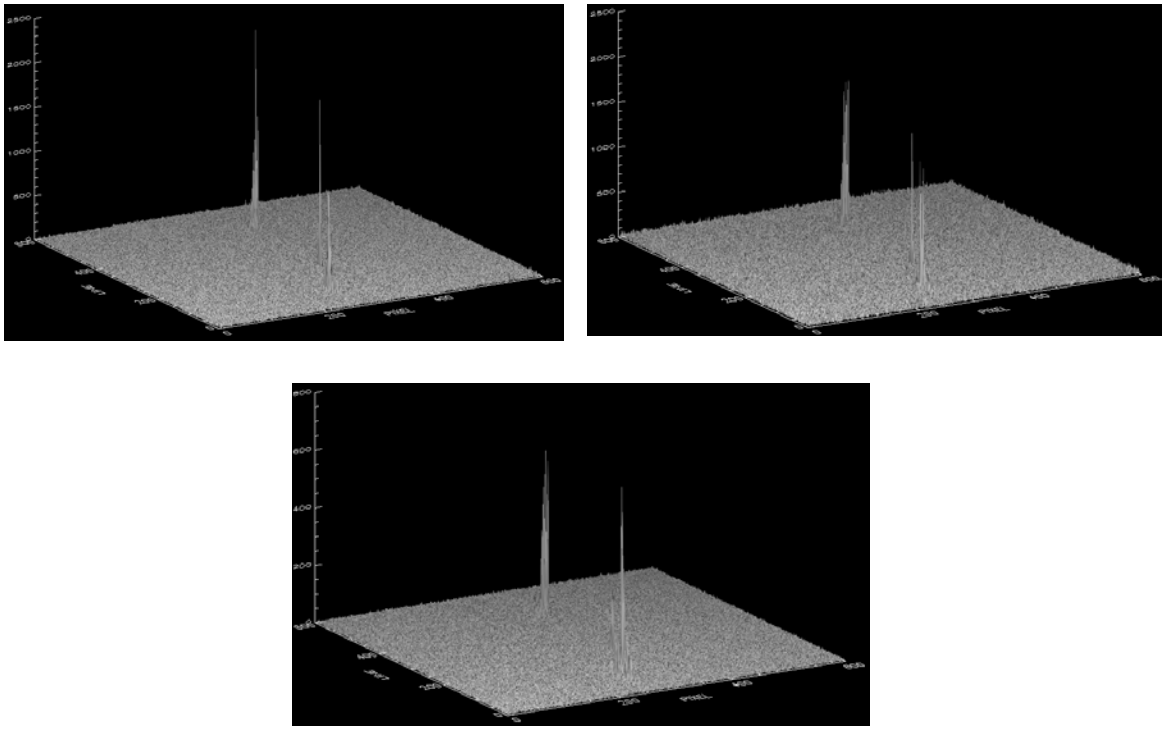

Figure 3.16 Sub sections of 600 pixels × 600 pixels in HH (top left), VV (top right) and HV (bottom) from March 23rd 2010. Norne FPSO is shown at the top.

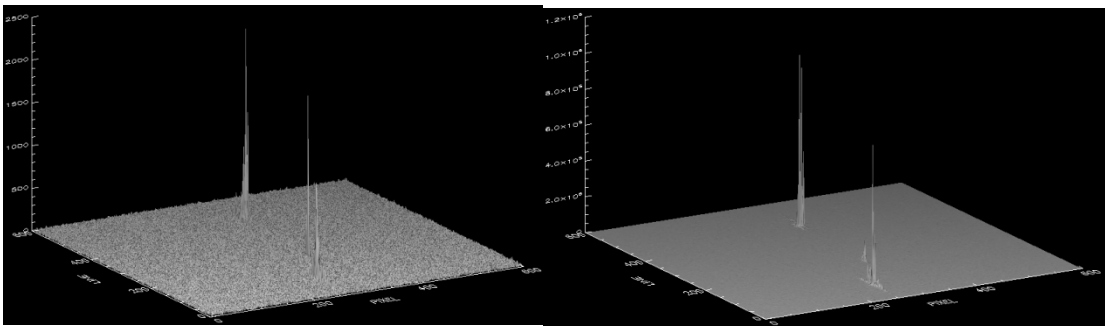

Figure 3.17 Three detections in HH (top) and (HH-VV)×HV (bottom) on March 23rd 2010. Norne FPSO is shown at the top.

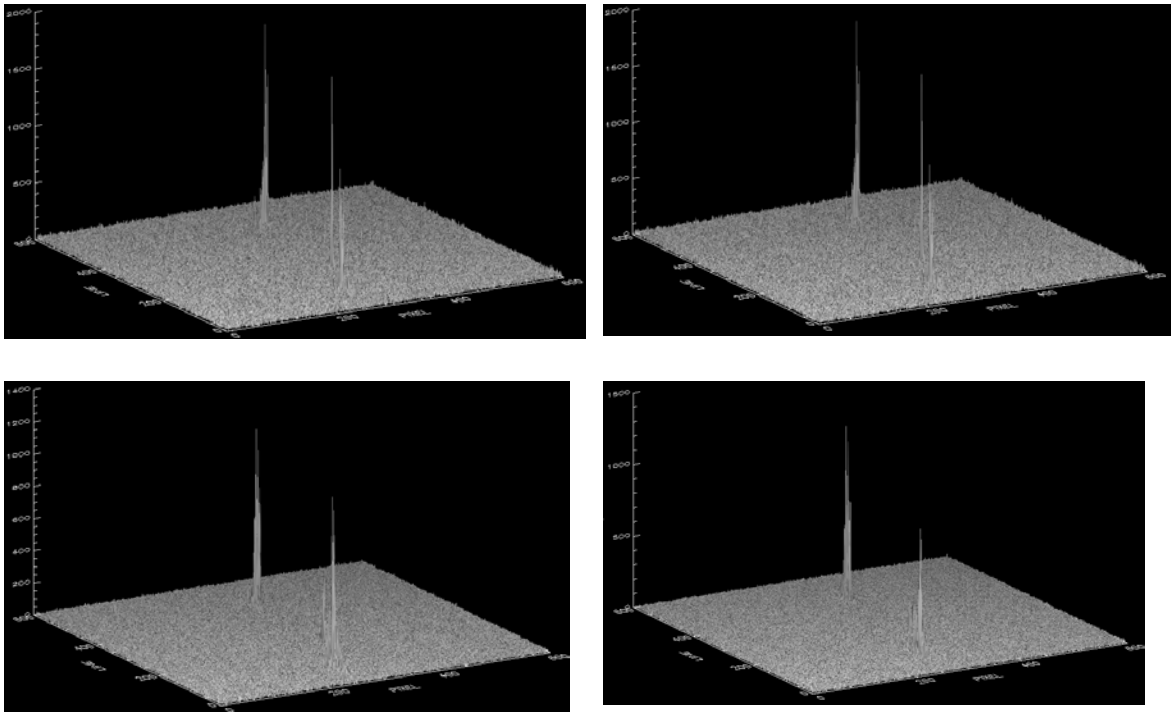

Figure 3.18 Sub sections of 600 pixels × 600 pixels in RR (top left), LL (top right), RL (bottom left), LR (bottom right) from March 23rd 2010. Norne FPSO is shown at the top.

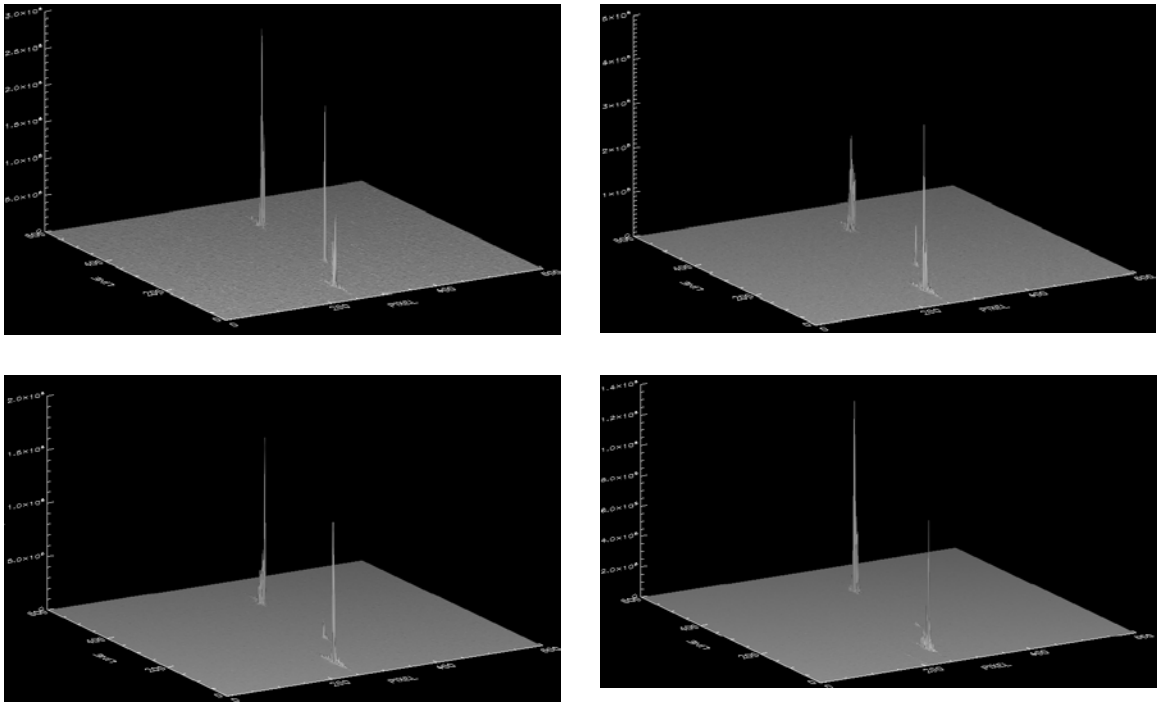

Figure 3.19 3D signatures of three vessels and the ocean background on March 23rd 2010 using Yamaguchi surface rotated (top), Yamaguchi helix rotated, Yamaguchi volume rotated and Yamaguchi double rotated (bottom). Norne FPSO is shown to the top.

Table 3.4 and Table 3.5 shows contrast measures of Norne FPSO and Ocean Prince for different polarisation channels and polarisation combinations. The numbers indicate what we have seen in Figure 3.16 - Figure 3.19.

	Max. amplitude / mean sea	
Method	**Norne FPSO**	**Ocean Prince**
HH	135	98
HV	122	58
HH-VV	139	30
RR	86	76
RL	117	46
kSphere	87	75
kHelix	140	74
Sqrt((HH-VV)×HV)	113	39
Sqrt(Yamaguchi helix)	71	47
Sqrt(Yamaguchi volume)	76	29
Sqrt(Yamaguchi surface)	47	38
Sqrt(Yamaguchi double)	151	16
Sqrt(Yamaguchi double rot.)	150	15

Table 3.4 Maximum amplitude divided by mean sea for Norne FPSO and Ocean prince on March 23rd 2010.

	Max. intensity / mean sea intensity	
Method	**Norne FPSO**	**Ocean Prince**
HH^2	13629	7312
VV^2	3835	2212
HV^2	11800	2665
(HH-VV)×HV	10628	1284
Yamaguchi helix	4091	1831
Yamaguchi volume	5455	822
Yamaguchi surface	2081	1355
Yamaguchi double	18728	191
Yamaguchi helix rot.	4091	1869
Yamaguchi volume rot.	12242	1216
Yamaguchi surface rot.	2057	1353
Yamaguchi double rot.	18326	189

Table 3.5 Maximum amplitude divided by mean sea for Norne FPSO and Ocean prince on March 23rd 2010.

Norne FPSO (260 m) is imaged in 23 quad-polarisation images. The relatively small vessels Ocean King (75 m), Ocean Prince (65 m) and Far Star (84 m) are imaged in 24 images in total. Edda Fauna (108 m) and Island Wellserver (116 m) (medium sized vessels) are imaged in seven images in total.

Figure 3.20 - Figure 3.22 show maximum amplitude divided by mean sea amplitude for Norne FPSO, while Figure 3.23 and Figure 3.24 show maximum intensity divided by mean sea intensity. Figure 3.25 - Figure 3.27 show maximum amplitude divided by mean sea amplitude for medium sized vessels, while Figure 3.28 shows maximum intensity divided by mean sea intensity. Figure 3.29 - Figure 3.31 show maximum amplitude divided by mean sea amplitude for small vessels, while Figure 3.32 and Figure 3.33 show maximum intensity divided by mean sea intensity.

Figure 3.20, Figure 3.25 and Figure 3.29 show that *VV*-polarisation gives the weakest contrast of the four polarisations for all vessel sizes and all incidence angles. Cross-polarisation is best, especially under 35°, but gives good results for all incidence angles. Over 35° the situation is more mixed, and HH-polarisation gives better results than it gives below 35°.

Figure 3.21, Figure 3.26 and Figure 3.30 show that *HH*-polarisation gives the lowest contrast of the four polarisations/polarisation combinations in the figures. *HH-VV* and *RL* seem to give better contrast than *HV*-polarisation for Norne FPSO (large vessel). For medium vessels, *HV*, *RL* and *HH-VV* are better than *HH* for all incidence angles. For small vessels, the contrasts give more mixed results for *HH-VV*, *RL* and *HV*, but are always better than *HH*. *HH*-polarisation performs better for higher incidence angles, especially over 37°.

Sqrt(Yamaguchi volume rotated), Sqrt(Yamaguchi double rotated) and Sqrt*((HH-VV)×HV)* are compared in Figure 3.22, Figure 3.27 and Figure 3.31 because the variables seem to give similar contrasts. For large vessels Figure 3.22 shows that for incidence angles below 27°, the contrasts are more similar, and it is hard to find out which one that gives the best contrasts. Yamaguchi double rotated and Yamaguchi volume rotated are slightly better for incidence angles between 27° and 30° and clearly better for incidence angles over 30°. Yamaguchi double rotated gives best results for incidence angles over 30°. For medium vessels Figure 3.27 shows that for incidence angles below 27°, the contrasts give more mixed results. For incidence angles over 27° Yamaguchi double rotated is best. Yamaguchi volume rotated and *(HH-VV)×HV* give more similar results, but the contrasts are below Yamaguchi double rotated. For small vessels Figure 3.31 shows that for incidence angles below 30°, the contrasts are more similar, and it is hard to find out which one that gives the best contrasts. For incidence angles over 30° Yamaguchi double rotated shows slightly the best contrasts. Yamaguchi volume rotated and *(HH-VV)×HV* give more mixed results, but the contrasts are below Yamaguchi double rotated.

Yamaguchi double rotated and *(HH-VV)×HV* give the best contrasts in Figure 3.23, Figure 3.28 and Figure 3.32 compared to Yamaguchi helix rotated and Yamaguchi volume rotated. *HV^2* gives the best contrast in Figure 3.24 (for large vessels), especially for small incidence angles.

HH^2 gives the lowest contrasts in Figure 3.24 for low incidence angles, which is expected. *HH^2*-polarisation performs better for higher incidence angles, especially over 40°.

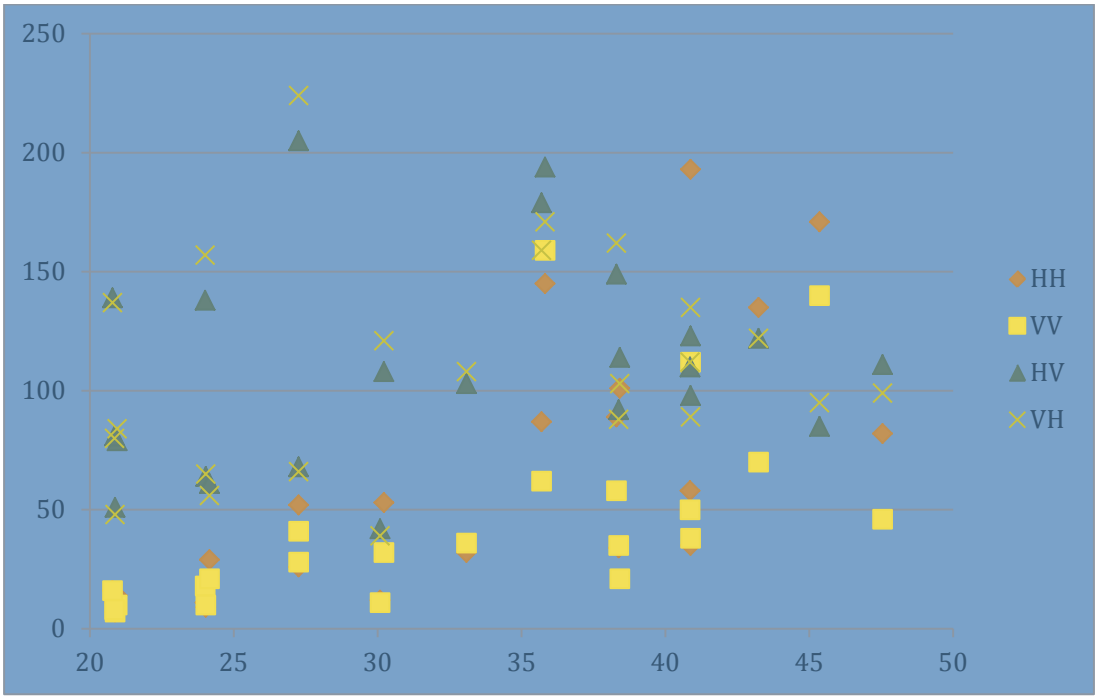

Figure 3.20 Maximum amplitude divided by mean sea amplitude for Norne FPSO for HH-polarisation, VV-polarisation, HV-polarisation and VH-polarisation.

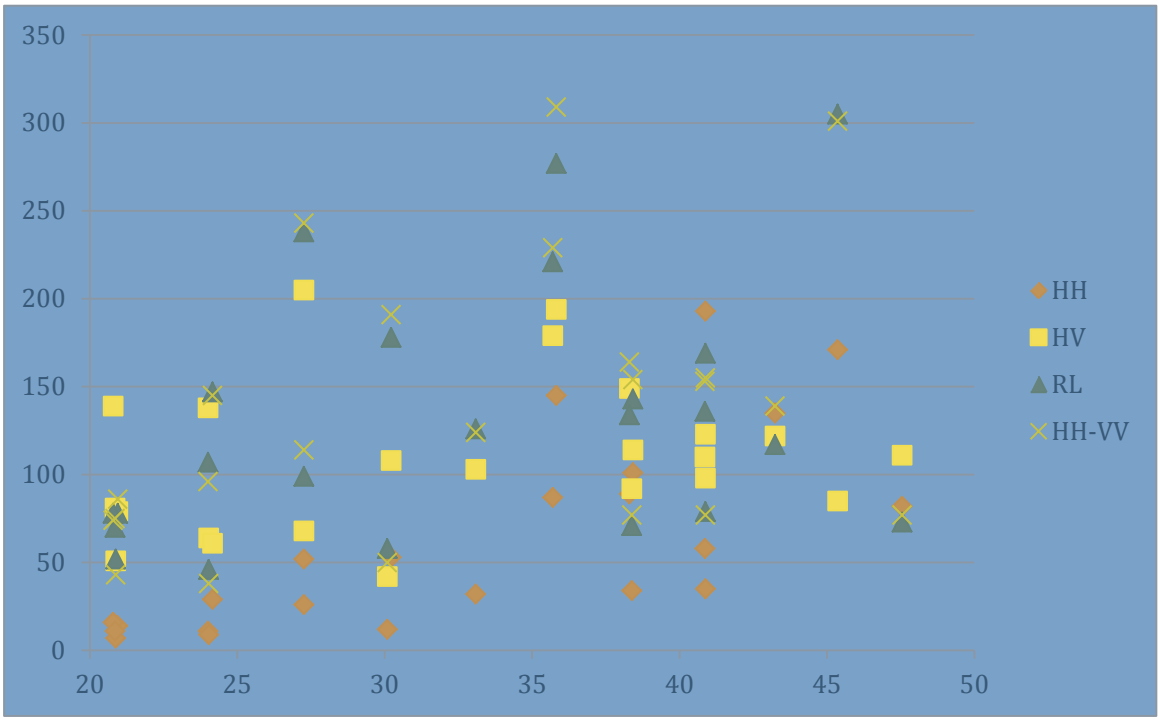

Figure 3.21 Maximum amplitude divided by mean sea amplitude for Norne FPSO for HH-polarisation, HV-polarisation, RL and (HH-VV).

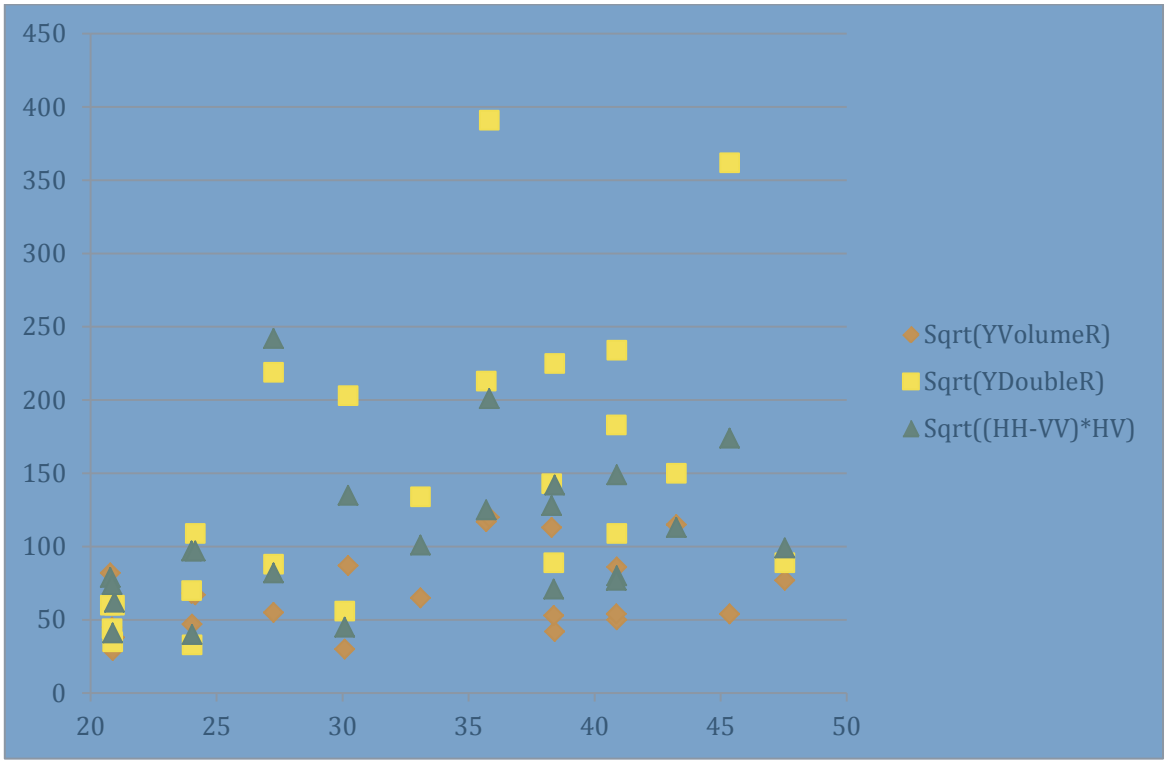

Figure 3.22 Maximum amplitude divided by mean sea amplitude for Norne FPSO for sqrt(Yamaguchi volume rotated), sqrt(Yamaguchi double rotated) and sqrt((HH-VV)×HV).

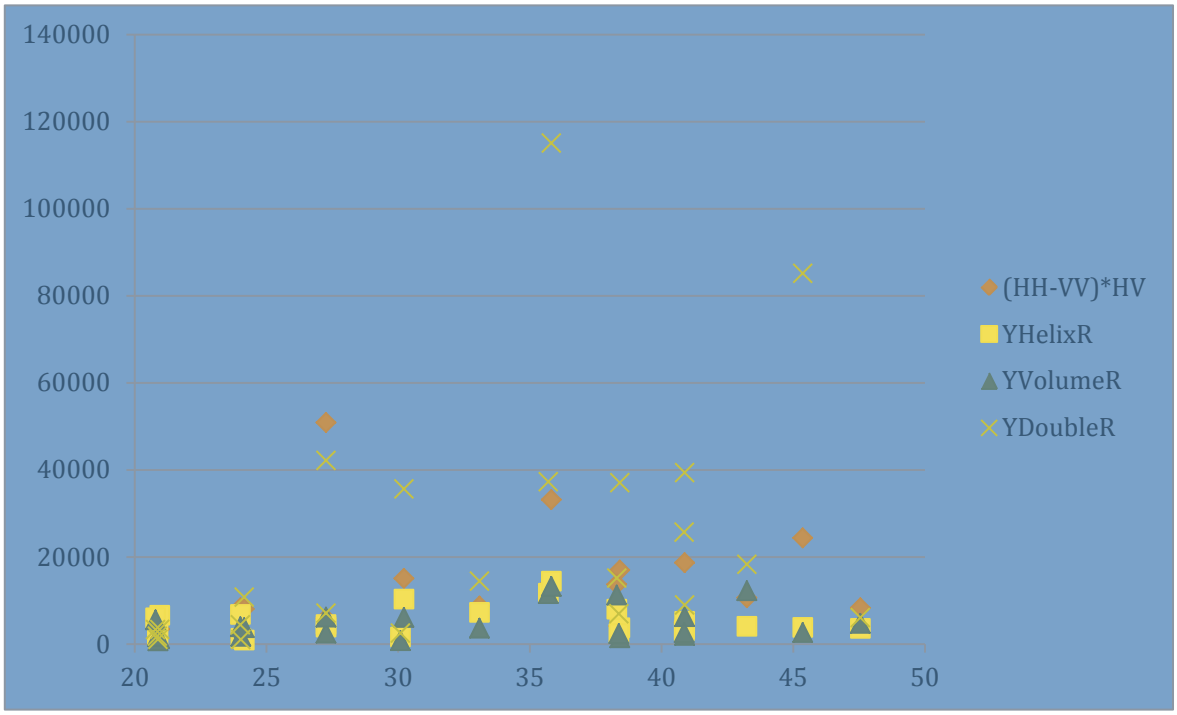

Figure 3.23 Maximum intensity divided by mean sea intensity for Norne FPSO for (HH-VV)×HV, Yamaguchi helix rotated, Yamaguchi volume rotated and Yamaguchi double rotated.

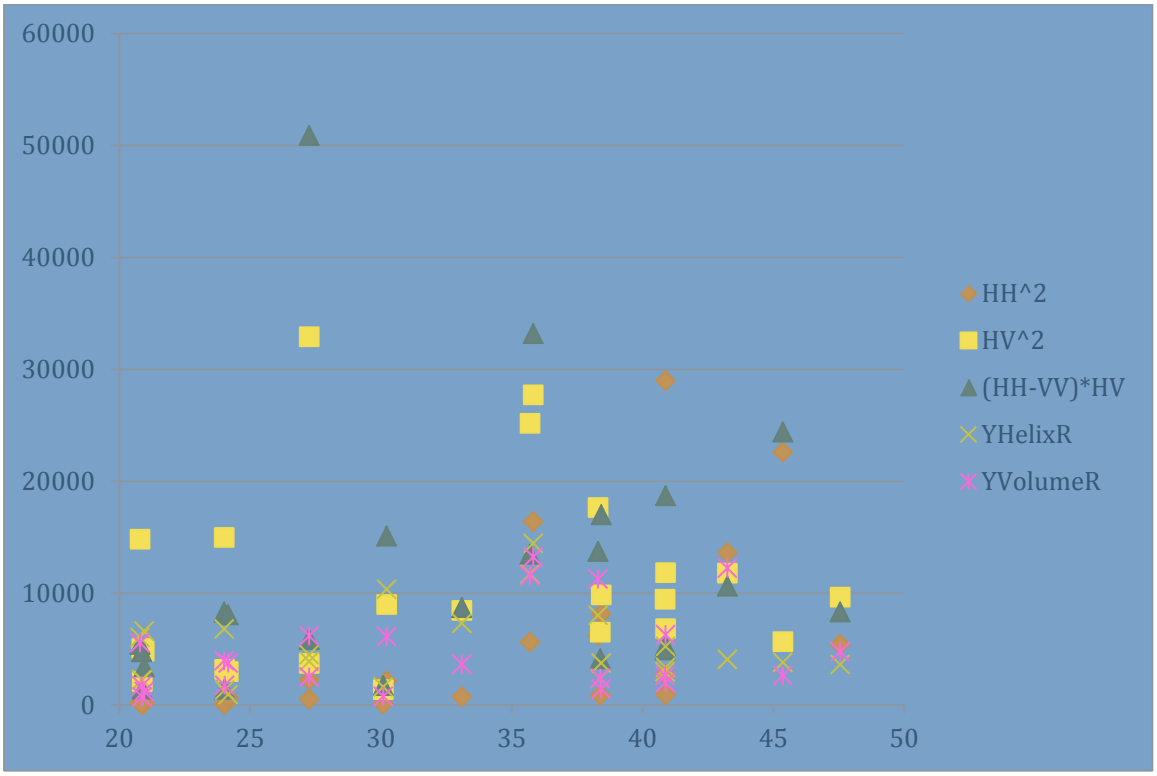

Figure 3.24 Maximum intensity divided by mean sea intensity for Norne FPSO for HH^2, HV^2, (HH-VV)×HV, Yamaguchi helix rotated and Yamaguchi volume rotated.

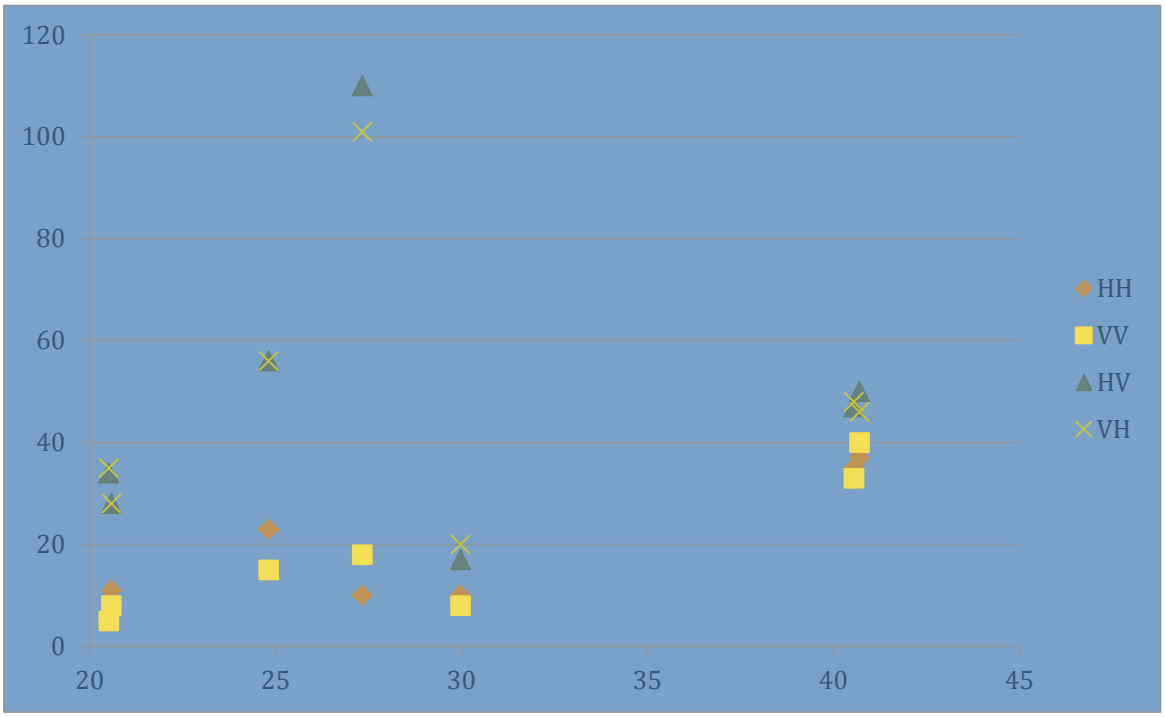

Figure 3.25 Maximum amplitude divided by mean sea amplitude for Edda Fauna, Vlas Nichkov and Island Wellserver for HH-polarisation, VV-polarisation, HV-polarisation and VH-polarisation.

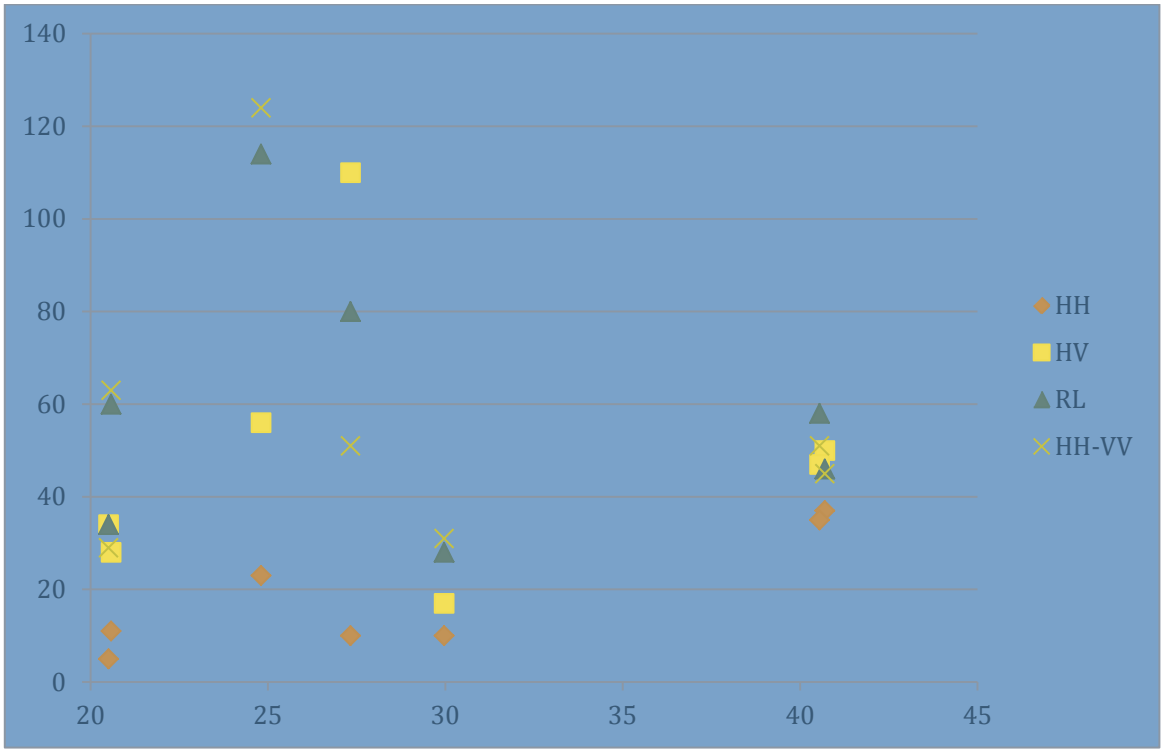

Figure 3.26 Maximum amplitude divided by mean sea amplitude for Edda Fauna, Vlas Nichkov and Island Wellserver for HH-polarisation, HV-polarisation, RL and HH-VV.

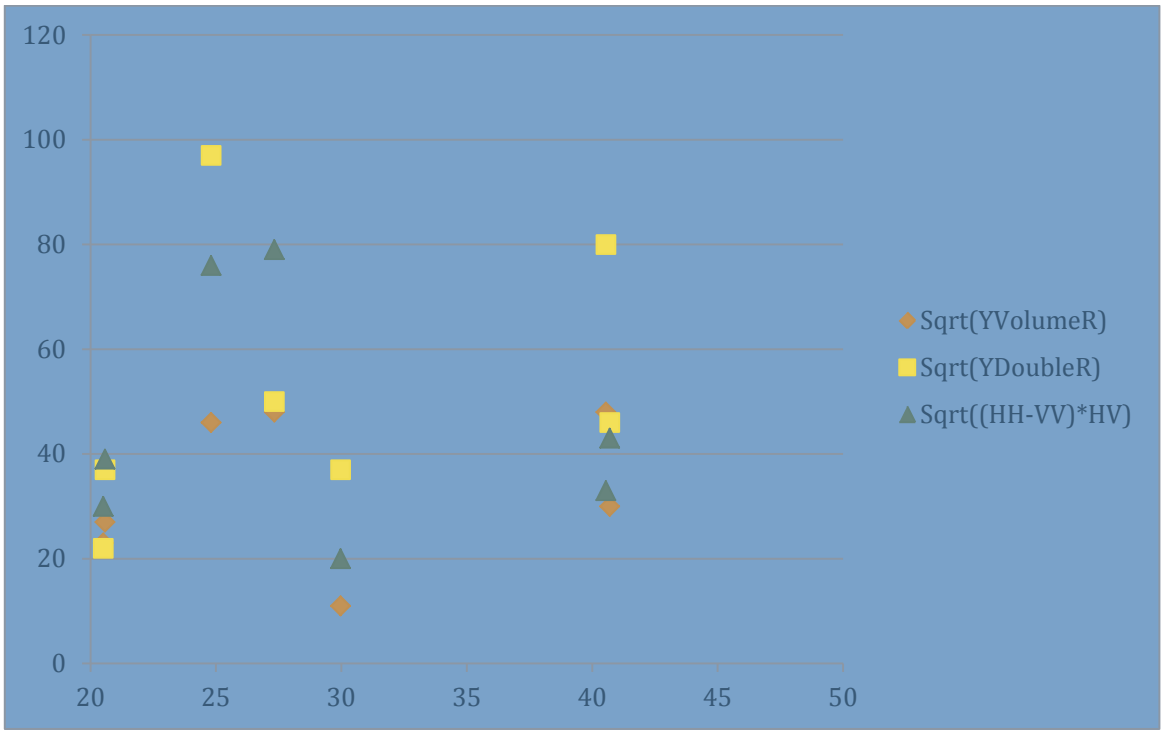

Figure 3.27 Maximum amplitude divided by mean sea amplitude for Edda Fauna, Vlas Nichkov and Island Wellserver for sqrt(Yamaguchi volume rotated), sqrt(Yamaguchi double rotated) and sqrt((HH-VV)×HV).

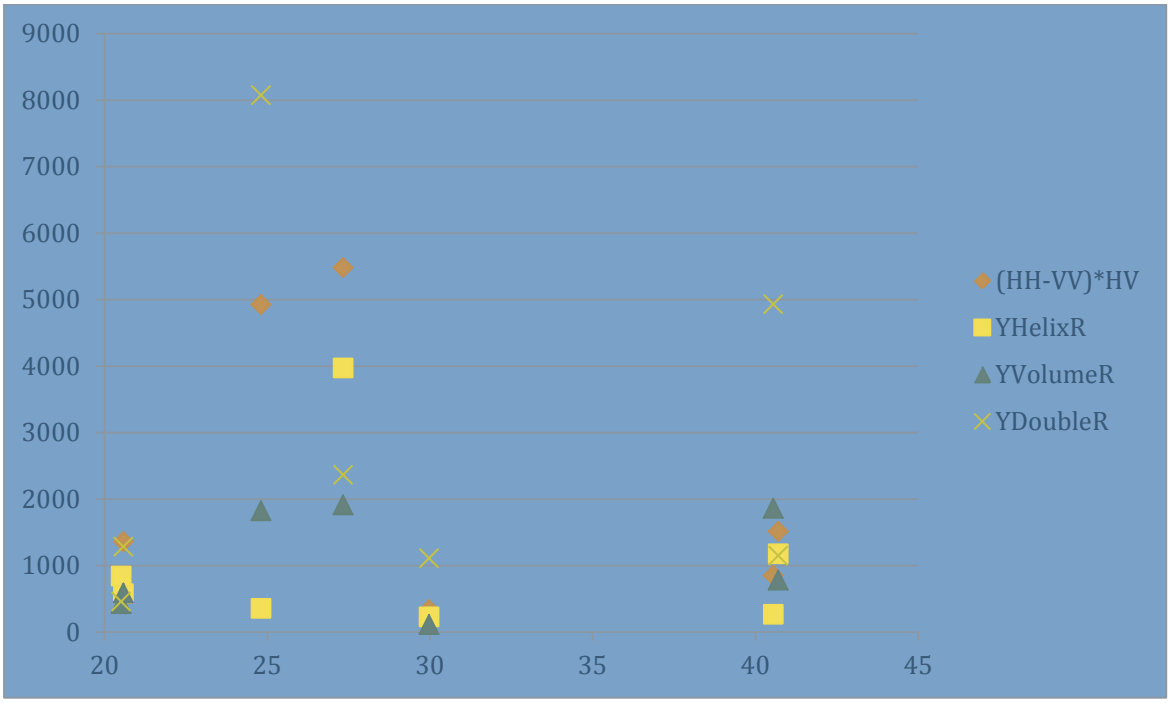

Figure 3.28 Maximum intensity divided by mean sea intensity for Edda Fauna, Vlas Nichkov and Island Wellserver for (HH-VV)×HV, Yamaguchi helix rotated, Yamaguchi volume rotated and Yamaguchi double rotated.

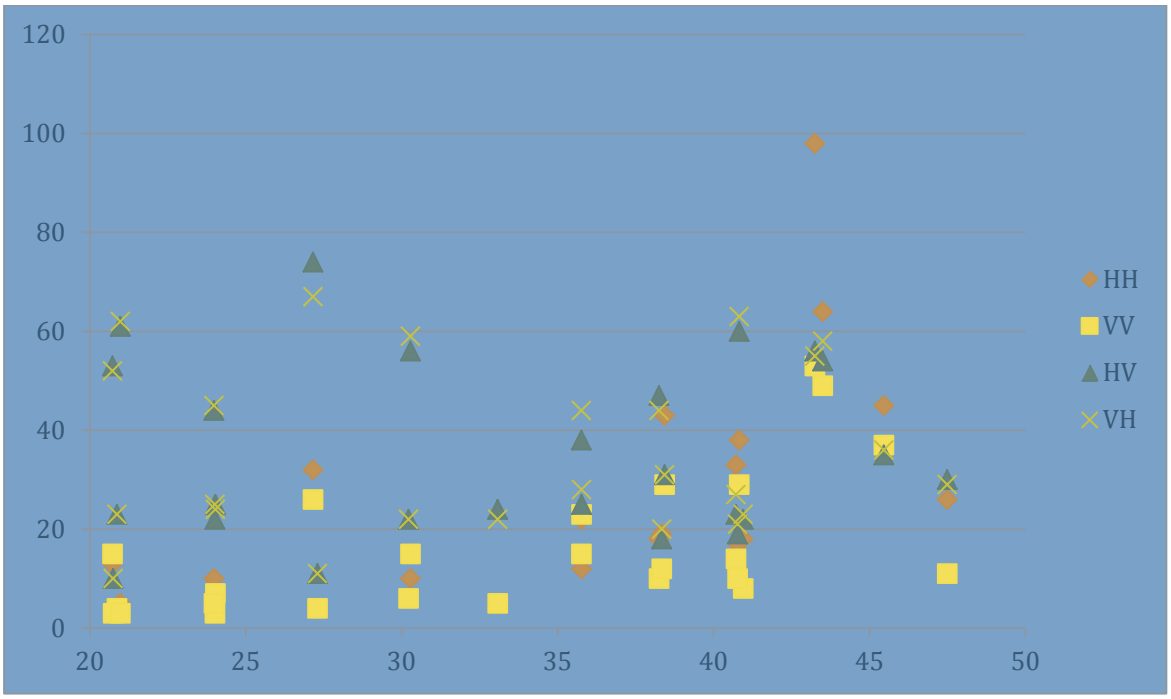

Figure 3.29 Maximum amplitude divided by mean sea amplitude for Ocean Prince and Ocean King for HH-polarisation, VV-polarisation, HV-polarisation and VH-polarisation.

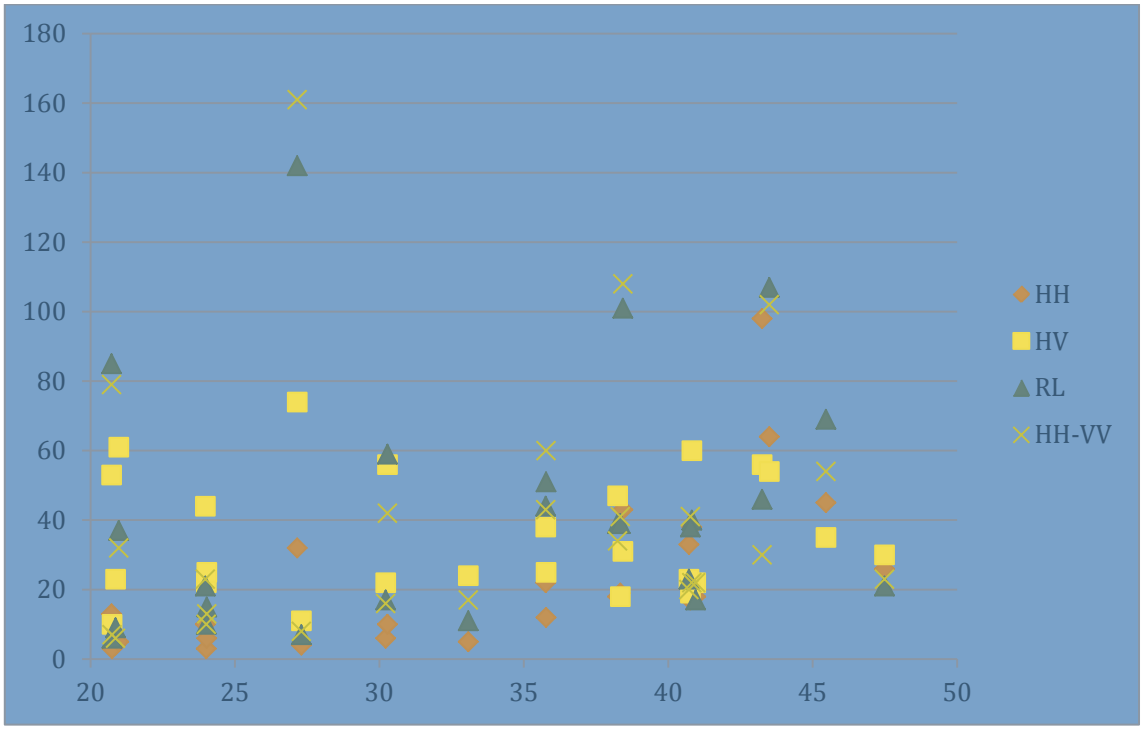

Figure 3.30 Maximum amplitude divided by mean sea amplitude for Ocean Prince and Ocean King for HH-polarisation, HV-polarisation, RL and HH-VV.

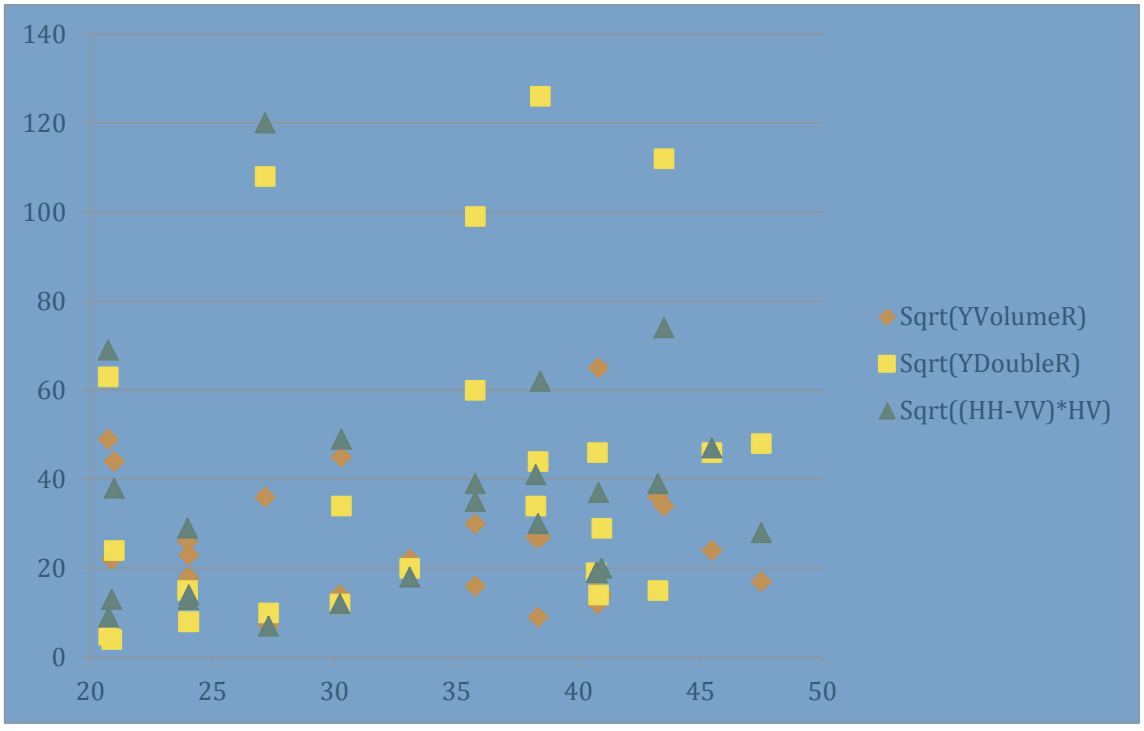

Figure 3.31 Maximum amplitude divided by mean sea amplitude for Ocean Prince and Ocean King for sqrt(Yamaguchi volume rotated), sqrt(Yamaguchi double rotated) and sqrt((HH-VV)×HV).

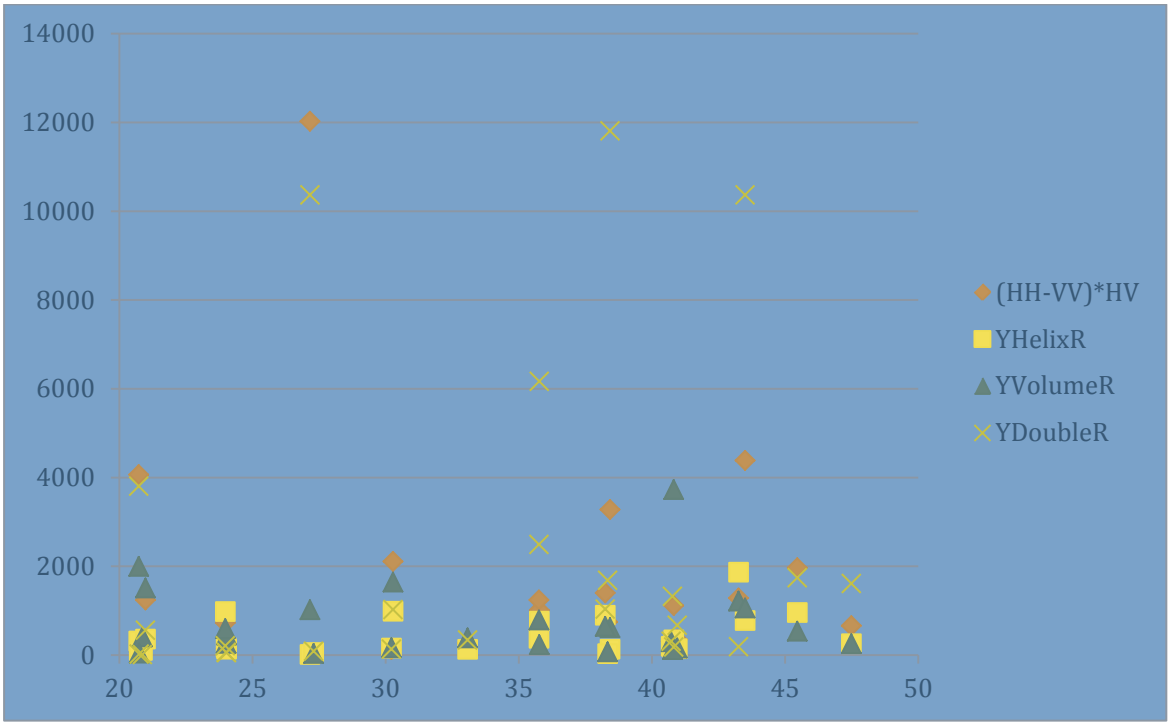

Figure 3.32 Maximum intensity divided by mean sea intensity for Ocean Prince and Ocean King for (HH-VV)×HV, Yamaguchi helix rotated, Yamaguchi volume rotated and Yamaguchi double rotated.

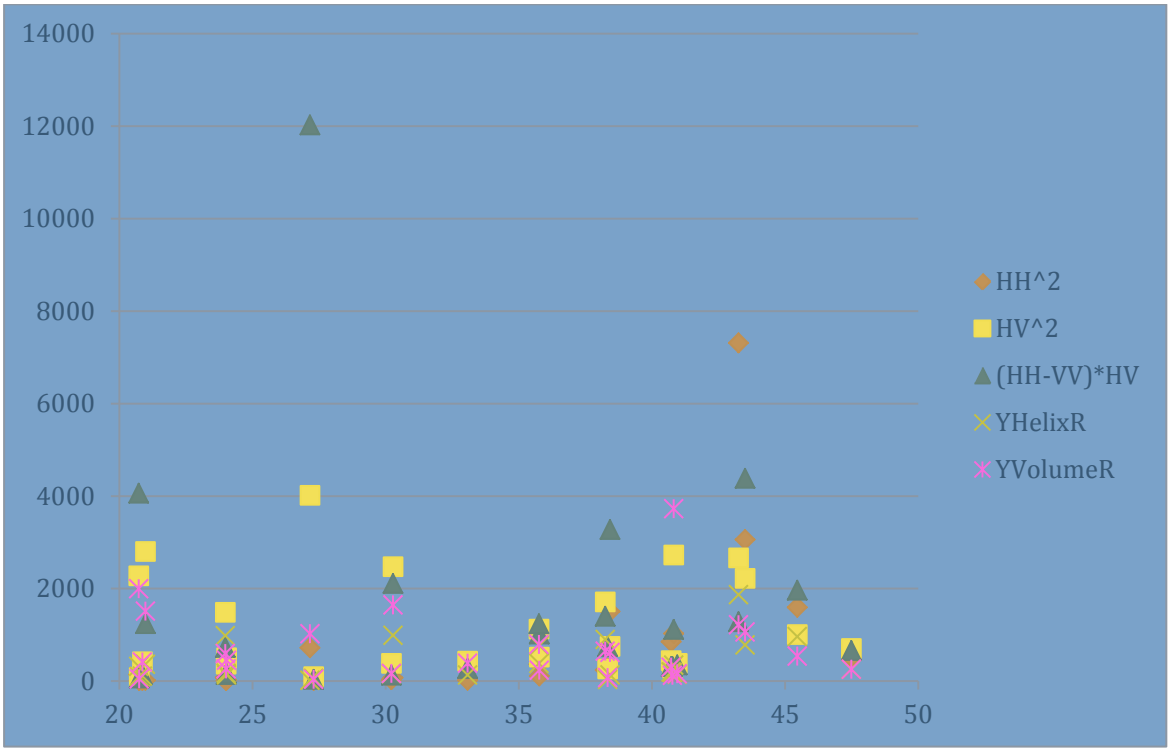

Figure 3.33 Maximum intensity divided by mean sea intensity for Ocean Prince and Ocean King for HH^2, HV^2, (HH-VV)×HV, Yamaguchi helix rotated and Yamaguchi volume rotated.

3.2 Automatic analysis

Table 3.6 shows the results from running the automatic analysis tool Aegir (see appendix B) on 19 quad-polarisation RADARSAT-2 images from November 2009 to March 2010. The table presents first the results from images with low, medium and large incidence angle (θ). *HH*- and *VV*-polarisation are shown in separate columns, while *HV*-, *VH*-polarisation and *(HH-VV)×HV* (combined case) are shown in the same column since the results from these are the same with respect to how many of the vessels that were detected. The last column shows how many vessels that are expected to be detected in each SAR image, based on AIS data from [14] and [15]. If two vessels are completely side by side, then only one detection is expected. The smallest AIS reported vessel is 65 m long and the longest is 264 m long. If all vessels are detected, the numbers are marked in light blue.

Date	θ	HH	VV	HV, VH & comb.	Exp. det.
29/11-09	L	4	5	6	6
9/12-09	L	0	0	5	5
15/12-09	L	0	0	5	5
22/12-09	L	2	2	3	3
21/3-10	L	0	0	4	4
22/3-10	L	0	0	7	7
29/3-10	L	6	6	6	6
28/3-12	L	1	1	4	4
1/12-09	M	3	0	7	7
17/3-10	M	5	5	6	6
19/3-10	M	4	4	5	5
10/12-09	H	6	5	5	6
21/12-09	H	0	0	0	0
16/3-10	H	5	6	6	6
20/3-10	H	5	5	5	5
23/3-10	H	5	5	5	5
26/3-10	H	3	1	4	4
22/3-12	H	4	4	4	4
29/3-12	H	5	4	5	5

Table 3.6 Results from automatic ship detection with Aegir on 19 quad-polarisation images. L = low, M = medium and H = high incidence angle.

The cross-polarisation channels and the fused case perform very well when using Aegir for automatic ship detection. All vessels are detected except in one image with high incidence angle on December 10th 2009 where there are strong surface waves in the SAR image. The co-polarisation channels miss one or more vessels in many images for all incidence angles. The co-polarisation channels perform better for higher incidence angles as expected, especially for *HH*-polarisation, but not as good as the performance of cross-polarisation and when combining the channels. The performance is poor for low and medium incidence angles for both of the co-polarisation channels.

3.2.1 Dual-polarisation and ice detection

The information content is not as good for dual-polarised data as it is for quad-polarised data, but some information is possible to get. Figure 3.34 shows RADARSAT-2 SAR ScanSAR Wide images on March 14th 2012 at 04:52:10 in the Baltic Sea. Land, ice and many vessels can be seen in the images. Figure 3.37 shows segments (area shown in white square in Figure 3.34) of the same images. It is easier to see the ice and vessels in the HV-polarisation image. Figure 3.35 shows the same segments in 3D view. The vessels have higher peaks than the ice. Silja Festival is 171 m long and Nordanhav is 127 m long, and are shown in Figure 3.36. Table 3.7 shows the maximum amplitude divided by mean sea for ice at 31.2 °, Silja Festival at 31.4° and Nordanhav at 30.5°. Both polarisation channels give values below 10 for both vessels and ice. Combining the polarisation channels gives evident improvements for the vessels.

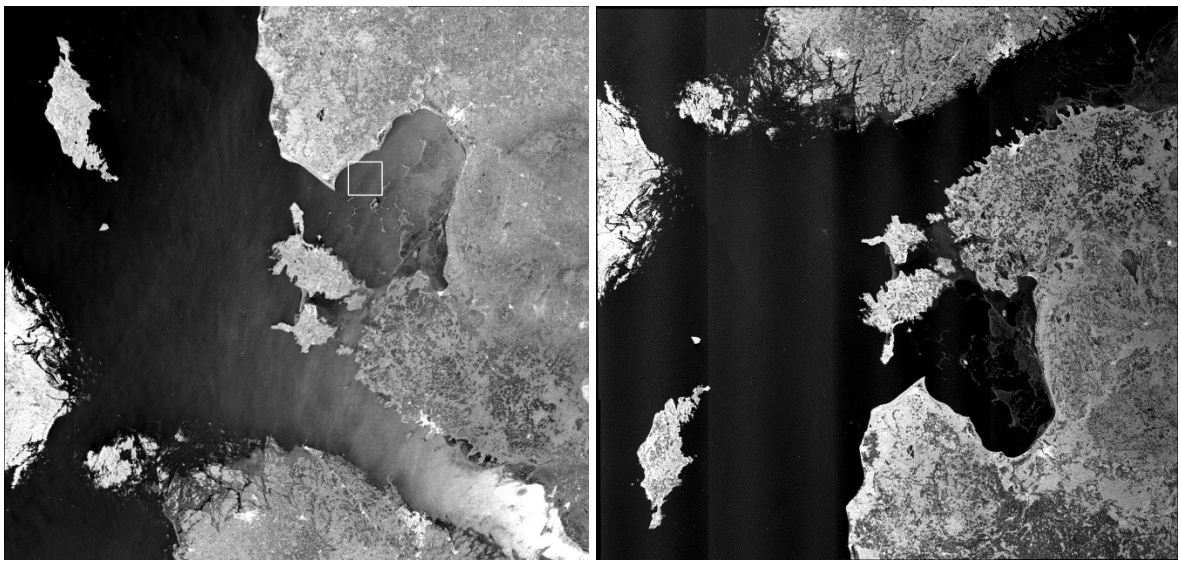

Figure 3.34 RADARSAT-2 HH-polarisation and HV-polarisation ScanSAR Wide images on March 14th 2012 at 04:52:10 in the Baltic Sea. Land, ice and vessels are shown in the images.

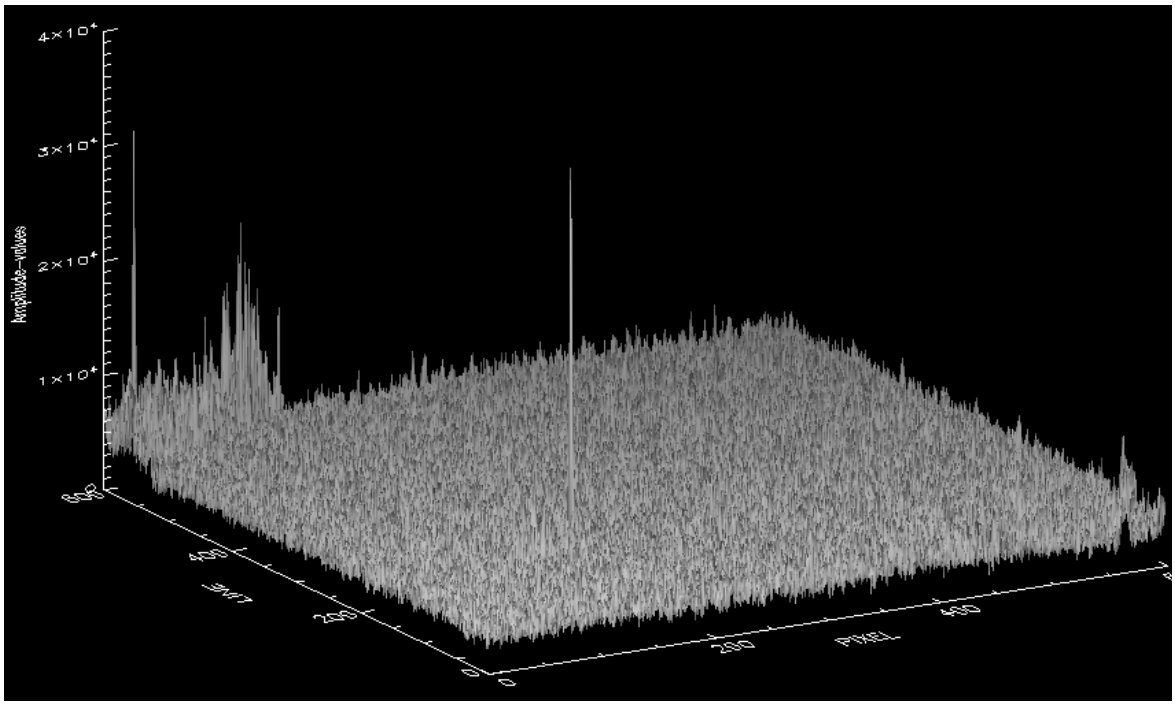
4×10⁴
3×10⁴
2×10⁴
1×10⁴
Amplitude-values
AZIMUTH
PIXEL

HH

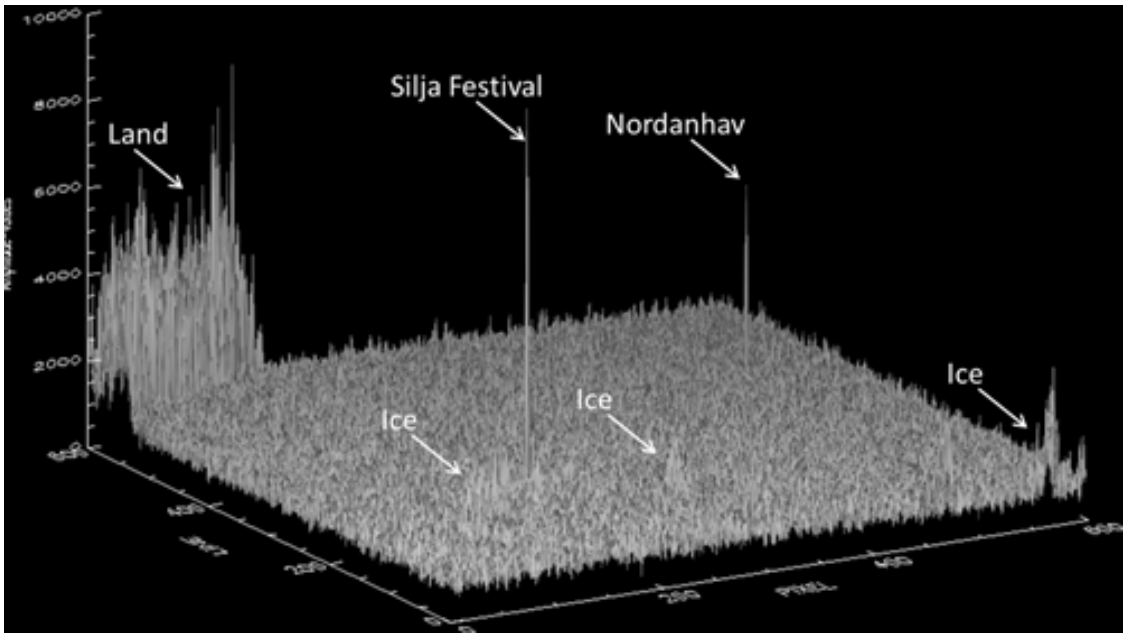
Land
Silja Festival
Nordanhav
Ice
Ice
Ice

HV

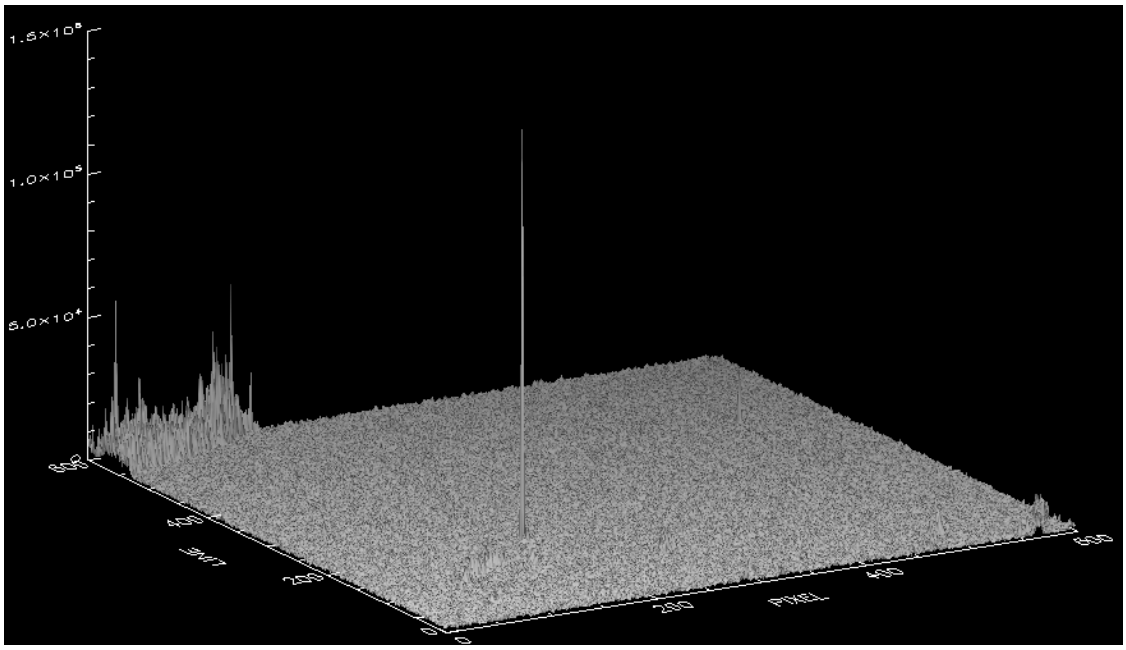

HHxHV

Figure 3.35 3D 600 pixels × 600 pixels segments of RADARSAT-2 images on March 14th 2012 at 04:52:10. Top previous page: HH-polarisation, bottom previous page: HV-polarisation and this page: HH×HV. The segments show land, ice and vessels.

Figure 3.36 Silja Festival (left) and Nordanhav (right). Source: marinetraffic.com.

	Max. amplitude / mean background		
Method	**Ice**	**Silja Festival**	**Nordanhav**
HH	2	9	2
HV	3	9	6
HH×HV	5	81	14

Table 3.7 Maximum amplitude divided by mean background for Silja Festival, Nordanhav and ice.

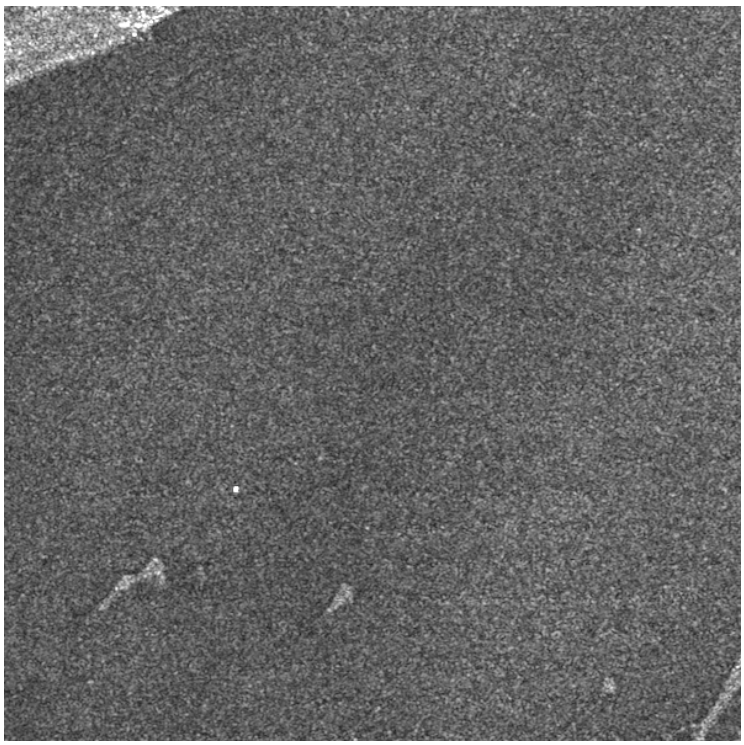

HH

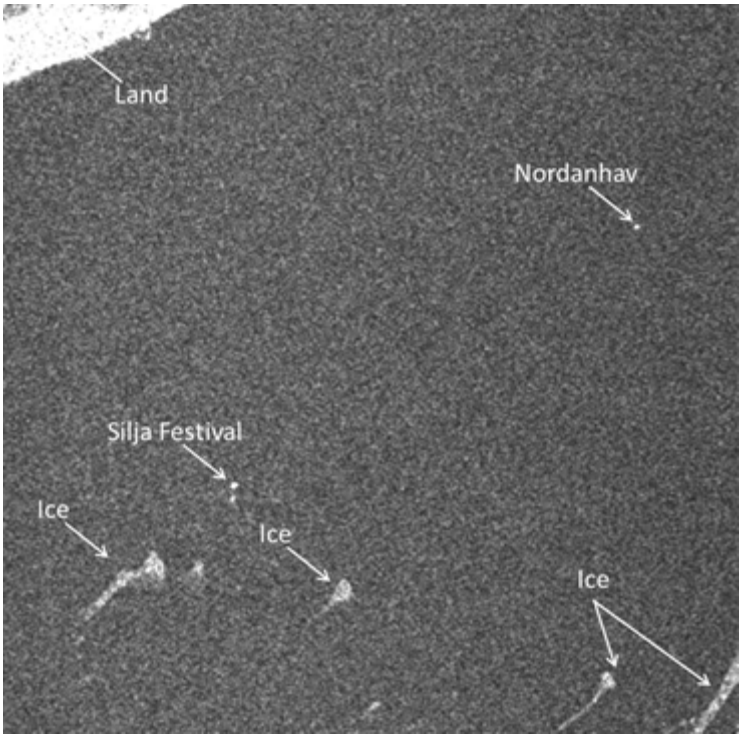

HV

Figure 3.37 Segments of RADARSAT-2 images on March 14th 2012 at 04:52:10. The segments show land, ice and vessels. Top: HH-polarisation and bottom: HV-polarisation.

3.2.2 Quad-polarisation and ice detection

The decomposition methods can be used to help to discriminate between ice and vessels. Figure 3.38 shows segments of a SAR image in *HH*- and *HV*-polarisation in the Oslofjord on February 7th 2010. Two vessels are shown, Hagland Bona (88 m) at 40.43° and Sunbeam (43 m) at 40.46°. There is ice in the background and an island (lower left) is also inside the segment. Figure 3.39 shows a 3D segment from the same SAR image where the ferry Color Viking (137 m) at 40.64° and ice are shown. Figure 3.40 shows another 3D presentation of the same segment in *HH*-polarisation, *(HH-VV)×HV*, Yamaguchi volume rotated and Yamaguchi double rotated. It is shown that the ice is most suppressed in *(HH-VV)×HV* and Yamaguchi double rotated.

Table 3.8 shows the maximum amplitude divided by mean background of Hagland Bona, Sunbeam and ice.

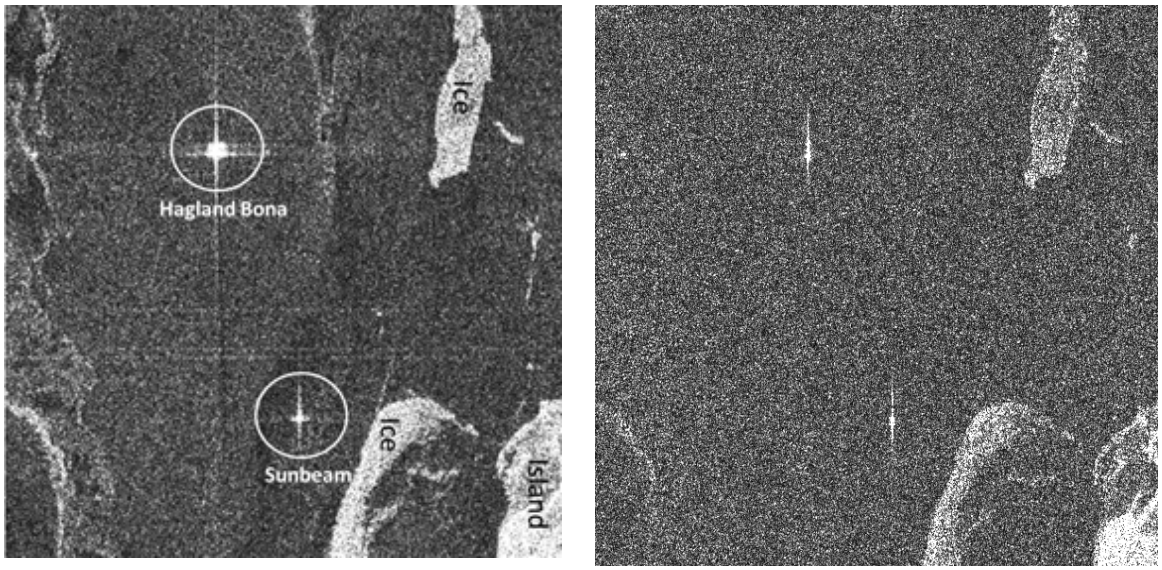

Figure 3.38 Sub images of RADARSAT-2 Standard quad-polarisation image on February 7th 2010 at 17:02:14. Left: HH. Right:HV.

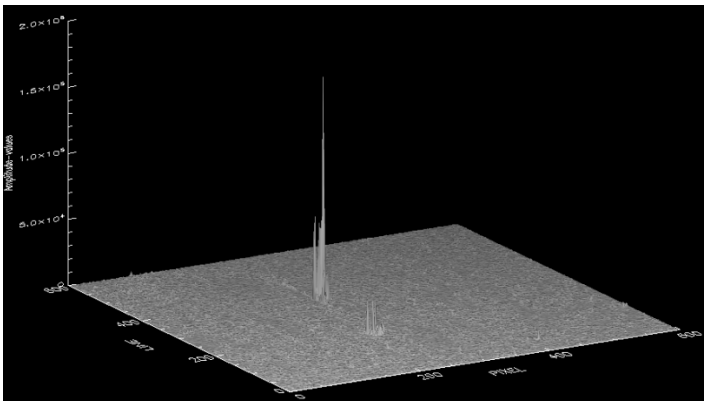

Figure 3.39 3D presentation of a segment of a SAR image on February 7th 2010 is shown in Yamaguchi volume rotated. Color Viking is shown at the top left and ice at the bottom right.

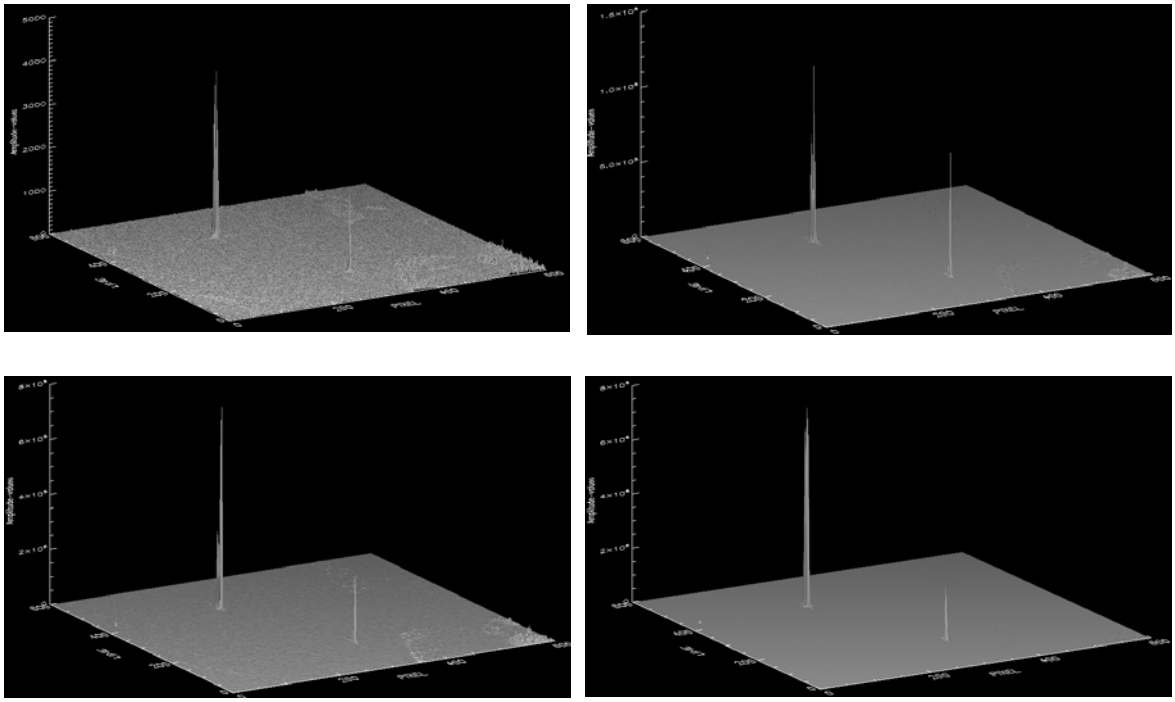

Figure 3.40 3D presentation of a 600 pixels × 600 pixels segment of a SAR image on February 7th 2010 are shown in HH-polarisation (top), (HH-VV)×HV, Yamaguchi volume rotated and Yamaguchi double rotated (bottom). The vessels Hagland Bona and Sunbeam are shown with high peaks.

	Max. amplitude / mean background		
Method	**Ice**	**Hagland Bona**	**Sunbeam**
HH	41	391	183
VV	18	290	130
HV	18	40	47
HH-VV	41	655	227
RR	18	133	67
RL	36	490	196
kSphere	19	139	77
kDiplane	39	692	216
kHelix	45	91	83
Sqrt((HH-VV)×HV)	24	158	112
Sqrt(Yamaguchi helix)	20	31	34
Sqrt(Yamaguchi volume)	6	57	25
Sqrt(Yamaguchi surface)	11	104	66
Sqrt(Yamaguchi double)	92	973	645
Sqrt(Yamaguchi helix rot.)	15	31	20
Sqrt(Yamaguchi volume rot.)	7	56	29
Sqrt(Yamaguchi surface rot.)	11	116	83
Sqrt(Yamaguchi double rot.)	78	985	581

Table 3.8 Maximum amplitude divided by mean background for ice and the vessels Hagland Bona and Sunbeam.

Table 3.9 shows maximum intensity divided by mean sea intensity. Table 3.10 shows the maximum amplitude divided by mean background of Color Viking and ice, while Table 3.11 shows maximum intensity divided by mean sea intensity.

	Max. intensity / mean background		
Method	**Ice**	**Hagland Bona**	**Sunbeam**
HH^2	1278	118160	26699
VV^2	251	67825	12907
VH^2	263	1036	1604
(HH-VV)×HV	481	21620	10786
Yamaguchi helix	328	768	951
Yamaguchi volume	33	3180	598
Yamaguchi surface	89	9663	2048
Yamaguchi double	3955	408884	103992
Yamaguchi helix rot.	186	768	320
Yamaguchi volume rot.	47	3039	809
Yamaguchi surface rot.	87	10867	2930
Yamaguchi double rot.	3229	392433	84792

Table 3.9 Maximum intensity divided by mean background intensity for ice and the vessels Hagland Bona and Sunbeam

	Max. amplitude / mean background	
Method	**Ice**	**Color Viking**
HH	69	143
VV	36	139
HV	19	88
HH-VV	109	226
RR	17	127
RL	85	185
kSphere	17	127
kDiplane	108	217
kHelix	28	73
Sqrt((HH-VV)×HV)	36	141
Sqrt(Yamaguchi helix)	22	80
Sqrt(Yamaguchi volume)	11	39
Sqrt(Yamaguchi surface)	11	80
Sqrt(Yamaguchi double)	161	416
Sqrt(Yamaguchi helix rot.)	21	76
Sqrt(Yamaguchi volume rot.)	11	26
Sqrt(Yamaguchi surface rot.)	12	89
Sqrt(Yamaguchi double rot.)	128	398

Table 3.10 Maximum amplitude divided by mean background of Color Viking and ice.

	Max. intensity / mean background intensity	
Method	**Ice**	**Color Viking**
HH^2	3604	15765
VV^2	948	14465
VH^2	300	5449
(HH-VV)×HV	1148	16296
Yamaguchi helix	393	5326
Yamaguchi volume	105	1362
Yamaguchi surface	94	5246
Yamaguchi double	12448	80739
Yamaguchi helix rot.	372	4837
Yamaguchi volume rot.	108	609
Yamaguchi surface rot.	97	6072
Yamaguchi double rot.	7694	70546

Table 3.11 Maximum intensity divided by mean background intensity of Color Viking and ice.

Table 3.12 - Table 3.15 show ship-to-background measures where standard deviation or the variance of the background is included. This will better emphasize the polarimetric combinations and decompositions. The difference between the target and mean background are compared with the variations in the background. Then the ratio will have a high value if the background is suppressed and if the standard deviation (variation) in the background is reduced.

	Max. amplitude / (mean sea ×standard dev. of background)		
Method	**Ice**	**Hagland Bona**	**Sunbeam**
HH	2.8	35.1	17.6
VV	1.0	20.7	9.3
HV	2.4	6.9	6.6
HH-VV	2.5	52.3	17.5
RR	1.2	11.6	5.7
RL	4.7	63.2	22.5
kSphere	1.4	13.2	7.2
kDiplane	4.6	108.8	32.6
kHelix	5.7	12.8	10.8
Sqrt((HH-VV)×HV)	3.1	27.6	16.7
Sqrt(Yamaguchi helix)	3.0	6.3	6.5
Sqrt(Yamaguchi volume)	0.7	10.5	3.8
Sqrt(Yamaguchi surface)	0.7	11.0	4.9
Sqrt(Yamaguchi double)	11.5	151.1	84.4
Sqrt(Yamaguchi helix rot.)	2.2	6.3	3.8
Sqrt(Yamaguchi volume rot.)	0.7	8.3	3.8
Sqrt(Yamaguchi surface rot.)	0.6	9.9	6.4
Sqrt(Yamaguchi double rot.)	9.4	146.4	68.2

Table 3.12 Maximum amplitude divided by mean background and standard deviation of background for ice and the vessels Hagland Bona and Sunbeam.

The ship-to-background measures in Table 3.12 andTable 3.14 are the maximum amplitude divided by the mean background and the standard deviation of the background. Table 3.13 and Table 3.15 show the maximum intensity divided by the mean background intensity and the standard deviation of the background intensity.

	Max. intensity / (mean sea int. × standard dev. of background int.)		
Method	**Ice**	**Hagland Bona**	**Sunbeam**
HH^2	2.7	398.9	104.7
VV^2	0.3	150.9	28.8
VH^2	2.0	9.9	15.0
(HH-VV)×HV	2.6	245.3	79.8
Yamaguchi helix	2.6	13.6	14.8
Yamaguchi volume	0.1	18.1	2.6
Yamaguchi surface	0.1	43.3	8.9
Yamaguchi double	44.5	6185.8	1048.1
Yamaguchi helix rot.	1.5	13.6	5.0
Yamaguchi volume rot.	0.1	14.1	3.0
Yamaguchi surface rot.	0.1	42.4	12.8
Yamaguchi double rot.	34.3	5731.7	721.1

Table 3.13 Maximum intensity divided by mean background intensity and standard deviation of background intensity for ice and the vessels Hagland Bona and Sunbeam

	Max. amplitude / (mean sea × standard dev. of background)	
Method	**Ice**	**Color Viking**
HH	4.6	9.9
VV	1.6	6.8
HV	2.8	11.7
HH-VV	7.9	16.6
RR	0.9	7.8
RL	8.9	21.4
kSphere	0.9	7.8
kDiplane	15.2	28.9
kHelix	3.4	10.0
Sqrt((HH-VV)×HV)	5.1	19.9
Sqrt(Yamaguchi helix)	3.7	16.8
Sqrt(Yamaguchi volume)	1.1	3.7
Sqrt(Yamaguchi surface)	0.5	4.5
Sqrt(Yamaguchi double)	24.0	57.1
Sqrt(Yamaguchi helix rot.)	3.6	16.0
Sqrt(Yamaguchi volume rot.)	0.9	2.2
Sqrt(Yamaguchi surface rot.)	0.5	4.5
Sqrt(Yamaguchi double rot.)	15.3	49.6

Table 3.14 Maximum amplitude divided by mean background and standard deviation of background for Color Viking and ice.

	Max. intensity / (mean sea int. × standard dev. of background int.)	
Method	**Ice**	**Color Viking**
HH^2	7.2	32.2
VV^2	0.8	14.3
VH^2	2.9	45.3
(HH-VV)×HV	8.0	138.4
Yamaguchi helix	5.0	96.4
Yamaguchi volume	0.3	3.6
Yamaguchi surface	0.1	8.2
Yamaguchi double	227.8	1150.7
Yamaguchi helix rot.	4.7	87.6
Yamaguchi volume rot.	0.3	1.4
Yamaguchi surface rot.	0.1	9.0
Yamaguchi double rot.	91.9	904.2

Table 3.15 Maximum intensity divided by mean background intensity and standard deviation of background intensity for Color Viking and ice.

It may be possible to discriminate ice and vessels by looking at the values in the tables and using known information from the polarisation channels and the polarisation combinations. Yamaguchi surface values (both with rotation and without rotation) are higher than Yamaguchi volume values (both with rotation and without rotation) or approximately the same for ice. The values for Yamaguchi double rotated are 11 and 12 times larger than Yamaguchi volume rotated for ice, while the values are 18, 20 and 15 for the vessels. Ice has the lowest values for these four variables: sqrt(Yamaguchi volume), sqrt(Yamaguchi surface), sqrt(Yamaguchi volume rotated) and sqrt(Yamaguchi volume rotated). This is not the case for the vessels.

Table 3.16 and Table 3.17 show ratios calculated using Yamaguchi decomposition results. For all three vessels the ratios Yamaguchi double divided by Yamaguchi helix and Yamaguchi double divided by Yamaguchi volume have higher or equal values than the ratio Yamaguchi double divided by Yamaguchi surface. For ice the lowest ratio is Yamaguchi double divided by Yamaguchi helix. This is the case both with and without rotation.

Some of this information can be used to see the difference between ice and vessels.

Method	Ice	Hagland Bona	Sunbeam
Yd/Ys	44	42	51
Yd/Yv	120	129	174
Yd/Yh	12	532	109
Ydr/Ysr	37	36	29
Ydr/Yvr	69	129	105
Ydr/Yhr	17	511	265

Table 3.16 Ratios based on maximum amplitude divided by mean background calculated using Yamaguchi decomposition results for ice, Hagland Bona and Sunbeam.

Method	Ice	Color Viking
Yd/Ys	134	15
Yd/Yv	119	59
Yd/Yh	32	15
Ydr/Ysr	79	12
Ydr/Yvr	71	116
Ydr/Yhr	21	15

Table 3.17 Ratios based on maximum amplitude divided by mean background calculated using Yamaguchi decomposition results for ice and Color Viking.

Figure 3.41 shows a RADARSAT-2 Fine quad-pol HH-polarisation image on April 13th 2011 at 14:46:10. A segment of the image is shown in HH-polarisation, Pauli, Krogager and Yamaguchi. The image is from north of Spitsbergen, and shows ice and the Coast Guard vessel KV Svalbard in the middle of the ice at 32.7°. KV Svalbard is 103.5 m long and 19 m wide. Figure 3.42 shows the same image using the Pauli, Krogager, Yamaguchi and Yamaguchi rotated decomposition methods. The decomposition methods give different information about the vessel and the background ice.

Figure 3.43 shows a 60 pixels × 60 pixels segment of the image around KV Svalbard in *HH*-, *VV*, *HV*- and *VH*-polarisation. The maximum ship to sea contrast is slightly better for cross-polarisation than co-polarisation. Figure 3.44 - Figure 3.49 show bigger segment of 600 pixels × 600 pixels where KV Svalbard is inside the segment. Figure 3.44 shows *HH*-, *VV*-, *HV*- and *VH*-polarisation. KV Svalbard is marked with the arrow. More information about the ice in the background can be seen in cross-polarisation compared with co-polarisation. Figure 3.45 shows the circular decompositions *RR*, *LL*, *RL* and *LR*. More information about the ice in the background can be seen in *RL* and *LR* compared to *RR* and *LL*. Figure 3.46 shows the Krogager decompositions Krogager kDiplane, Krogager kSphere and Krogager kHelix. Figure 3.47 and Figure 3.48 show the Yamaguchi decompositions. Figure 3.47 shows Yamaguchi surface, Yamaguchi helix, Yamaguchi double and Yamaguchi volume, while Figure 3.48 shows Yamaguchi surface rotated, Yamaguchi helix rotated, Yamaguchi double rotated and Yamaguchi volume rotated. The vessel is very clear using Yamaguchi decomposition method. Yamaguchi double and Yamaguchi double rotated give more information about the ice in the background. Figure 3.49 shows *HH-VV* (double bounce) and *(HH-VV)×HV* ("double bounce times volume scattering"). The vessel KV Svalbard is very clear in the "double bounce times volume scattering", and the ice around the vessel is suppressed.

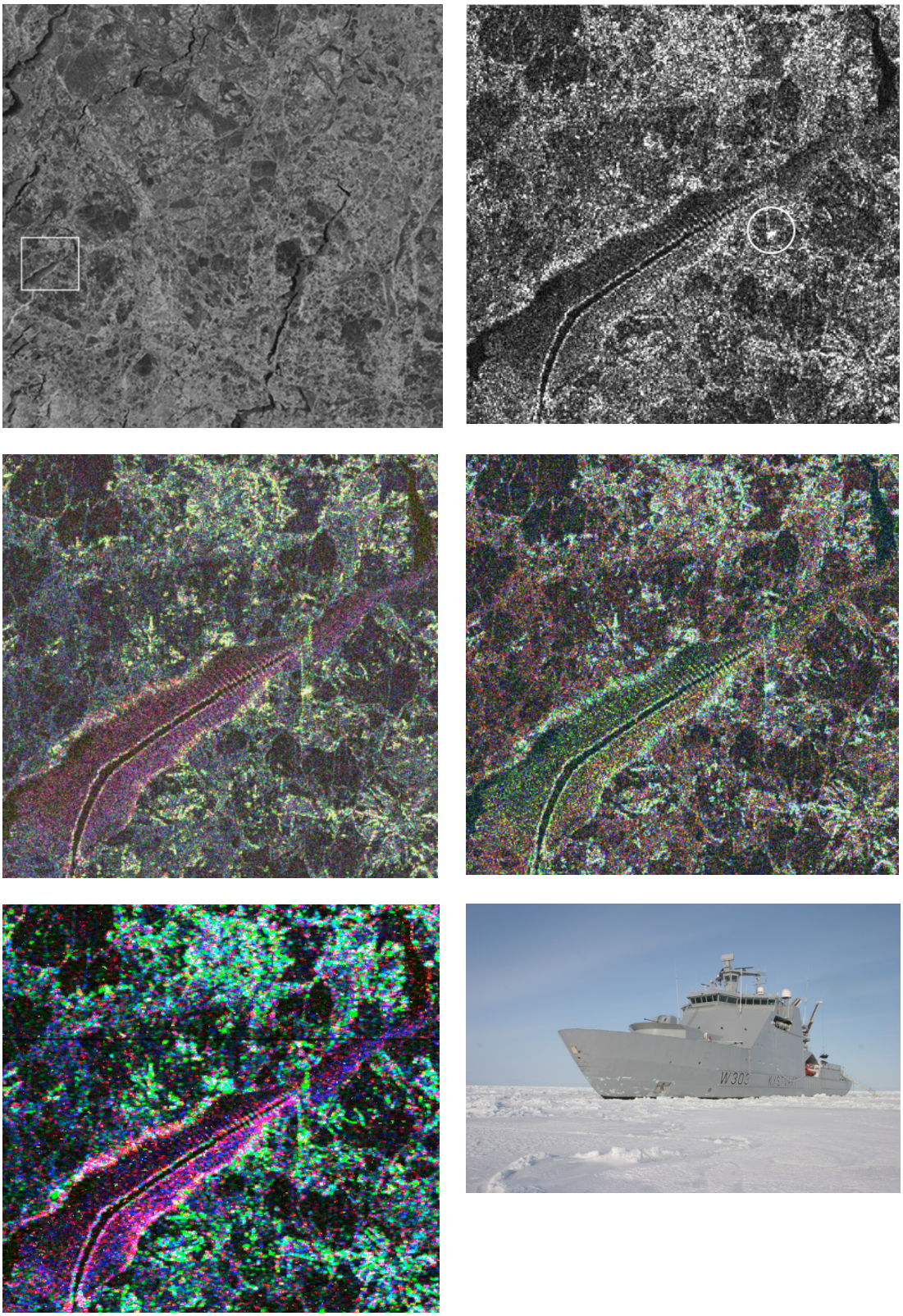

Figure 3.41 RADARSAT Fine quad-pol HH-polarisation image (top left) on April 13th at 14:46:10. A segment of the image with KV Svalbard inside the circle is shown in HH-polarisation (top right), Pauli (middle left), Krogager (middle right), Yamaguchi (bottom left). A picture of KV Svalbard is shown at the bottom right.

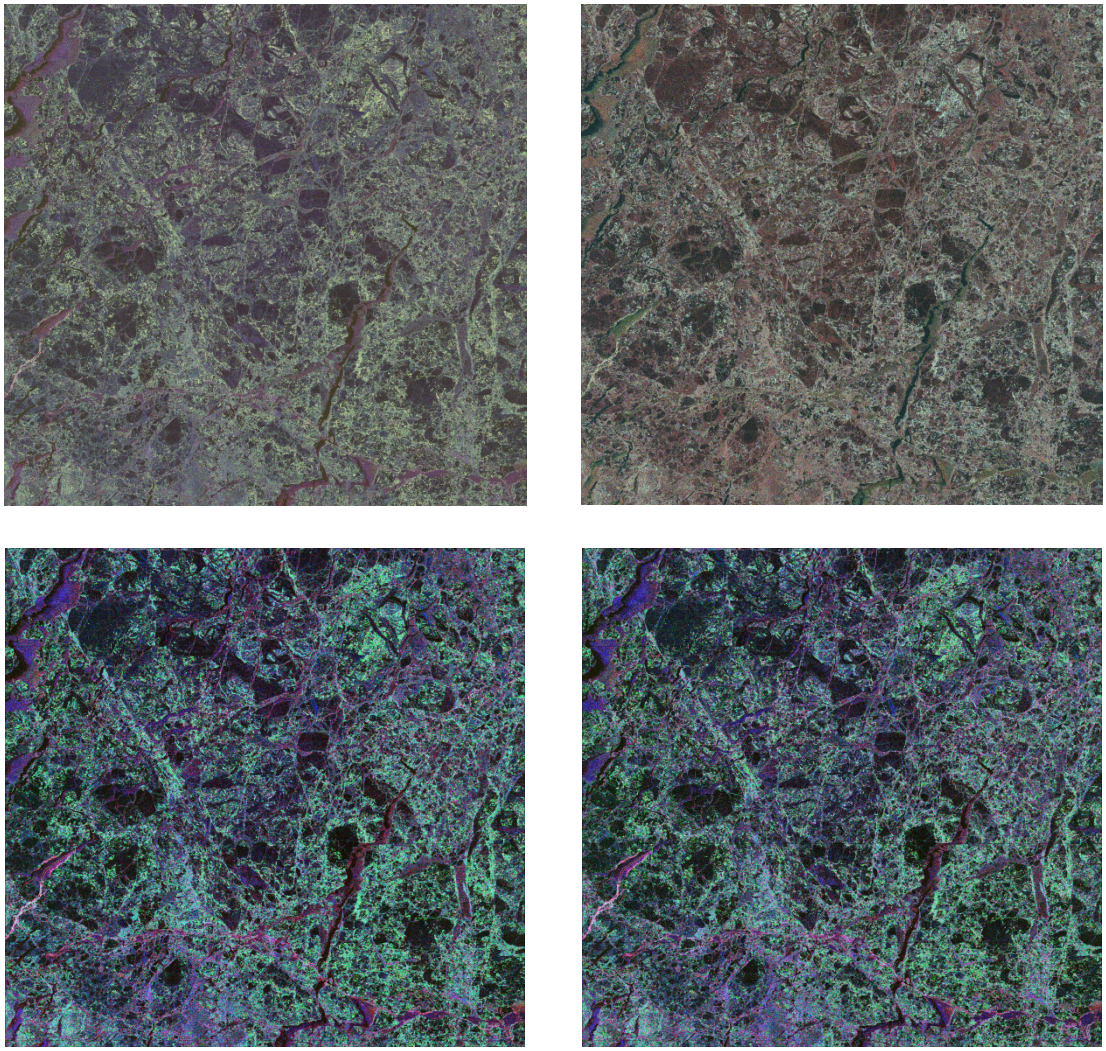

Figure 3.42 RADARSAT Fine quad-pol images on April 13th at 14:46:10 shown in Pauli (upper left), Krogager (upper right), Yamaguchi (upper left)and Yamaguchi rotated (upper right).

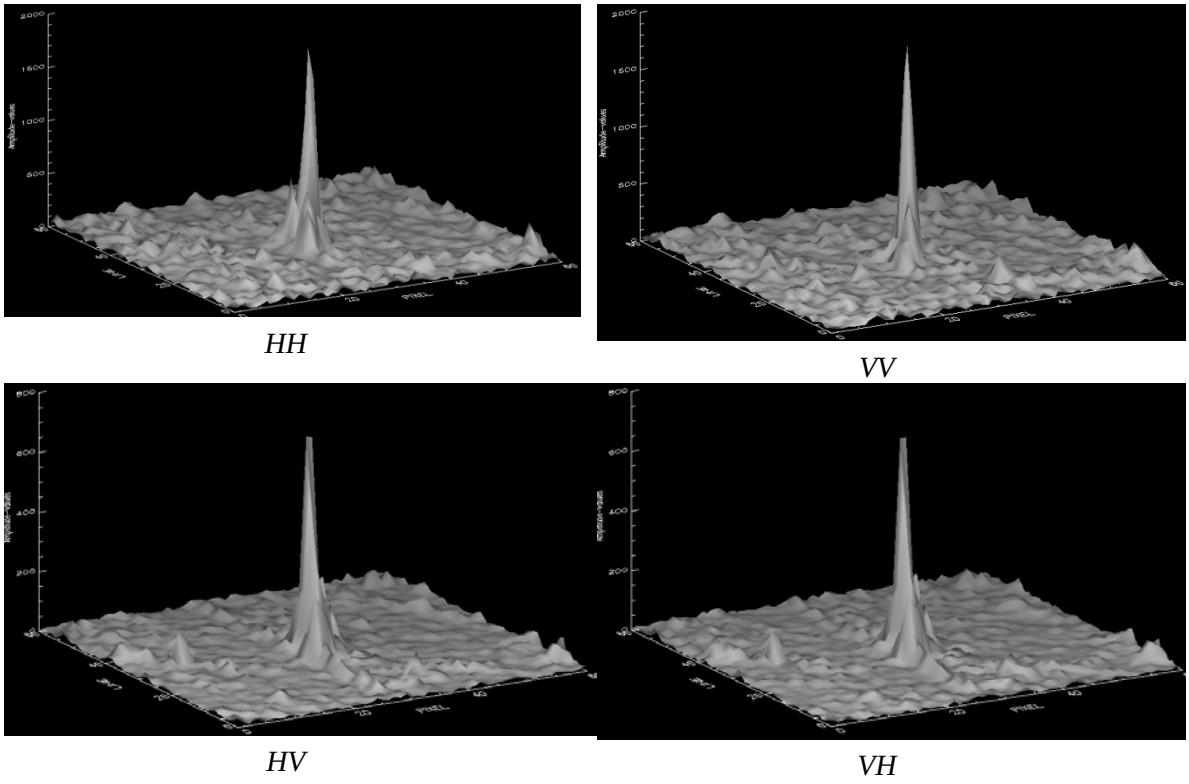

Figure 3.43 3D presentation of KV Svalbard and the background in the RADARSAT-2 SAR image on April 13th 2011th 2010. HH-, VV-, HV- and VH-polarisation are shown.

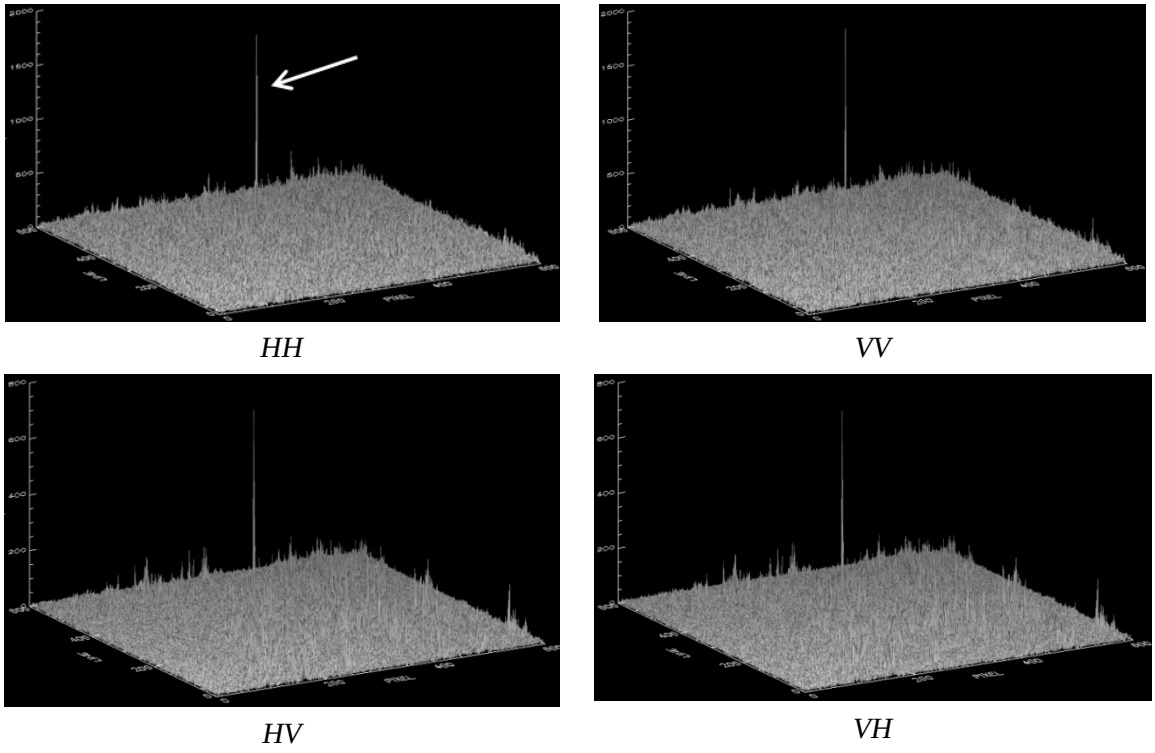

Figure 3.44 3D presentation of 600 pixels × 600 pixels of a RADARSAT-2 SAR image on April 13th 2011th 2010. HH-, VV-, HV- and VH-polarisation are shown. KV Svalbard is shown with the white arrow.

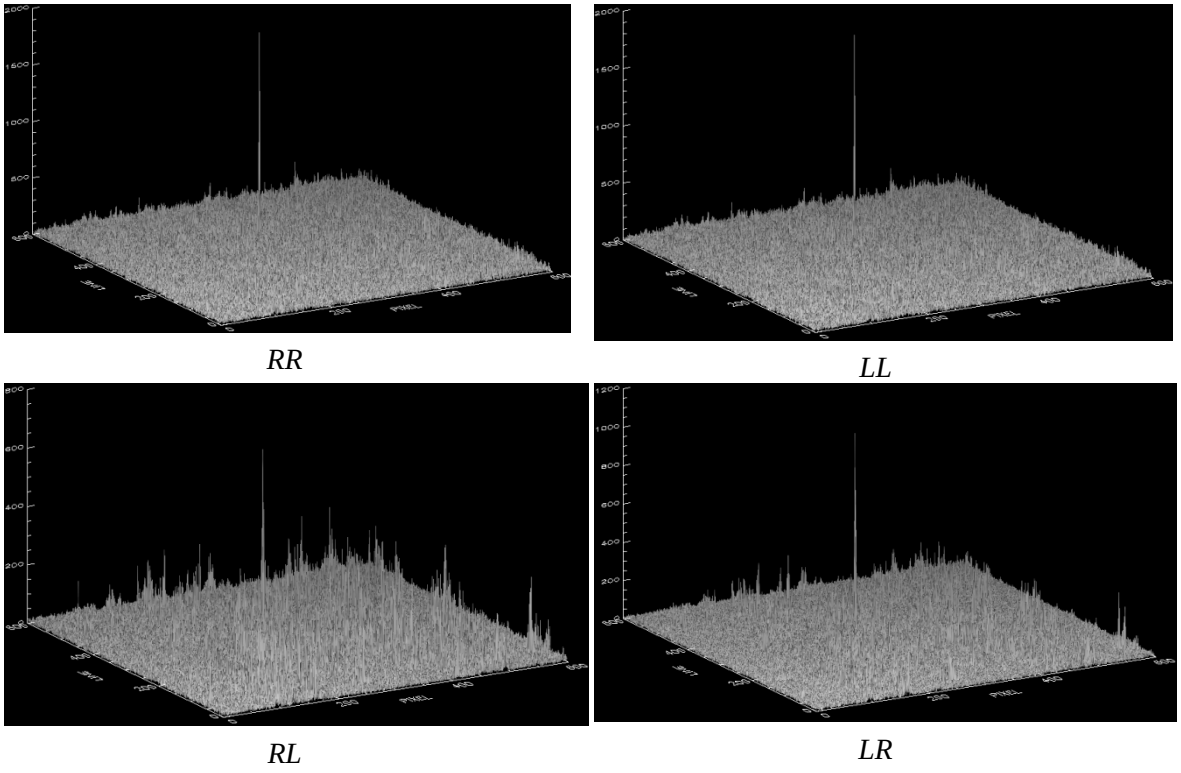

RR *LL*

RL *LR*

Figure 3.45 3D presentation of 600 pixels × 600 pixels of a RADARSAT-2 SAR image on April 13th 2011th 2010. Circular RR, LL, RL and LR are shown.

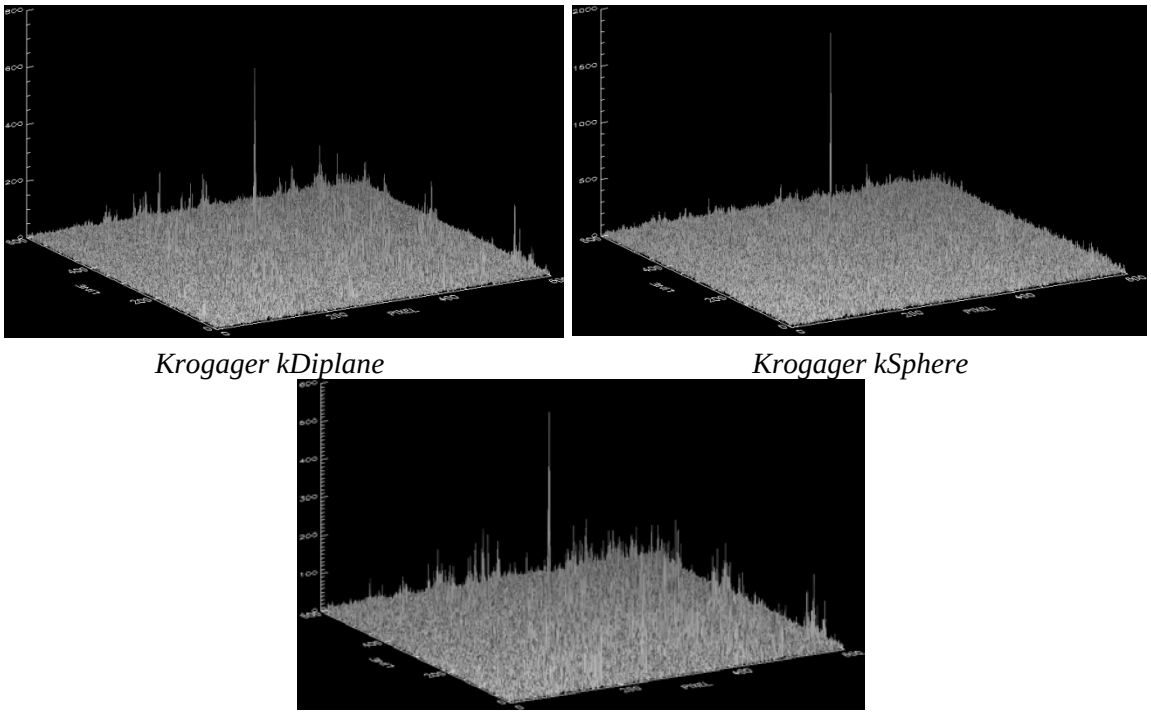

Krogager kDiplane *Krogager kSphere*

Krogager kHelix

Figure 3.46 3D presentation of 600 pixels × 600 pixels of a RADARSAT-2 SAR image on April 13th 2011th 2010. Krogager kDiplane, Krogager kSphere and Krogager kHelix are shown.

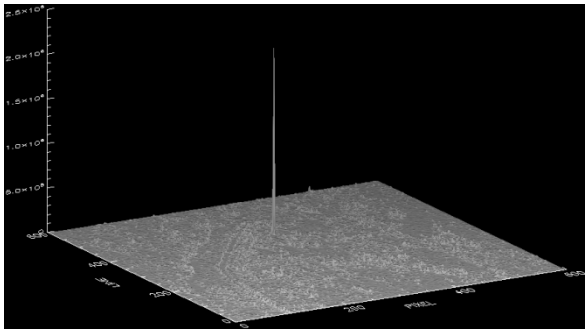

Yamaguchi surface

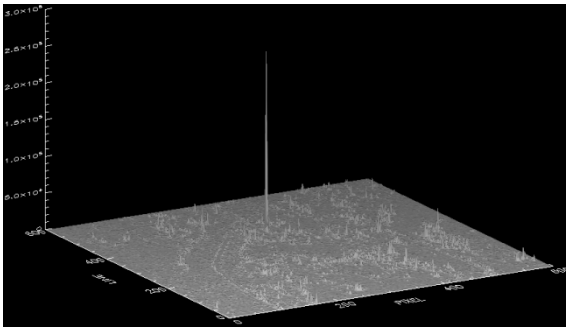

Yamaguch helix

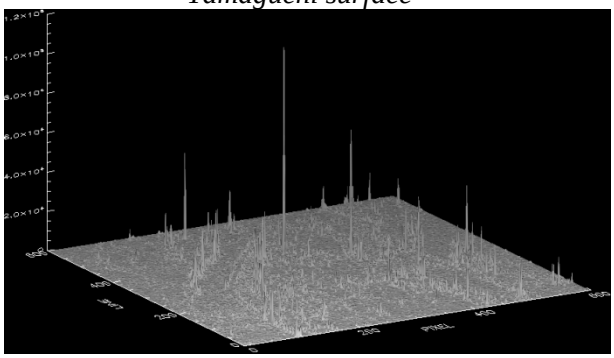

Yamaguchi double

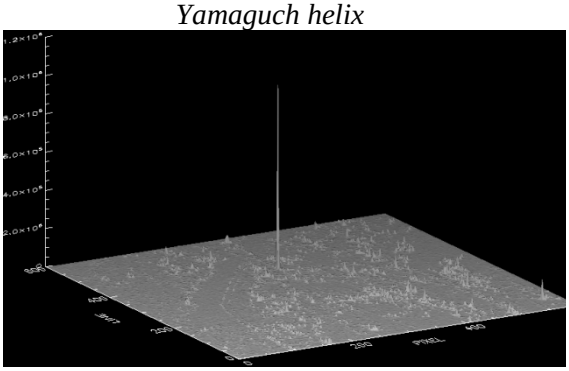

Yamaguchi volume

Figure 3.47 3D presentation of 600 pixels × 600 pixels of a RADARSAT-2 SAR image on April 13th 2011th 2010. Yamaguchi surface, Yamaguchi helix, Yamaguchi double and Yamaguchi volume are shown.

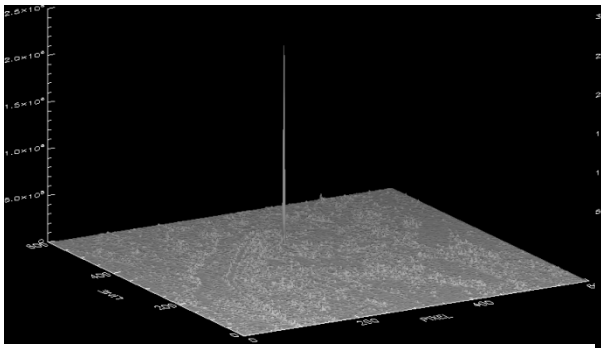

Yamaguchi surface rotated

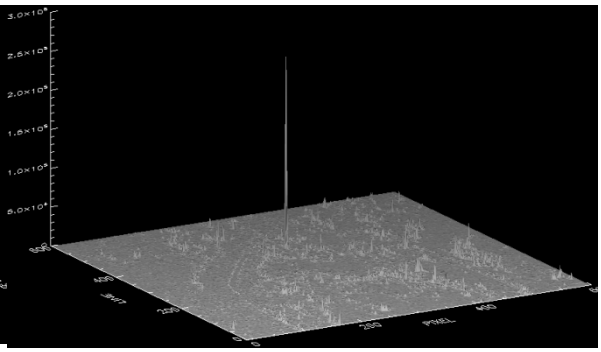

Yamaguchi helix rotated

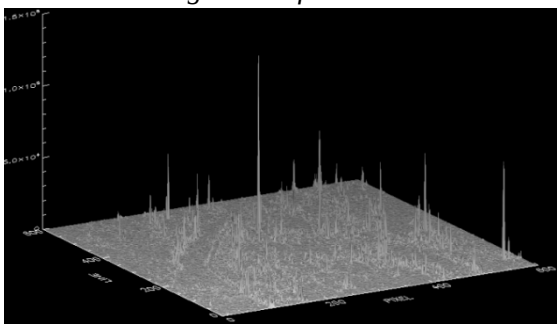

Yamaguchi double rotated

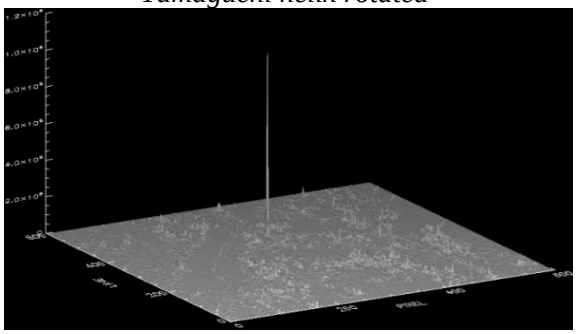

Yamaguchi volume rotated

Figure 3.48 3D presentation of 600 pixels × 600 pixels of a RADARSAT-2 SAR image on April 13th 2011th 2010. Yamaguchi surface rotated, Yamaguchi helix rotated, Yamaguchi double rotated and Yamaguchi volume rotated are shown.

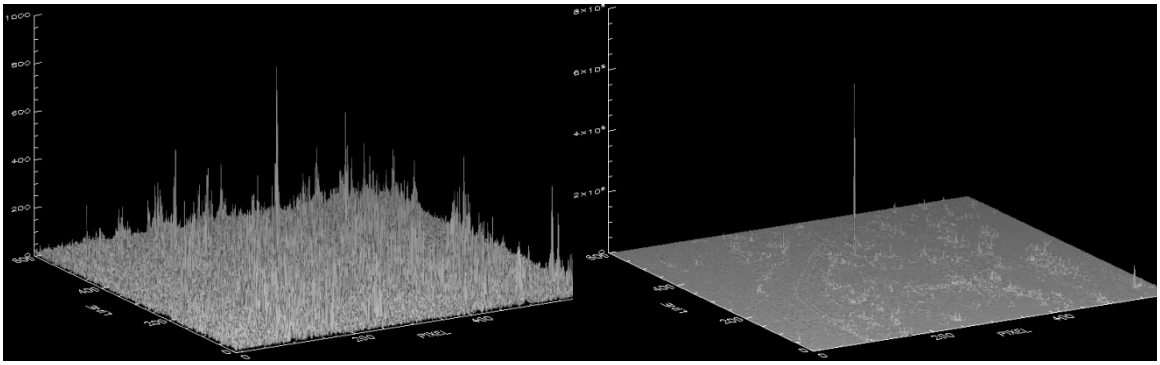

HH-VV *(HH-VV)×HV*

Figure 3.49 3D presentation of 600 pixels × 600 pixels of a RADARSAT-2 SAR image on April 13th 2011th 2010. HH-VV and (HH-VV)×HV are shown.

Table 3.18 shows maximum amplitude divided by mean background and Table 3.19 shows maximum intensity divided by mean intensity background for ice and KV Svalbard at 32.7°.

	Max. amplitude / mean background	
Method	**Ice**	**KV svalbard**
HH	11	71
VV	11	70
HV	18	99
HH-VV	21	48
RR	10	73
RL	21	52
LR	19	94
ksphere	10	74
kDiplane	24	79
kHelix	29	83
Sqrt((HH-VV)×HV)	17	74
Sqrt(Yamaguchi helix)	15	60
Sqrt(Yamaguchi volume)	12	58
Sqrt(Yamaguchi surface)	5	38
Sqrt(Yamaguchi double)	20	62
Sqrt(Yamaguchi helix rot.)	16	69
Sqrt(Yamaguchi volume rot.)	15	64
Sqrt(Yamaguchi surface rot.)	6	39
Sqrt(Yamaguchi double rot.)	18	51

Table 3.18. Maximum amplitude divided by mean background for KV Svalbard and ice.

Maximum amplitude divided by mean background (ice) for KV Svalbard is better for *HV* (99) than for co-polarisation (*HH* =71 and *VV*=70), better for *LR* (94) and *RR* (73) than *LR* (52), better for kHelix (83) than for kDiplane (79) and kSphere (74), better for sqrt(Yamaguchi helix rotated) (69) and sqrt(Yamaguchi volume rotated) (64) than for sqrt(Yamaguchi surface rotated) (39) and sqrt(Yamaguchi surface) (38). Maximum intensity divided by mean background intensity is better

for *VH^2* (5873) and *(HH-VV)×HV* (4727) than *HH^2* (3887) and *VV^2* (3581). Yamaguchi helix rotated (3379) and Yamaguchi volume rotated (3486) has the highest value of the Yamaguchi decompositions, while Yamaguchi surface (1347) has the lowest value. Maximum amplitude for ice with strong reflection divided by mean ice background is better for *HV* (18), *HH-VV* (21), *RL* (21), *LR* (19), kDiplane (24), kHelix (29) and Yamaguchi double rotated (20) than for *HH* and *VV* (11), Yamaguchi surface (5) and Yamaguchi surface rotated (6). Again, Yamaguchi surface (5), Yamaguchi surface rotated (6), Yamaguchi volume (12) and Yamaguchi volume rotated (15) have for ice the lowest four values of the Yamaguchi decompositions. Maximum intensity divided by mean ice background intensity is better for *VH^2* (202), *(HH-VV)×HV* (248), Yamaguchi helix rotated (203), Yamaguchi double (218) and Yamaguchi double rotated (213) than for *HH^2* (85), *VV^2* (83), Yamaguchi surface rotated (35) and Yamaguchi surface (24).

	Max. intensity / mean background intensity	
Method	**Ice**	**KV Svalbard**
HH^2	85	3887
VV^2	83	3581
VH^2	202	5873
(HH-VV)×HV	248	4727
Yamaguchi helix	188	2773
Yamaguchi volume	127	3090
Yamaguchi surface	24	1347
Yamaguchi double	218	2270
Yamaguchi helix rot.	203	3379
Yamaguchi volume rot.	185	3486
Yamaguchi surface rot.	35	1370
Yamaguchi double rot.	213	1754

Table 3.19 Maximum intensity divided by mean background intensity for KV Svalbard and ice.

Figure 3.49 shows that the background is very much suppressed in the *(HH-VV)×HV*-image compared with *HH*-polarisation in Figure 3.43. Table 3.18 shows that maximum amplitude divided by mean background has the value 71 for *HH* and 74 for sqrt*((HH-VV)×HV),* which are similar values. A ship-to-background measure where standard deviation or the variance of the background is included will better emphasize the polarimetric combinations and decompositions. Therefore a ship-to-background measure is calculated where the maximum amplitude divided by the mean background and the standard deviation of the background. Then the difference between the target and mean background are compared with the variations in the background. Then the ratio will have a high value if the background is suppressed and if the standard deviation (variation) in the background is reduced. The results are shown in Table 3.20, which shows the maximum amplitude divided by the mean background and the standard deviation of the background, and Table 3.21, which shows the maximum intensity divided by the mean background intensity and the standard deviation of the background intensity.

	Max. amplitude / (mean sea × standard dev. of background)	
Method	**Ice**	**KV svalbard**
HH	0.4	2.2
VV	0.4	1.9
HV	3.1	12.8
HH-VV	1.3	3.0
RR	0.3	2.2
RL	2.2	4.2
LR	2.0	8.9
kSphere	0.4	2.2
kDiplane	3.4	11.1
kHelix	4.0	7.6
Sqrt(HH-VV)×HV)	2.5	8.5
Sqrt(Yamaguchi helix)	2.5	7.3
Sqrt(Yamaguchi volume)	1.4	4.5
Sqrt(Yamaguchi surface)	0.3	1.5
Sqrt(Yamaguchi double)	2.0	8.0
Sqrt(Yamaguchi helix rot.)	2.7	7.4
Sqrt(Yamaguchi volume rot.)	1.3	4.1
Sqrt(Yamaguchi surface rot.)	0.3	1.5
Sqrt(Yamaguchi double rot.)	1.9	5.5

Table 3.20 Maximum amplitude divided by mean background and standard deviation of the background for KV Svalbard and ice.

	Max. int. / (mean sea int. × standard dev. of background int.)	
Method	**Ice**	**KV Svalbard**
HH^2	0.05	1.6
VV^2	0.1	1.1
VH^2	1.8	36.2
(HH-VV)×HV	2.0	24.8
Yamaguchi helix	2.1	20.9
Yamaguchi volume	0.5	6.2
Yamaguchi surface	0.0	0.6
Yamaguchi double	1.5	26.5
Yamaguchi helix rot.	2.5	21.2
Yamaguchi volume rot.	0.6	5.7
Yamaguchi surface rot.	0.0	0.6
Yamaguchi double rot.	1.5	14.6

Table 3.21 Maximum intensity divided by mean background intensity and standard deviation of the background intensity for KV Svalbard and ice.

Table 3.20 shows that the contrast is much stronger for sqrt*((HH-VV)×HV)* (8.5) than for *HH-*

(2.2) and *VV*-polarisation (1.9) for KV Svalbard. The difference is clearer here than in Table 3.18, and the larger difference is more the same what we see in the figures. Maximum amplitude divided by mean background and standard deviation of the background for KV Svalbard is better for *HV* (12.8) than for co-polarisation (*HH*=2.2 and *VV*=1.9), better for *LR* (8.9) than *RR* (2.2), better for kDiplane (11.1) and kHelix (7.6) than for kSphere (2.2), better for sqrt(Yamaguchi helix) (7.3), sqrt(Yamaguchi helix rot.) (7.4) and sqrt(Yamaguchi double) (8.0) than for sqrt(Yamaguchi surface) (1.5) and sqrt(Yamaguchi surface rotated) (1.5). Maximum intensity divided by mean background and standard deviation intensity is better for *VH^2* (36.2) and *(HH-VV)×HV* (24.8) than *HH^2* (1.6) and *VV^2* (1.1). Yamaguchi double (26.5), Yamaguchi helix rotated (21.2) and Yamaguchi helix (20.9) have the highest values of the Yamaguchi decompositions, while Yamaguchi surface (0.6) and Yamaguchi surface rotated (0.6) have the lowest values. The contrast values calculated this way show more what are seen in Figure 3.44 - Figure 3.49.

Maximum amplitude for ice with strong reflection divided by mean ice background and standard deviation of the mean background is better for *HV* (3.1), *RL* (2.2), *LR* (2.0), kDiplane (3.4), kHelix (4.0), sqrt*((HH-VV)×HV)* (2.5), Yamaguchi helix (2.5) and Yamaguchi helix rotated (2.7) than for *HH* (0.4) and *VV* (0.4), RR (0.3), Yamaguchi surface (0.3), Yamaguchi surface rotated (0.3) and kSphere (0.4). Maximum intensity divided by mean ice background intensity and standard deviation intensity is better for *VH^2* (36.2), *(HH-VV)×HV* (24.8), Yamaguchi helix rotated (21.2), Yamaguchi helix (20.9) and Yamaguchi double rotated (26.5) than for *HH^2* (1.6), *VV^2* (1.1), Yamaguchi surface rotated (0.6) and Yamaguchi surface (0.6).

Ice has the lowest values for these four variables: sqrt(Yamaguchi volume), sqrt(Yamaguchi surface), sqrt(Yamaguchi volume rotated) and sqrt(Yamaguchi volume rotated). This is not the case for the vessels.

Table 3.22 shows ratios calculated using Yamaguchi decomposition results. For KV Svalbard and ice with a background of ice at lower incidence angle the situation is different than what was the case with an incidence angle above 40° as was the case in Table 3.16 and Table 3.17.

Method	Ice	KV Svalbard
Yd/Ys	9.1	1.7
Yd/Yv	1.7	0.7
Yd/Yh	1.2	0.8
Ydr/Ysr	6.1	1.3
Ydr/Yvr	1.1	0.5
Ydr/Yhr	1.0	0.5

Table 3.22 Ratios based on maximum amplitude divided by mean background calculated using Yamaguchi decomposition results for ice and KV Svalbard.

Figure 3.50 - Figure 3.53 show segments of SAR images in *HH*-polarisation, *VV*-polarisation,

HV-polarisation, Pauli decomposition, Krogager decomposition, Yamaguchi decomposition and Yamaguchi rotated decomposition.

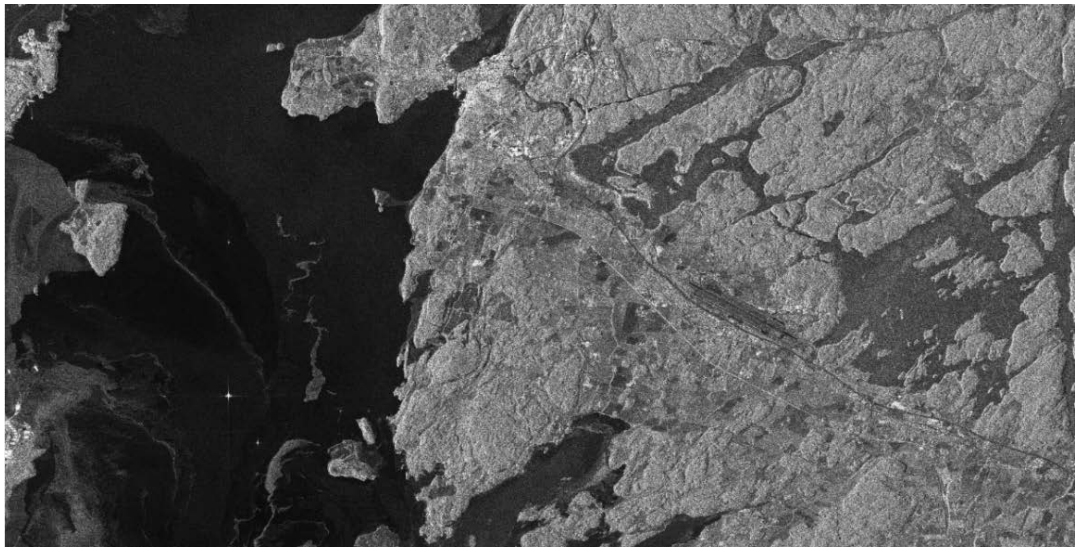

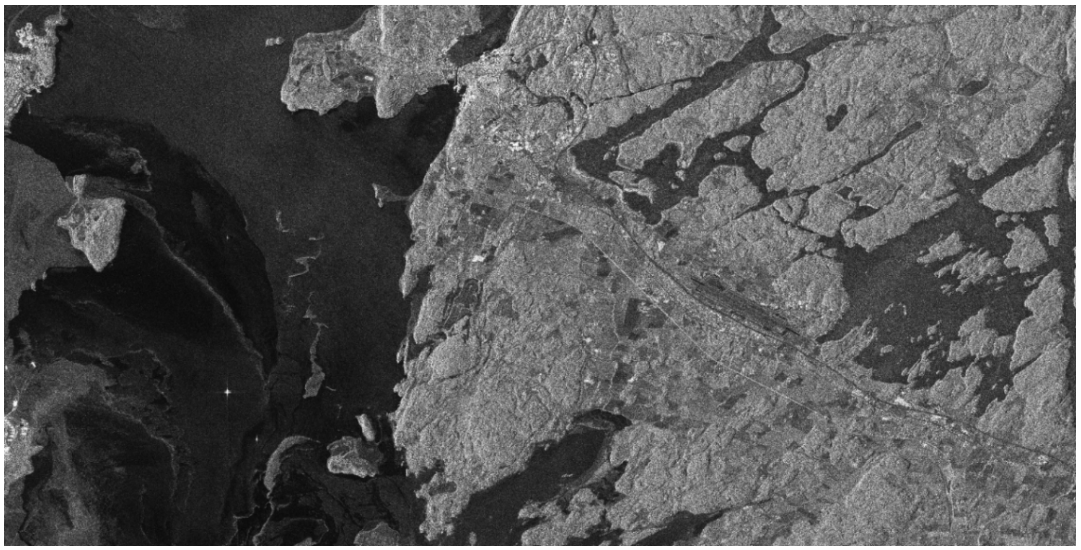

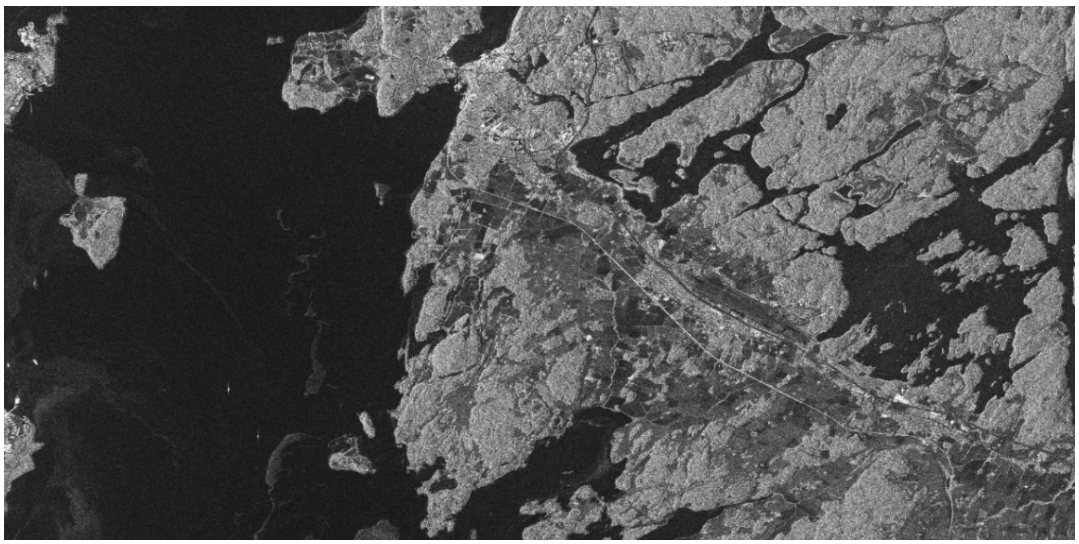

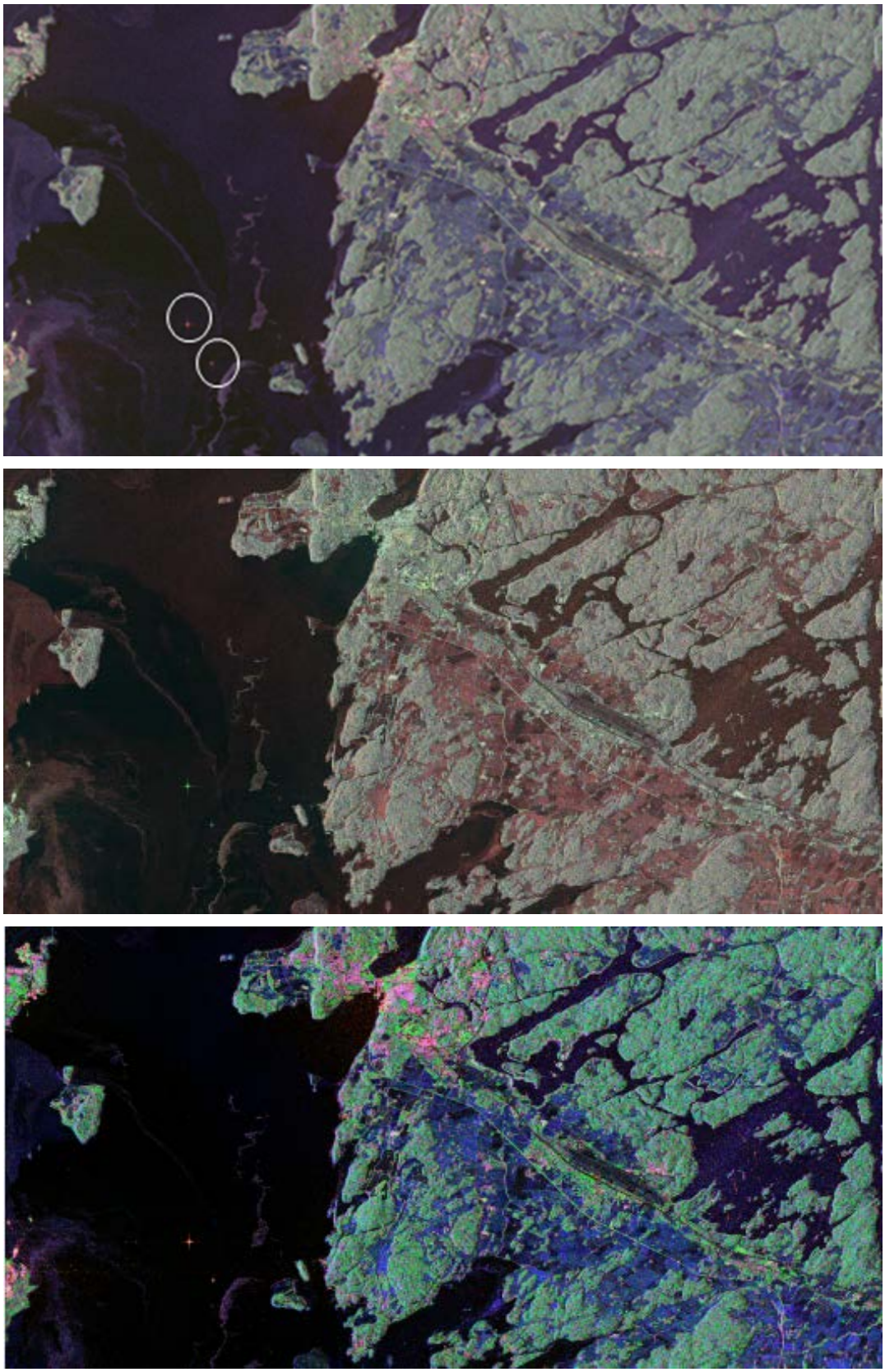

Figure 3.50 Segments of a SAR image on February 7th 2010 in the Oslofjord shown in HH-polarisation (top previous page), VV-polarisation (middle previous page), HV-polarisation (bottom previous page), Pauli (top), Krogager (middle) and Yamaguchi rotated (bottom).

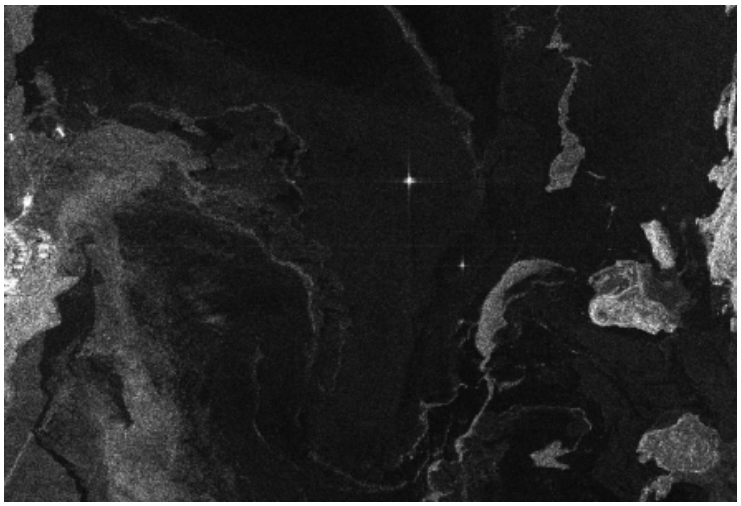

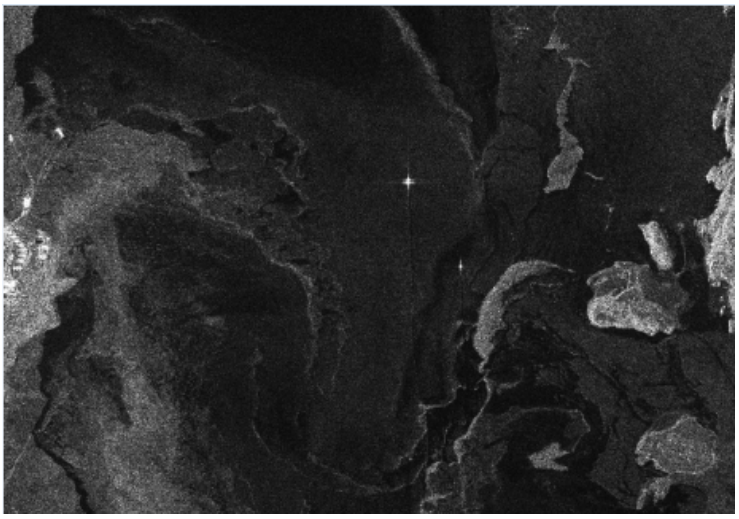

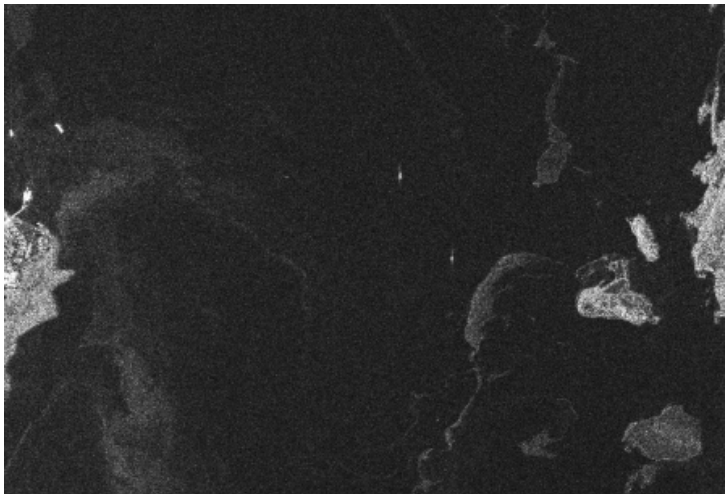

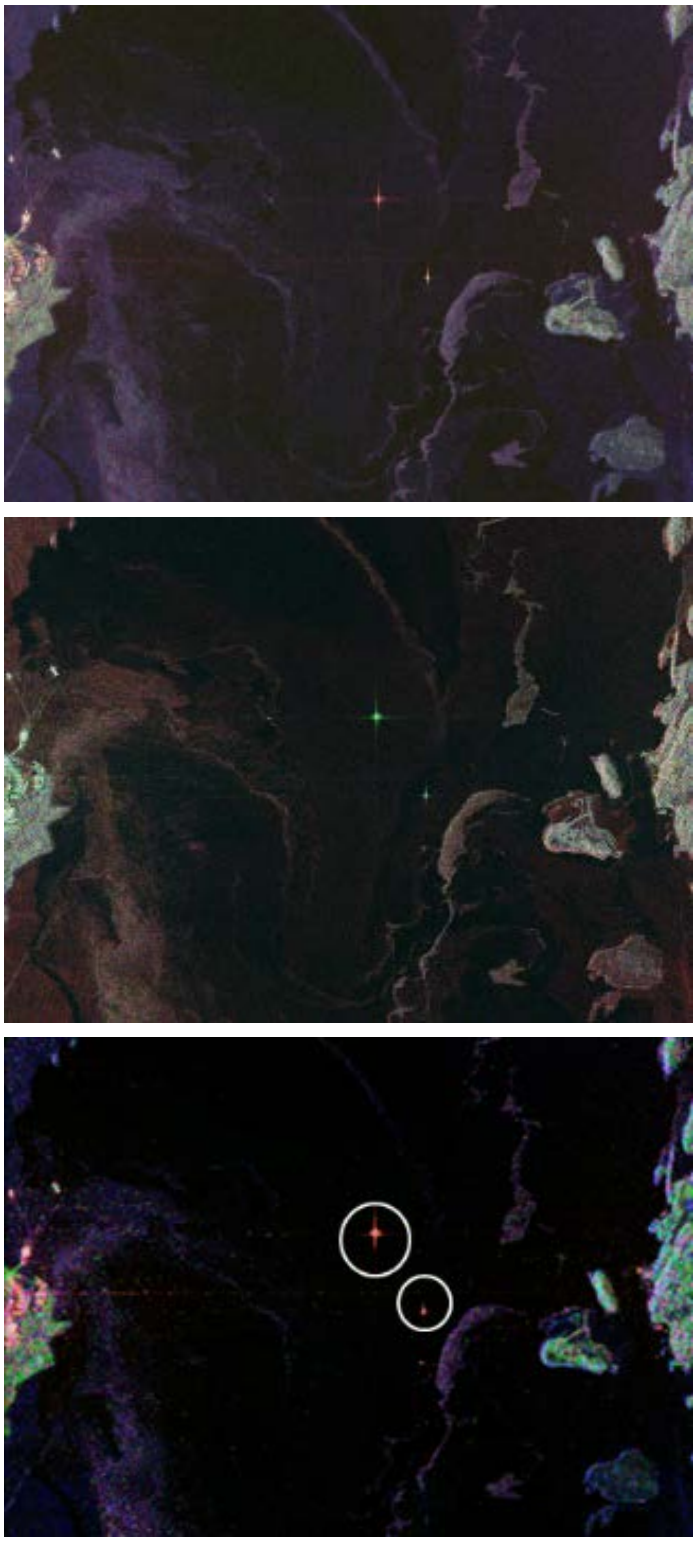

Figure 3.51 Sub images of SAR image on February 7th 2010 in the Oslofjord showing both ice and vessels (inside the circles). Hagland Bona and Sunbeam are shown. Top previous page: HH-polarisation, middle previous page: VV-polarisation, bottom previous page: HV-polarisation, top: Pauli, middle: Krogager and bottom: Yamaguchi.

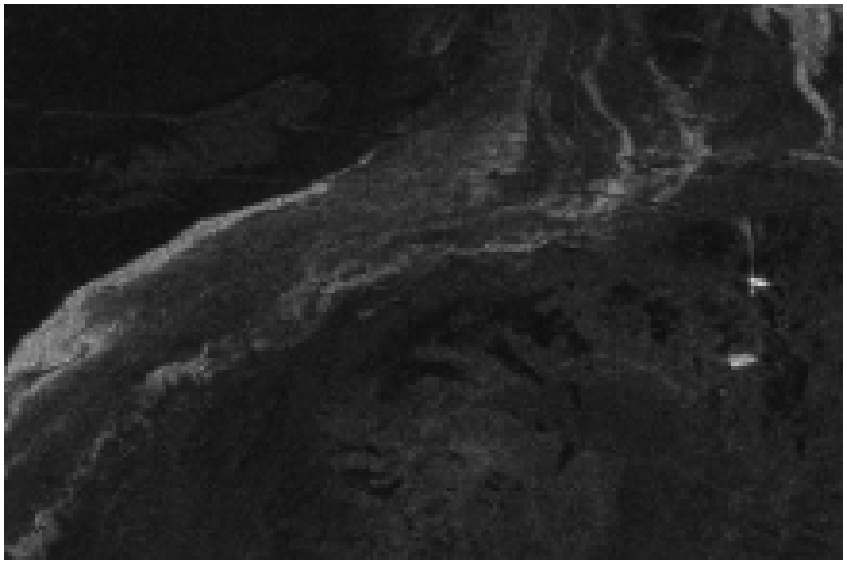

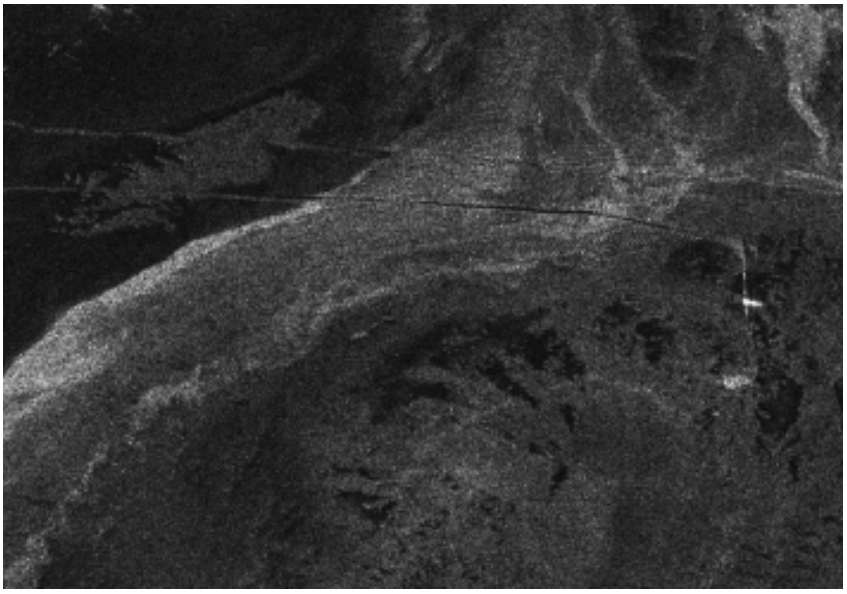

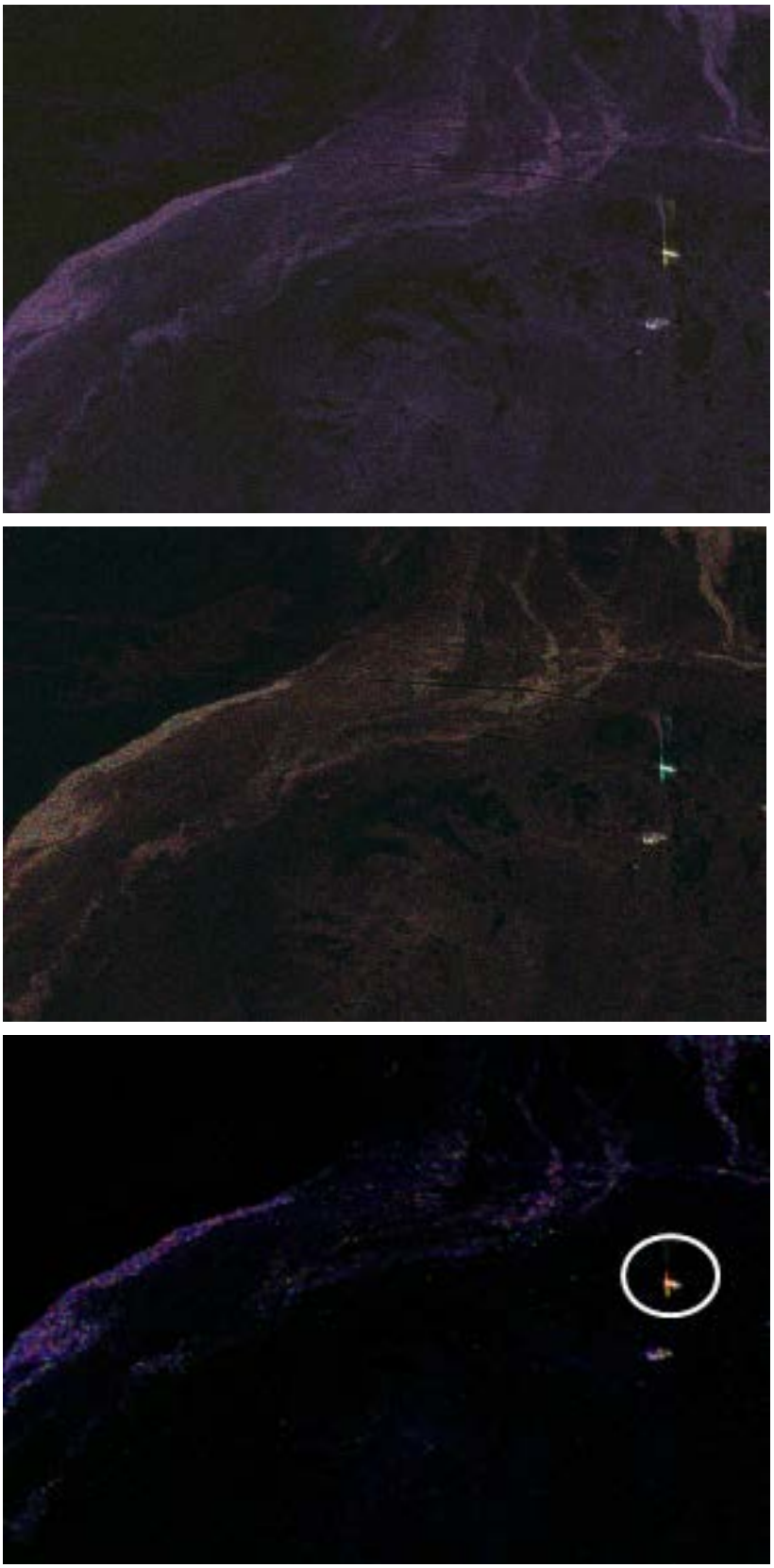

Figure 3.52 Sub images from February 7th 2010 in the Oslofjord showing both ice and a vessel, Color Viking (inside the circles). Top previous page: HH-polarisation, middle previous page: VV-polarisation, bottom previous page: HV-polarisation, top: Pauli, middle: Krogager bottom:Yamaguchi.

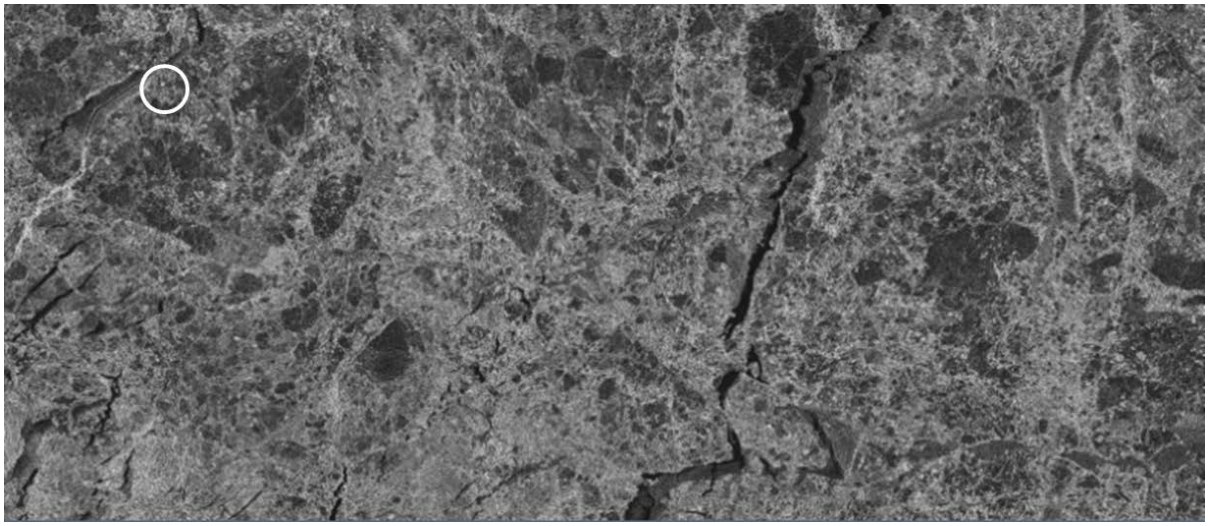

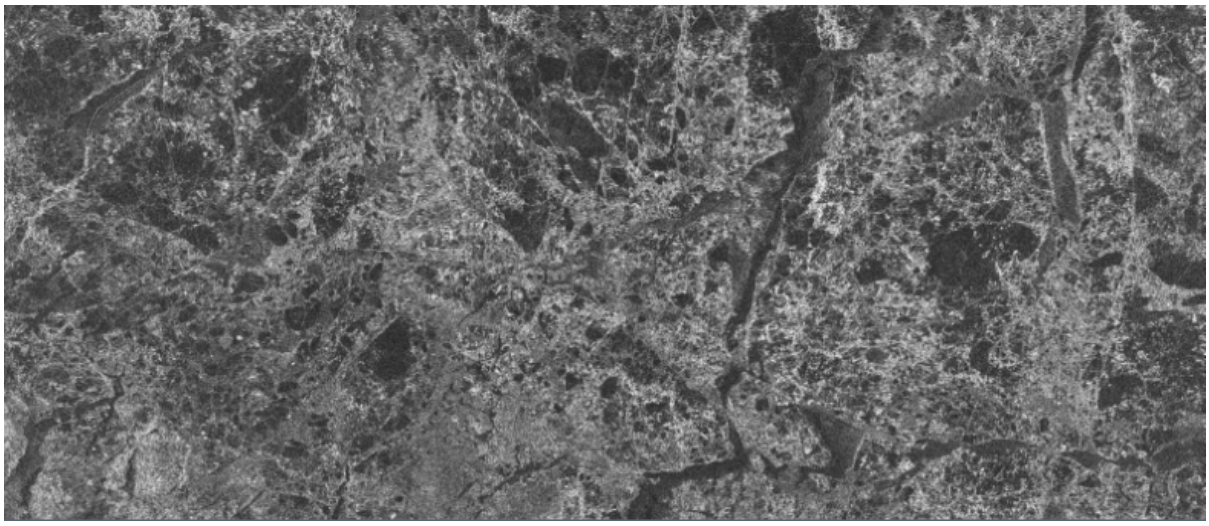

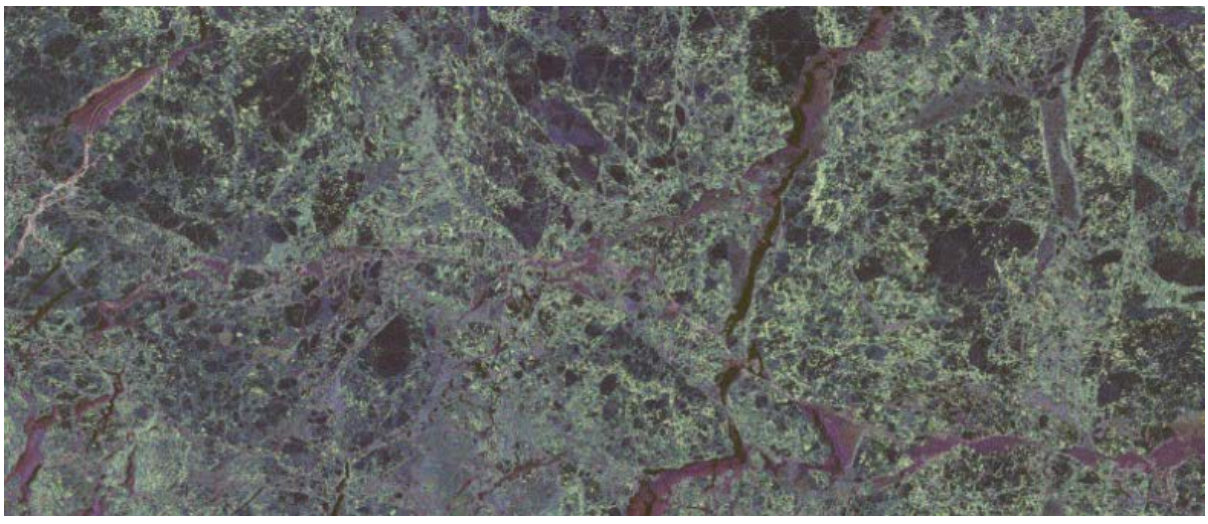

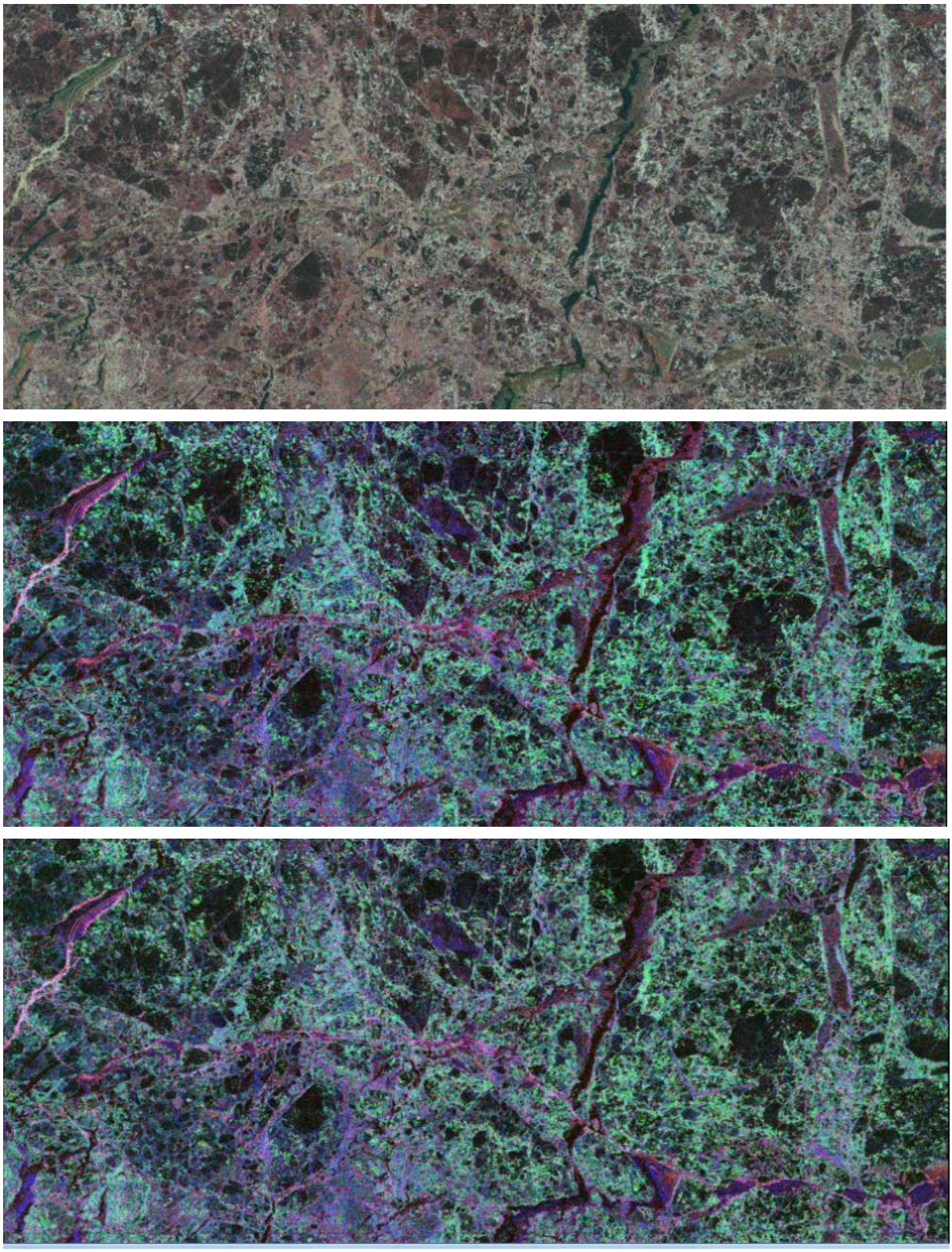

Figure 3.53 Sub images from RADARSAT-2 Fine quad-pol on April 13th 2011 north of Spitsbergen. HH-polarisation (top), HV-polarisation, Pauli (middle top), Krogager (middle bottom), Yamaguchi and Yamaguchi rotated (bottom) are shown. The vessel KV Svalbard is shown inside the circle in the HH-polarisation segment.

Figure 3.51 shows a close up of a part of Figure 3.50. The ice in the fjord is easy to spot in Pauli and Krogager. The vessels, Hagland Bona and Sunbeam, are shown inside the two circles in the Pauli image. In the Pauli image the ice has a purple colour, while the vessels are more pink and brighter. In the Krogager image the vessels are sharp green and bright, while the ice is darker green, almost brown. In the Yamaguchi image the vessels are bright and red/pink in colour, while the ice is dark pink/purple in colour. In the Pauli decomposition, and partly in the Yamaguchi decomposition, images it is easier to distinguish between land and ice. More ice is visible in those decompositions, as well as in *HH*- and *VV*-polarisation. The vessels are clearly visible and have another colour than the ice in all three decomposition methods. Figure 3.52 shows a segment of an area with ice and a vessel, Color Viking, south in the Oslofjord. The vessel is visible in all segments. In the Krogager decomposition, the vessel is clear green, and different from the surroundings. In the Yamaguchi decomposition, the vessel is also very clear, in a pink colour, which is slightly different from the surroundings. Figure 3.53 shows segments of a RADARSAT-2 Fine quad-pol recording north of Spitsbergen. Using the Pauli, Krogager and Yamaguchi decomposition methods shows that the different types of ice are shown in different colours and strengths of colour. The vessel KV Svalbard is shown inside the circle in the *HH*-polarisation segment.

The situations for max amplitude and max intensity divided by mean background are different for vessels and ice against sea background than for vessels and ice against ice background.

4 Conclusions and further work

Norway has large ocean areas in the North that require effective methods for surveillance of vessel traffic, fishing and smuggling. Radar satellites are being used daily of the Norwegian Defence for ship detection.

Radar satellites offer dual- and/or quad-polarised data, and the information content in these data are superior compared to the earliest single-polarised satellites. Extensive research has been done the latest years on how to best use and combine the different polarisation channels.

FFI has developed an automatic ship detection tool, Aegir, which detects vessels in all polarisation channels as well as in a “channel” where the available polarisation channels are combined to enhance the ship to sea contrast. When dual-polarisation data are available the co- and cross-polarisation channels are multiplied, and the ship detector Aegir can be run on this combined “channel”. When quad-polarisation data are available, Aegir is also run on a combined polarisation channel, where the double bounce and the volume scattering are multiplied, *(HH-VV)×HV*. Both methods give evident enhancements on the ship to sea contrast.

It is also possible to do extra polarimetric analysis when quad-polarimetric data are available, using the Pauli, Circular, Krogager and Yamaguchi decomposition methods. Combining the available polarisation channels increases the ship to sea contrast. It is shown that

cross-polarisation and *(HH-VV)×HV* work very well for ship detection for all incidence angles. *HH*-polarisation works well for high incidence angles, but not for low and medium incidence angles.

The polarisation decomposition methods can be used to increase the ship to sea contrast and help to discriminate between ice and vessels. It is shown that all Yamaguchi decompositions, but especially Yamaguchi double rotated, give high ship to sea contrasts, and it is easier to spot the vessels against a sea or ice background. Using information from all polarisation channels and polarisation combinations can give information to find out if a detected target is a vessel or ice. It may be possible to discriminate ice and vessels by looking at the statistics on max value divided by background and using known information from the polarisation channels and the polarisation combinations. Yamaguchi surface values (both with rotation and without rotation) are higher than Yamaguchi volume values or approximately the same for ice. The values for sqrt(Yamaguchi double rotated) are much lower than sqrt(Yamaguchi volume) for ice than the corresponding values are for vessels. Ice has the lowest values for these four variables: sqrt(Yamaguchi volume), sqrt(Yamaguchi surface), sqrt(Yamaguchi volume rotated) and sqrt(Yamaguchi volume rotated). This is not the case for the vessels. Maybe some of this information can be used to see the difference between ice and vessels.

It may also be possible to distinguish vessels and ice by visibly looking at Pauli, Krogager and Yamaguchi decomposition methods represented in red, green and blue.

Previously, high resolution and/or quad-polarisation (quad-pol) images only covered small areas, and were mainly useful in harbour areas or over a known small area of interest. To be able to image vessels of interest in the open ocean with high resolution and/or quad-polarisation before, information in advance was necessary to locate where the images should be acquired. From 2011 RADARSAT-2 provided new wide modes, thus opening up new opportunities to use high resolution and quad-polarisation images for operational ship detection due to increased coverage area.

The situation is different when looking at the target to background contrast when the background is sea and when the background is ice. This has to be taken into account when analysis is done. More research can be done to analyse the consistency of the results and see how the results can be used when analysing radar images on a daily basis. The contrasts depend on if the background is sea, ice or partly ice and sea, the incidence angle and the size of the vessel.

References

[1] Arnesen, T.N. and R.B. Olsen. Vurdering av ENVISAT ASAR for Skipsdeteksjon. FFI-Rapport, 2004/02121, 2004.

[2] Arnesen, T.N., R.B. Olsen and D.J. Weydahl. Ship Detection Signatures in AP Mode Data. International Astronautical Congress, Fukuoka, Japan, 2005.

[3] Brekke, C. Automatic Ship Detection Based on Satellite SAR. FFI-Rapport, 2008/00847, 2008.

[4] Laval, M.Full and Compact Polarimetric Radar Interferometry for Vegetation Remote Sensing. PhD Thesis, Institut d'Electronique et de Télécommunications de Rennes, Université Rennes 1, 18th December, 2009.

[5] Krogager, Ernst. Polarimetry – For the Full Story. RTO SCI Symposium on "Non-Cooperative Air Target Identification Using Radar". Mannheim, Germany, 22-24 April 1998. Published in RTO-MP-6.

[6] Lee, Jong-Sen, Eric Pottier. Polarimetric Radar Imaging. From Basics to Applications. CRC Press. Taylor & Francis Group, FL, USA. ISBN 978-1-4200-5497-2.

[7] Yamaguchi, Y., A. Sato, W.-M. Boerner, R. Sato, H. Yamada. Four-Component Scattering Power Decomposition With Rotation of Coherency Matrix. IEEE Transactions on Geoscience and Remote Sensing, Vol. 49, No. 6, pp. 2251-1158, 2011.

[8] Yamaguchi, Y., A. Sato, W.-M. Boerner, R. Sato, H. Yamada. Four-Component Scattering Model for Polarimetric SAR Image Decomposition. IEEE Transactions on Geoscience and Remote Sensing, Vol. 39, No. 8, pp. 1699-1706, 2005.

[9] Huynen, J.R. Phenomenological theory of radar targets. Ph.D. dissertation, univ. Technol., Delft, The Netherlands, 1970.

[10] Xu, F and Y.Q. Jin. Deorientation theory of polarimetric scattering taregts and application to terrain surface classification. IEEE Trans. Geosc. Remote Sens., Vol. 43, No. 10, pp. 2351-2364, Oct 2005.

[11] Yajima, Y., Y. Yamaguchi, R. Sato, H. Yamada, W.-M. Boerner. POLSAR image analysis of wetlands using a modified four-component scattering power decomposition. IEEE Trans. Geosc. Remote Sens., Vol. 46, No. 6, pp. 1667-1673, Jun. 2008.

[12] Weydahl, D.J. Personal Communication 2010.

[13] R. B. Olsen, K. Eldhuset, Ø. Helleren, and C. Brekke, "Analysis of Options for MARISS Service Extension,"MARISS-FFI-TN2-TN-015. Issue 2., Nov.2009.

[14] Statoil and VisSIM AS, 2010.

[15] Aisonline. *Christian Michelsen Research. www.aisonline.com. 2010.*

[16] Krogager, Ernst. Advances of Techniques for Utilizing Polarimetric Features of Radar Targets. RTO SET Symposium on "Target Identification and Recognition Using RF Systems", Oslo, Norway, 11-13 October 2004. Published in RTO-MPO-SET-080.

Acronyms

AIS	Automatic Identification System
CFAR	Constant False Alarm Rate
Co-pol	Co-polarisation
Cross-pol	Cross-polarisation
Dual-pol	Dual-polarisation
FFI	Forsvarets Forskningsinstitutt
H	Horisontal polarisation
HH	Horisontally transmitted – Horisontally received polarisation
HV	Horisontally transmitted – Vertically received polarisation
k_d	Krogager diplane
k_h	Krogager helix
k_s	Krogager sphere
KS_{LL}	Krogager Left Left
KS_{LR}	Krogager Left Right
KS_{RL}	Krogager Right Left
KS_{RR}	Krogager Right Right
LL	Left, Left (circular polarisation)
LR	Left, Right (circular polarisation)
PDF	Probability Density Function
Quad-pol	Quad-polarisation
RGB	Red, Green, Blue
RL	Right, Left (circular polarisation)
RR	Right, Right (circular polarisation)
SAR	Synthetic Aperture Radar
sc1	Scaling factor 1
sc2	Scaling factor 2
V	Vertical polarisation
VH	Vertically transmitted – Horisontally received polarisation
VV	Vertically transmitted – Vertically received polarisation

Appendix A SAR and AIS

Spaceborne and land-based AIS (Automatic Identification System) are used operationally every day in Norway. AIS data can be used to verify and identify the vessels in the SAR images. Ship detection in SAR imagery and tracking based on AIS reports are complementary. Land based AIS data can be collected from Statoil and VisSim AS [14] and aisonline.com [15]

Appendix B Automatic ship detection - Aegir

Aegir is an automatic ship detection tool developed at FFI. The software tool automatically detects bright objects in all polarisation channels in SAR images.

Figure B-1 shows the work flow of Aegir. The K-distribution thresholding algorithm is used. First the image is divided into overlapping frames of M pixels × M pixels. The method is based on Probability Density Function (PDF). Threshold value and model parameters are estimated for each frame. The three main parameters are the L (Equivalent Number of Looks), the order parameter, ν, of the K-distribution and the Constant False Alarm Rate (CFAR) [3]. The available polarimetric images can be fused before the ship detection algorithm Aegir is run.

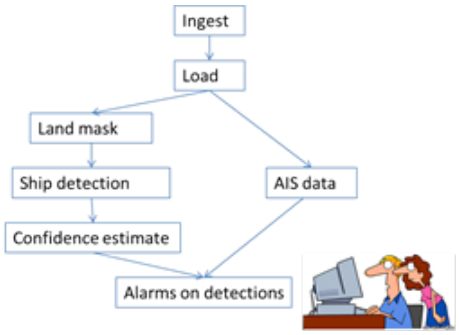

Figure B.1 Work flow of the automatic ship detection tool Aegir.